

---

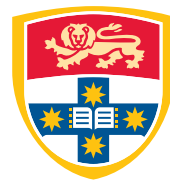
# **Investigation of Propeller Interactions for Mini Aerial Vehicles**

---

**Jasmine Warner**

Supervisor: Associate Prof. Dries

Verstraete



THE UNIVERSITY OF  
**SYDNEY**

School of Aerospace, Mechanical and Mechatronic Engineering  
The University of Sydney

A thesis submitted to The University of Sydney in fulfilment of the requirements for  
the degree of *Bachelor of Engineering Honours*

Nov 2022



Thank you so much to my incredible supervisor, Dries Verstraete, for the guidance, direction, wisdom, banter and encouragement you have given me this year. It would have been impossible to finish this without you.



# Declaration

I, Jasmine Warner, hereby declare that this thesis submission titled *Investigation of Propeller Interactions for Mini Aerial Vehicles* is my own work and that, to the best of my knowledge and belief, it contains no material previously published or written by another person nor material which to a substantial extent has been accepted for the award of any other degree or diploma of the University or other institute of higher learning, except where due acknowledgement has been made in the text. Specifically, the work I contributed consists of:

1. Conducting the literature review
2. Assisting in producing a 3D model of the generic micro aerial vehicle
3. Wind tunnel testing of the generic micro aerial vehicle model
4. Analysing data of wind tunnel results and validating collected data using VAP 3.5
5. Writing this thesis report.

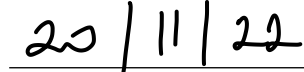
Assistance was received from Benjamin Van Magil in the development of the MAV model.  
Assistance was received from my supervisor in the areas of:

1. Distinguishing relevant literature and indicating critical software required for this thesis
2. Assisting in developing the final MAV model
3. Ameliorating this thesis through constant feedback.



Jasmine Warner

*Author*



Date

---

A/Prof. Dries Verstraete

*Supervisor*

---

Date



## Acknowledgements

This year has been the most difficult year of my life for many reasons, and I want to thank all the people who have helped motivate me to keep going when I truly felt like giving up for the first time in my life.

Firstly I want to acknowledge the incredible patience, support and encouragement my thesis supervisor, Dr Dries Verstraete, has given me this year. From replying to emails at ridiculous night hours to motivating me when I was at my absolute lowest. Thank you so much, and I am so grateful to have had the opportunity to do this thesis under your guidance.

To Benjamin Van Magil, thank you for taking time out of your schedule to help me learn more about FreeCAD and the design decisions you've made yourself when designing 3D printed models. For finalising the model design with me and assisting in the wind tunnel along with some of the other PhD students, thank you so much!

To Gabby Papadopoulos, thank you for letting me visit every day, being there for me, and helping me process all that I've been through this year. Our daily runs and midnight conversations helped me process so many different things. This thesis would have never made it to fruition without you. Thank you.

To Irina Tyan, her partner Ben, and her parents, who have given me so much support during the most incredibly stressful time of my life. You made an impossible situation something that helped me grow as a person, and I will forever appreciate the kindness and support you have all shown.

To Alex, who dragged me out of the house when I barely had the energy to get up in the morning. Thank you for encouraging me to keep going and giving me little nuggets of advice when everything was too overwhelming. Your advice helped me break this into more manageable chunks of work until I finally reached the end.



# Investigation of Propeller Interactions for Mini Aerial Vehicles

## Abstract

Micro Aerial Vehicles (MAVs) are a class of unmanned aerial vehicles that vary from the size of an insect to sizes similar to large birds. They are difficult to design and manufacture, due to several main factors, including low-speed flight, small physical dimensions, structural strength, reduced stall speed and low inertia. With MAV design becoming one of the fastest-growing areas of development in the aerospace industry, there is a need for experimental data to model varieties of MAV configurations. This investigation outlines propellers' influence on MAVs' aerodynamics and stability.

The aerodynamic analysis of the MAV showed that the addition of the propeller delayed the MAVs stall in all configurations. This effect is seen to a greater extent for the tractor configuration. The tractor configuration also had a deeper stall when airspeed is at  $20\text{ms}^{-1}$ , which is undesirable to recover the MAV if a stall were to occur. The tractor configuration, in general, produced less drag than the pusher configuration. The MAV's stability analysis showed that the MAV model's pitching moment decreased as the angle of attack increased and indicated that the MAV was stable in all cases. The pusher configuration had a larger pitching moment compared with the no-propeller model, hence MAV became more stable in the pusher configuration. The tractor configuration showed the opposite, and the MAV became less stable in this configuration. The pusher configuration shifts the rolling moment to a more significant extent than the tractor configuration as it has a longer moment arm from the position of the propeller to the aerodynamic centre of the MAV model. Further investigation is required into the suitability of VAP 3.5 as a validation software for wing propeller interactions. Currently, the side forces and moment calculations are still in testing and based on discrepancies found with wind tunnel testing, further work is required.



# Table of contents

<b>List of figures</b>	<b>xvi</b>
<b>List of tables</b>	<b>xx</b>
<b>List of abbreviations</b>	<b>xxi</b>
<b>1 Introduction</b>	<b>1</b>
1.1 Problem Statement . . . . .	3
1.2 Objectives . . . . .	4
1.3 Outline . . . . .	5
<b>2 Background</b>	<b>6</b>
2.1 Aircraft Geometry . . . . .	6
2.2 Span . . . . .	6
2.3 Chord . . . . .	7
2.4 Sweep . . . . .	8
2.5 Dihedral . . . . .	8

---

## Table of contents

---

2.6	Twist and Incidence . . . . .	9
2.7	Aspect Ratio . . . . .	10
2.8	Reference Frames . . . . .	11
2.8.1	Earth Centered Axes: denoted as $(x_e, y_e, z_e)$ . . . . .	12
2.8.2	LVLH Axes: denoted as $(x_v, y_v, z_v)$ . . . . .	13
2.8.3	Body Axes: denoted as $(x_b, y_b, z_b)$ . . . . .	13
2.8.4	Stability Axes: denoted as $(x_s, y_s, z_s)$ . . . . .	14
2.8.5	Air Path Axes: denoted as $(x_a, y_a, z_a)$ . . . . .	14
2.9	Key Parameters . . . . .	14
2.10	Aerodynamic Forces and Coefficients . . . . .	15
2.11	Static Longitudinal Stability . . . . .	17
2.12	Static Lateral Stability . . . . .	19
2.13	Reynolds Number . . . . .	22
<b>3</b>	<b>Literature Review</b>	<b>23</b>
3.1	Proliferation of MAV's in the Aerospace Landscape . . . . .	23
3.2	Limitations of MAV Design Techniques . . . . .	24
3.3	Low Reynolds Number Effects . . . . .	25

---

**Table of contents**

3.3.1	Laminar Separation Bubbles and Vortices . . . . .	28
3.3.2	Non-Linear Lift Distribution . . . . .	30
3.4	Propeller Wing Interaction . . . . .	32
3.4.1	Stability Effects . . . . .	36
3.4.2	Aerodynamic Parameters . . . . .	37
3.4.3	The General Micro Aerial Vehicle . . . . .	37
3.4.4	Optimization Techniques and Validation . . . . .	38
<b>4</b>	<b>Theory and Methodology</b>	<b>40</b>
4.1	Material Choice . . . . .	40
4.2	FreeCAD . . . . .	41
4.3	VAP 3.5 . . . . .	43
4.4	XFOIL . . . . .	46
4.5	Wind Tunnel Testing . . . . .	47
4.6	Stability Calculation . . . . .	49
<b>5</b>	<b>Results and Discussion</b>	<b>50</b>
5.1	Wind Tunnel Results . . . . .	50
5.1.1	Aerodynamic Coefficient of Lift . . . . .	50

## Table of contents

---

5.1.2	Aerodynamic Coefficient of Thrust Minus Drag Force . . . . .	52
5.1.3	Pitching Moment Coefficient . . . . .	53
5.1.4	Rolling Moment Coefficient . . . . .	55
5.1.5	Yawing Moment Coefficient . . . . .	56
5.1.6	Static Margin . . . . .	58
5.2	VAP 3.5 Validation . . . . .	60
5.2.1	Wing Validation . . . . .	60
5.2.2	GenMAV model validation . . . . .	61
5.2.3	Validation of Wind Tunnel Results with VAP 3.5 . . . . .	62
5.2.3.1	No Propeller Configuration . . . . .	62
5.2.3.2	Tractor Configuration . . . . .	65
5.2.3.3	Pusher Configuration . . . . .	68
6	Conclusions and Future Work	72
6.1	Conclusions . . . . .	73
6.2	Future Work . . . . .	74
References		77
Appendix A	Wind Tunnel Results	87

---

**Table of contents**

<b>Appendix B Wing Validation</b>	<b>89</b>
-----------------------------------	-----------

# List of figures

1.1 MAV gross weight with wing span. Figure is adapted [6]. Image sources: [7–14]	2
1.2 Examples of MAVs with category	2
2.1 Aircraft geometric parameters	7
2.2 Wing dihedral and anhedral example. Image source: [32]	9
2.3 Wing twist and incidence angle	10
2.4 High and medium AR aircraft examples [33]	11
2.5 Aircraft reference frames	12
2.6 Earth centered axes [34]	13
2.7 Pressure distribution over a wing	15
2.8 Aerodynamic forces acting on MAV	16
2.9 Lift curve with respect to angle of attack	16
2.10 Position of center of gravity (CG), neutral point (NP) and aerodynamic center (AC)	18
2.11 General forces acting through the neutral point and center of gravity for a stable and unstable state	19

---

## List of figures

2.12 Relevant parameters when an aircraft undergoes a sideslip motion . . . . .	21
2.13 Moments acting on an aircraft . . . . .	21
3.1 MAV speed with Reynolds number region in respect to flying bodies. Figure is adapted [59]. Image sources: [60–63] . . . . .	25
3.2 Flow characteristics across the propeller when the propeller is turned off (a) and when the propeller is turned on (b) [65] . . . . .	26
3.3 Flow separation position change with Reynolds number [57] . . . . .	27
3.4 Anatomy of laminar separation bubbles. Figure adapted from Mohamed [74] . . . . .	28
3.5 Airfoil aerodynamic performance variation with increasing: (a) turbu- lence intensity (b) length scale [74] . . . . .	29
3.6 Flow patterns shown by smoke. Laminar flow to turbulence without surface roughness (a). Laminar flow for with a rough surface (b). [77] .	30
3.7 Development of wingtip vortices over a wing section [82] . . . . .	31
3.8 Tangential and Axial velocity effects [95] . . . . .	33
3.9 Effect of propeller slipstream on the lift coefficient curve with angle of attack ( $Re = 0.3 \times 10^5$ ) [96]. . . . .	33
3.10 Propeller slipstream effect with span-wise location for airflow transition over the wing upper surface, $\alpha = 2.5^\circ$ [96]. . . . .	34
3.11 Influence areas related to propeller-wing interaction based on the loading distributions [101] . . . . .	35

## List of figures

---

3.12	Blade angle of attack variation due to propeller pitch angle [101] . . . . .	36
3.13	GenMAV Model [106] . . . . .	38
3.14	Unique constraints of MAVs [74] . . . . .	39
4.1	Final model for wind tunnel testing in FreeCAD . . . . .	41
4.2	Dimensions of the final MAV model in millimeters . . . . .	42
4.3	FreeCAD model mounted in Wing tunnel . . . . .	42
4.4	VAP 3.5 main steps to setup, run and return results from simulation . .	44
4.5	Visualisation of a single distributed vorticity element. The leading and trailing edge vortices are represented by $\Gamma_{l,e}$ and $\Gamma_{t,e}$ , respectively. The quadratic circular distribution is in the spanwise $\eta$ direction, and the leading and trailing edge vortices are joined in the streamwise direction by a linear changing distribution vorticity strength indicated by $\gamma$ in the spanwise direction [118]. . . . .	45
4.6	Safety measures taken to ensure no damage is done to any people or to the wind tunnel itself. . . . .	47
4.7	Wind tunnel mount and load cell used . . . . .	48
4.8	Examples of MAVs with category . . . . .	48
4.9	Calibrating pitch of model mount to ensure AoA is accurate . . . . .	49
5.1	Coefficient of lift variation with various conditions for the pusher, tractor and no propeller configurations . . . . .	51

---

**List of figures**

5.10 No propeller configuration showing the start of the wake interference when run through VAP 3.5 at a sideslip angle of $15^\circ$ . . . . .	64
5.12 VAP 3.5 simulation of tractor configuration showing propeller-wing wake interference . . . . .	65
A.1 Coefficient of drag variation at 20ms airspeed for the tractor, pusher and no propeller configuration . . . . .	87

# List of tables

5.1 Static margin of all three configurations tested at airspeeds of $10\text{ms}^{-1}$ and $20\text{ms}^{-1}$ , and propeller speeds of 6000RPM and 11000RPM . . . . .	59
--	----

# List of abbreviations

$\lambda$  Taper ratio.

$\Lambda$  Sweep.

$\gamma$  Dihedral angle.

$\alpha$  Angle of Attack.

$\beta$  Side slip angle.

$\theta_i$  Wing incidence angle.

$\theta_t$  Wing twist angle.

$C_{L_{alpha}}$  Lift coefficient at an angle of attack of  $0^\circ$ .

$c_r$  Root chord of wing.

$c_t$  Tip chord of wing.

$x_e$  x-axis of an Earth centered frame of reference.

$y_e$  y-axis of an Earth centered frame of reference.

$z_e$  z-axis of an Earth centered frame of reference.

**AC** Aerodynamic Center.

**AoA** Angle of Attack.

**AR** Aspect Ratio.

**AVL** Athena Vortex Lattice.

## **List of abbreviations**

---

**b** Wingspan.

**CAD** Computer aided design.

**CFD** Computational Fluid Dynamics.

**CG** Center of Gravity.

**DVE** Distributed Vortex Element.

**e** Oswald efficiency factor.

**FIM** Full Interaction Mode.

**GenMAV** Generic Micro-Aerial Vehicle.

**GPS** Global Positioning System.

**HOFW** High-Order Free Wake.

**LSB** Laminar separation bubbles.

**LVLH** Local-vertical local-horizontal.

**MAC** Mean Aerodynamic Chord.

**MAV** Micro Aerial Vehicle.

**NP** Neutral Point.

**Open VSP** Open Vehicle Sketch Pad.

**PLA** Polylactic acid.

**q** Dynamic pressure.

**Re** Reynolds Number.

---

## List of abbreviations

**RPM** Revolutions per minute.

**s** semi-span.

**S** Wing area.

**SDVE** surface distributed vorticity element.

**UAV** Unmanned aerial vehicle.

**VLM** Vortex Lattice Method.

**VSP** Vehicle Sketch Pad.



# Chapter 1

## Introduction

Unmanned aerial vehicles (UAVs) are used throughout various industries to conduct missions that are either dangerous, difficult or dull for humans to perform. Recently UAVs have seen unprecedented growth for both commercial [1] and military [2, 3] use. The capability to fly within narrow spaces gives Micro Aerial Vehicles (MAVs) a significant advantage over general UAVs in specific use cases. MAVs, in particular, are more manoeuvrable in cluttered environments, such as, collapsed buildings, commercial centres, and search and rescue missions. Given current technology, MAVs could provide coordinates of trapped victims in areas where it would be dangerous to search manually [4]. Possible applications of MAVs include dangerous gas detection, environmental monitoring, border patrol, mapping, precision agriculture, homeland security, and drug interdiction [1, 4]. MAVs ability to be much quieter and concealed give it a major advantage over UAVs [2].

Today defence programs around the world utilize UAVs for reconnaissance, surveillance, damage assessments, and communication relay [2–4]. MAVs have even more recently seen major research interest, particularly in the last decade [4]. The relative size of MAVs to other typical aircraft is shown in Figure 1.1. Smaller vehicles are intended to lower the total cost of systems currently used and increase the portability of MAVs [5]. The most significant factors for MAV design, are current limitations in propulsion, configuration, and flight control [5].

## Introduction

---

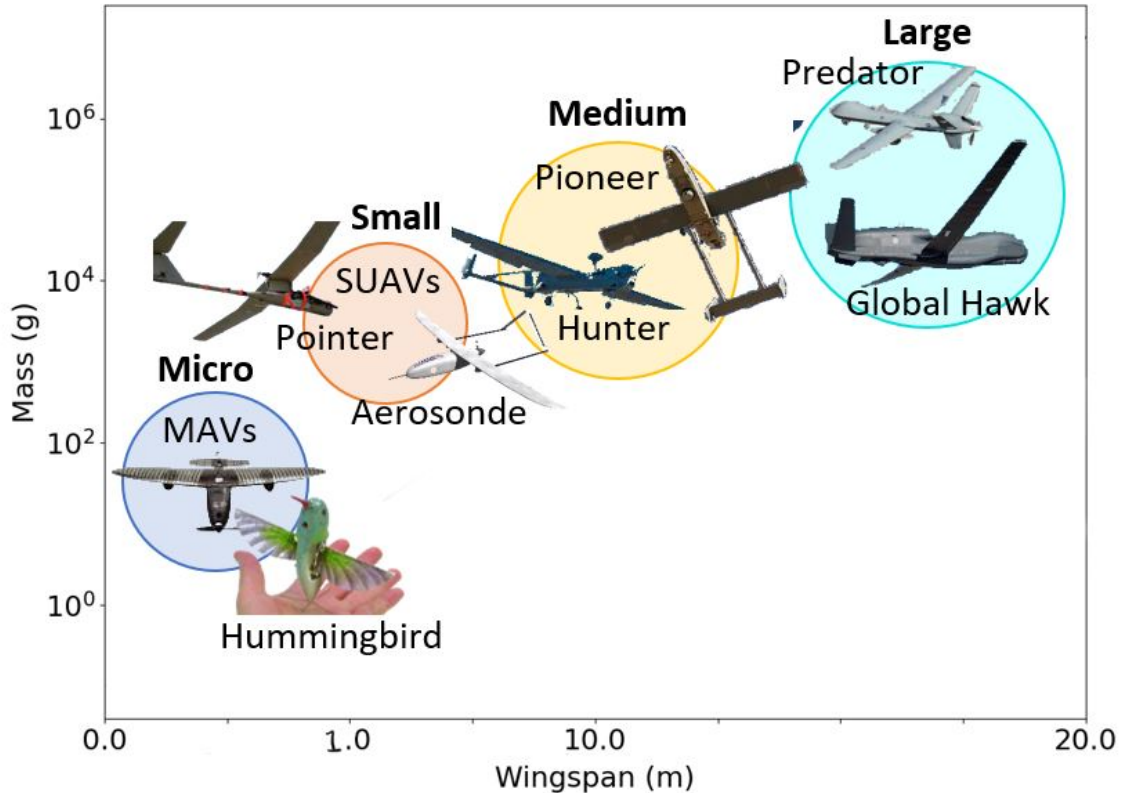


Fig. 1.1 MAV gross weight with wing span. Figure is adapted [6]. Image sources: [7–14]

MAVs fall into three main categories. These are fixed wings [15], rotary wings [16] and flapping wings [17], which can also be used in combination.

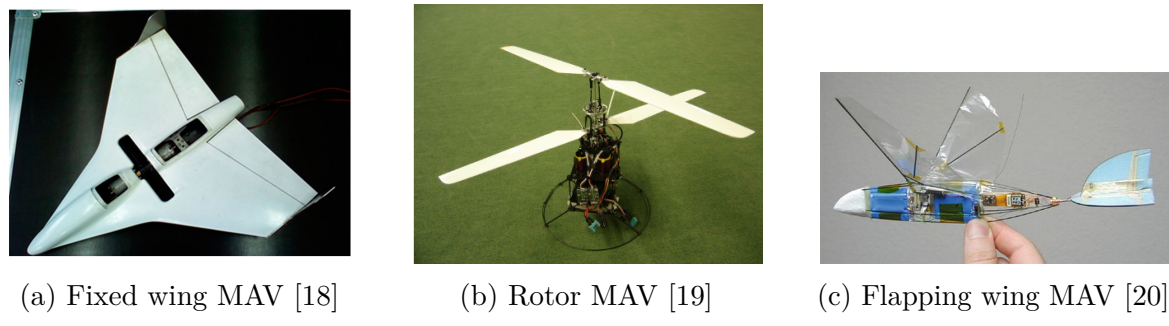


Fig. 1.2 Examples of MAVs with category

## **1.1 Problem Statement**

---

MAVs are much more difficult to design and manufacture than typical aircraft [21]. This additional complexity is due to several factors:

- Low speed flight
- Small physical dimensions
- Structural strength
- Reduced stall speed due to smaller size
- Low inertia

With the increased complexity of MAV designs, there has also been an increased interest in the research and design of optimised MAV models [21]. Design software to optimise MAV designs is generally based on aerodynamic properties, weights, stability, and maneuverability [22–24]. The low-speed and non-linear flight dynamics are of particular importance for MAV development [25, 26]. The low speeds that MAVs fly at and the influence of an operating propeller on the rest of the MAV is currently unvalidated with physical wind tunnel testing. This thesis aims to fill in this gap.

### **1.1 Problem Statement**

In the past, surveillance was conducted initially from hot air balloons. Later, aircraft such as helicopters would be used, costing companies large sums of money to survey from a bird's eye view [27]. Today drones and UAVs often conduct this work, within certain limits due to range and flight time [28, 27]. The next significant technology jump sees the optimisation and miniaturisation of these aircraft to produce MAVs. MAVs are set to increase the ability to conduct a variety of missions that predominately have military or surveillance objectives [27, 29–31].

## **Introduction**

---

The MAV's main deferring attributes are; its smaller size, lower radar visibility and lower noise output. With MAV design becoming one of the fastest-growing areas of development in the aerospace industry, there is an increasing need to have accurate experimental data to validate, simulate and model the numerous MAV configurations being investigated. One of the core but currently missing pieces to this puzzle is the influence and effect of propellers on the aerodynamics and stability of MAVs. Can we further deepen our understanding of MAVs by analysing these effects?

## **1.2 Objectives**

The objectives of this thesis are as follows:

1. To review current published literature and determine areas with insufficient or no research available for further development and research.
2. To design and produce a 3D model of a MAV with a detachable propeller to allow for both tractor and pusher configurations.
3. To conduct wind tunnel testing of the MAV model with and without propeller effects.
4. To analyse data of wind tunnel results and detail the effect propellers have on the MAV model.
5. To validate results with VAP 3.5 software and give insights into the accuracy of VAP 3.5 when accounting for propeller-wing interactions.

## 1.3 Outline

An outline of the contents of this thesis submission is listed below.

- **Chapter 2: Background**

Outlines the core theory and relevant literature for understanding current MAV technology, provides information surrounding the key issues to be addressed, and justifies the study's need.

- **Chapter 3: Literature Review**

Collates the current information relating to MAVs and propeller effects. This chapter also details the significance of low Reynolds number flight. Previous studies and current literature are outlined here, along with how this study will extend or differ from previous work.

- **Chapter 4: Methodology**

This chapter outlines the Methodology to develop the MAV model from python scripts and FreeCAD software, model development, complete wind tunnel testing and validation of results using VAP 3.5.

- **Chapter 5: Results**

Discusses the study's final results, provides insights as to why these results have occurred and compare these results with validation cases from VAP 3.5.

- **Chapter 6: Discussion and Future Work**

This chapter explains the results, summarizes the main findings of this thesis and recommends future work to be investigated.

# Chapter 2

## Background

This chapter outlines the core theory and topics relevant for optimising MAVs and literature regarding the effect of propeller interactions on MAVs. Crucial coefficients, concepts and terminology are explained here. This section will cover general aircraft geometry, aerodynamic forces, reference frames, longitudinal stability, lateral stability and Reynolds number.

### 2.1 Aircraft Geometry

Several aircraft geometric parameters will be referred to throughout this thesis. Key parameters discussed are the wingspan, chord length, aspect ratio, sweep, dihedral and twist. Figure 2.1 shows some of these.

### 2.2 Span

The wingspan ( $b$ ) is the distance from one wing tip to the other. The semi-span ( $s$ ) is the distance from the fuselage reference line to the wing tip. These parameters are also shown in Figure 2.1.

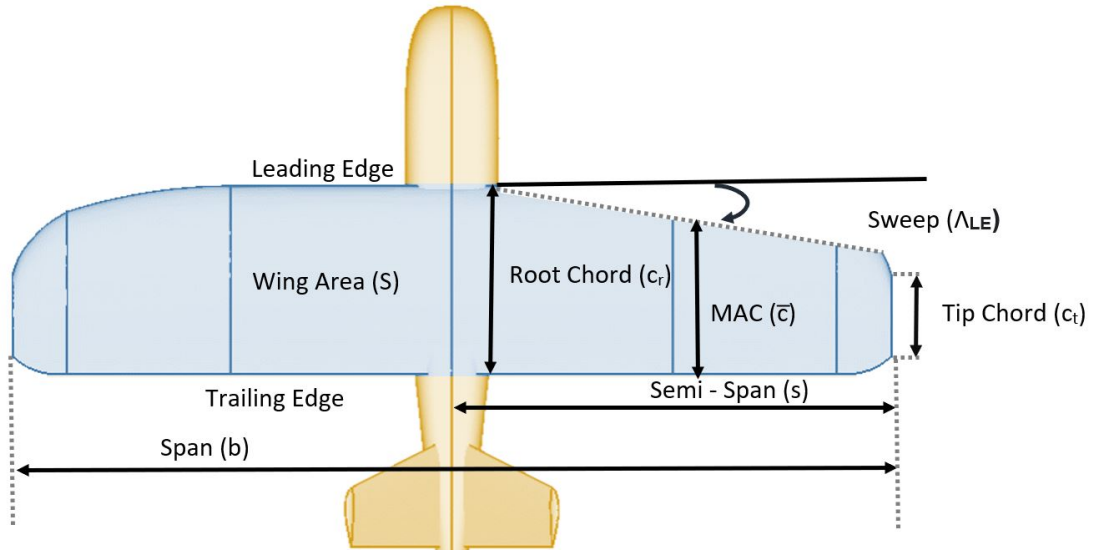


Fig. 2.1 Aircraft geometric parameters

## 2.3 Chord

The chord is the distance between the leading and trailing edge of the wings shown in Figure 2.1. The chord is often defined in terms of three main parameters, these are:

- **Root Chord (denoted  $c_r$ ):** This is the chord length where the wing meets the fuselage and is generally the position where the chord length is the longest.
- **Tip Chord (denoted  $c_t$ ):** The tip chord is the chord length at the tips of the wings
- **Mean Aerodynamic Chord (MAC):** The mean aerodynamic chord is used to represent the wing in only two dimensions. The MAC is the chord length at which the resultant aerodynamic force acts. The MAC is defined by Equation 2.1 and is taken from wing tip to wing tip.

## Background

---

$$\bar{c} = \frac{\int_0^b c(y)^2 dy}{\int_0^b dy} \quad (2.1)$$

Taper ratio is the ratio between the root and tip chord lengths given by Equation 2.2.

$$\lambda = \frac{c_t}{c_r} \quad (2.2)$$

The taper ratio is significant as it influences the lift distribution over the wing. Reducing the wing area towards the wing tips, reduces the moment produced by the wings.

## 2.4 Sweep

The sweep is the angle ( $\Lambda$ ) between the  $y_b$  axis and the leading edge. When wings are swept back, the flow is directed outwards along the length of the wing. This also changes the angle of attack towards the wings' tips. A negative sweep angle (generally only seen on experimental aircraft) directs the flow inboard towards the fuselage. Sweep is also used to assist with static longitudinal stability. A positive sweep angle will move the aircraft's aerodynamic center backwards and vice versa. The sweep angle ( $\Lambda$ ) can be used to fine-tune the pitch stability. Sweep is also used to delay shock wave formation on wings.

## 2.5 Dihedral

The dihedral angle ( $\gamma$ ) is the angle between the wing and the  $y_b$  axis, which is represented by the horizontal dotted line in Figure 2.2. A dihedral angle is when the wing tip is at a higher point than the root of the wing. This is the opposite for the case of an

anhedral angle, also shown in Figure 2.2. Having a dihedral angle increases the lateral stability - particularly when banking, as the lower wing will fly at a higher angle of attack than the higher wing.

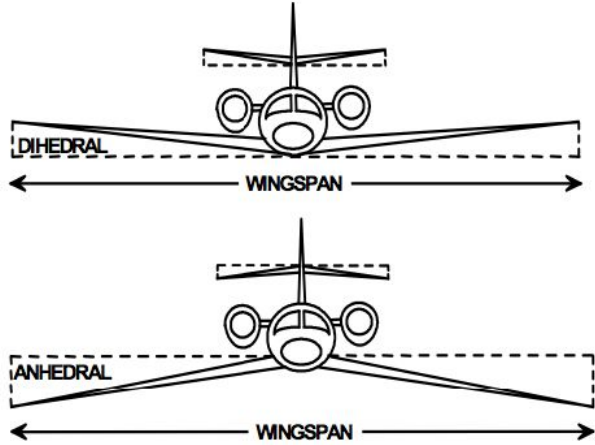


Fig. 2.2 Wing dihedral and anhedral example. Image source: [32]

## 2.6 Twist and Incidence

The wing twist angle ( $\theta_t$ ) is the angle between the tip chord reference line and the root chord. By convention, a positive wing twist angle is defined as a downward twist on the wing. Figure 2.3 shows an example of this. Another significant parameter is the wing incidence angle ( $\theta_i$ ) which is the angle between the fuselage reference line and the root chord line. In this case, a positive incidence angle is defined as an upward twisted root chord.

The wing twist is often used to redistribute the lift along the wing's surface. The wing tip is the last wing surface that will experience stall; particularly when in a steep climb or roll manoeuvre. By twisting the wingtip downwards with respect to the rest of the wing, the effective angle of attack will be lower at the wingtip than at the root. This

## Background

---

means that the root will stall before the wingtip. This is desirable as control surfaces such as ailerons lose their effectiveness when the wingtips stall first.

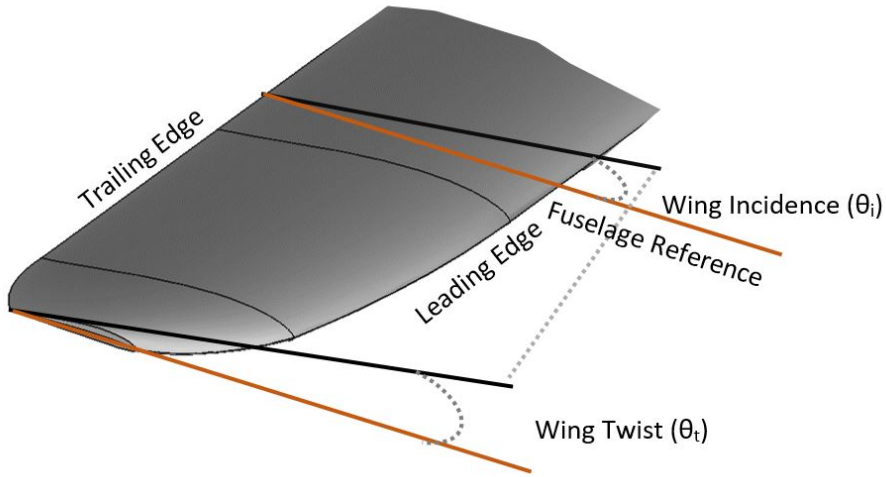


Fig. 2.3 Wing twist and incidence angle

## 2.7 Aspect Ratio

The aspect ratio (AR) is significant when considering an aircraft's aerodynamic efficiency. First, the wing area (S) must be introduced. The AR can be calculated through Equation 2.3.

$$AR = \frac{b^2}{S} \quad (2.3)$$

Where b is the wing span and S is the total platform area of the wing, also shown in Figure 2.1, as the area coloured blue.

Higher aspect wings produce less lift-induced drag - however, they often require more structural support and are typically heavier than lower AR aircraft. High aspect wings

are long and thin, whilst low aspect wings are short and wide. Figure 2.4 shows two aircraft with high and medium ARs. The Schleicher aircraft shown has a much higher AR. This also means it has high aerodynamic efficiency.



Fig. 2.4 High and medium AR aircraft examples [33]

## 2.8 Reference Frames

The primary reference frames used to describe the position of an aircraft are:

- Earth Centered Axes
- Local-vertical local-horizontal (LVLH) Axes
- Body Axes
- Stability Axes
- Air Axes

Figure 2.5 provides a visualisation to assist with the following explanations.

## Background

---

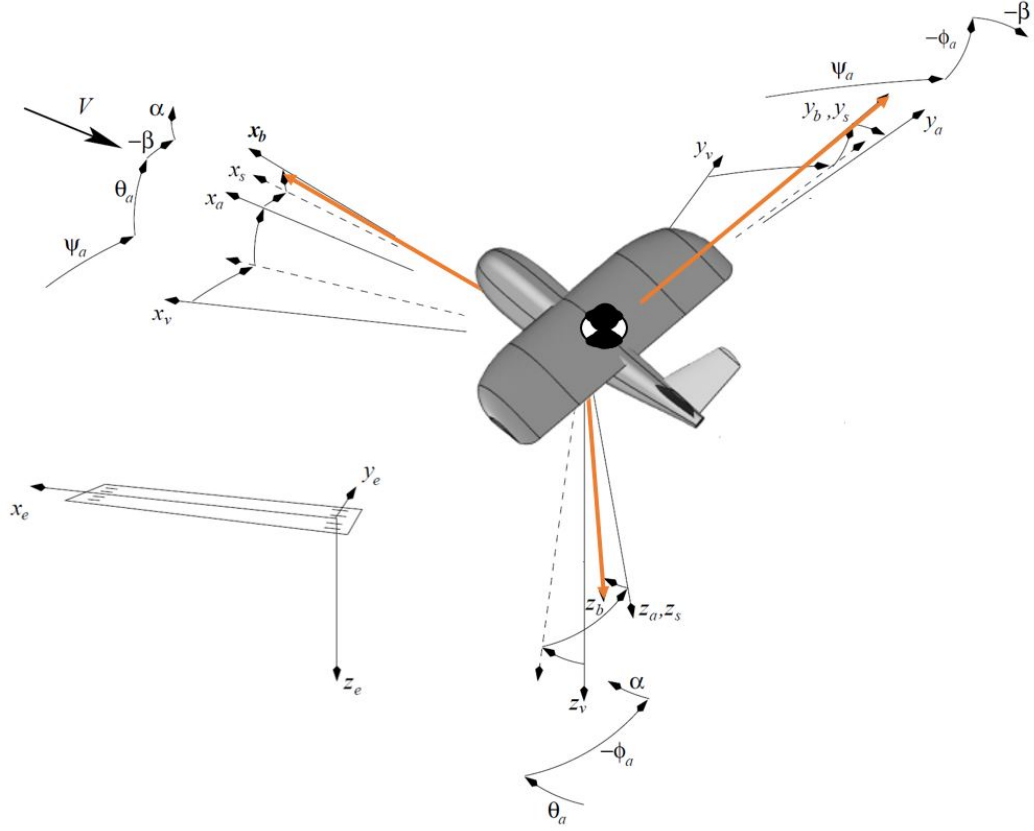


Fig. 2.5 Aircraft reference frames

### 2.8.1 Earth Centered Axes: denoted as $(x_e, y_e, z_e)$

The Earth centered axes is a global reference frame with the centre of the Earth's origin. From the Earth's centre, three orthogonal axes remain fixed to the Earth. This axis is primarily used when describing the position of aircraft. Further visualisation of this reference frame is shown in Figure 2.6. As Earth has an ellipsoid shape (rather than a sphere), the position is described in terms of the latitude ( $\phi$ ), longitude ( $\lambda$ ), and altitude (h).

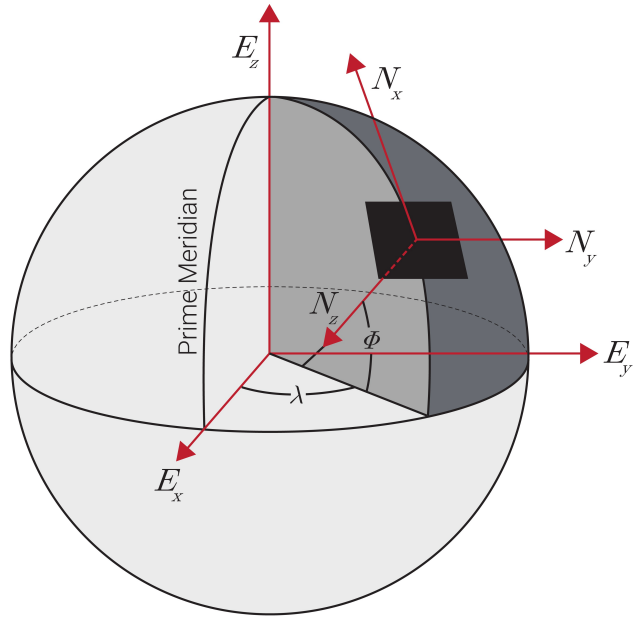


Fig. 2.6 Earth centered axes [34]

### 2.8.2 LVLH Axes: denoted as $(x_v, y_v, z_v)$

This axis frame translates with the aircraft and is aligned with the Earth axes previously described. It is shown in Figure 2.5.

### 2.8.3 Body Axes: denoted as $(x_b, y_b, z_b)$

This axis is positioned at the aircraft's centre of gravity. Figure 2.5 shows this position in the aircraft's centre. The body axes translate with the aircraft and are highlighted in orange in Figure 2.5.

## Background

---

### 2.8.4 Stability Axes: denoted as $(x_s, y_s, z_s)$

The stability axis has its origin at the centre of gravity, shown in Figure 2.5. It translates with the aircraft's movement.  $x_s$  aligns with the air path and is described as an offset from  $x_b$  by an angle of  $\alpha$  (further described in 2.9).  $y_s$  is aligned with the body axes  $y_b$  and  $z_s$  acts perpendicular to both  $x_s$  and  $y_s$ .

### 2.8.5 Air Path Axes: denoted as $(x_a, y_a, z_a)$

The air path axis has its origin at the centre of gravity.  $x_a$  and  $y_a$  are aligned with the relative air path and is offset from  $x_b$  by the angle of attack ( $\alpha$ ) and  $y_b$  by the sideslip angle ( $\beta$ ) respectively.  $z_a$  is perpendicular to both  $x_a$  and  $y_a$ .

## 2.9 Key Parameters

Some key parameters are used to define the motion of the aircraft. These are explained below:

- **Aerodynamic Angles  $(\alpha, \beta)$ :** These angles are used to describe the offset of the aircraft's body axes to the relative air path.  $\alpha$  is also known as the angle of attack and describes the angle between the  $x_a$  and  $x_b$  positions.  $\beta$  is also known as the side slip angle and describes the angle between the  $y_a$  and  $y_b$  positions. These angles are also shown in Figure 2.5.
- **Euler Angles  $(\theta_a, \phi_a, \psi_a)$ :** The Euler angles are used to describe the orientation of rigid bodies with respect to a fixed coordinate system. In the case of aircraft, this describes the pitch ( $\theta_a$ ), yaw ( $\psi_a$ ) and roll ( $\phi_a$ ). These angles are relative to the LVLH reference frame. These can be seen in Figure 2.5.

## 2.10 Aerodynamic Forces and Coefficients

Airfoils produce lift due to a pressure difference between the upper and lower surface in a moving fluid. This lift force acts perpendicular to the chord line shown in Figure 2.7.

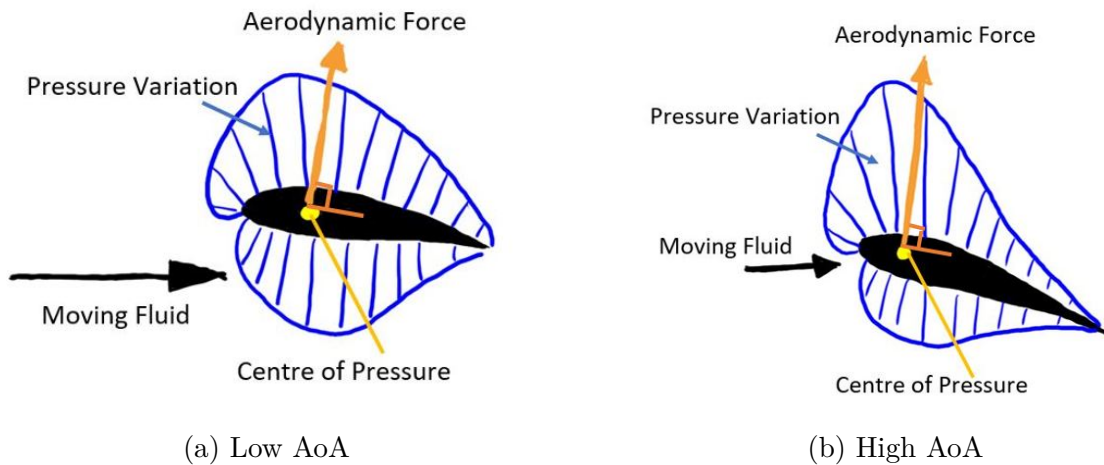


Fig. 2.7 Pressure distribution over a wing

To simplify calculations the aerodynamic centre is used. The wing's aerodynamic centre is the wing's position where when the net force is applied, and the total moment created with respect to the angle of attack remains constant. The total force acts through the aerodynamic centre. The main forces which act on the wing are lift and drag. Lift ( $L$ ) is the force acting normally on the air path axes ( $z_a$ ). Drag ( $D$ ) is the force that acts both in the  $x_a$ , air path axis and along the aircraft surface due to air friction. The main forces are also shown in Figure 2.8. Two significant aerodynamic coefficients are used as the lift and drag force coefficients shown in Equations 2.4 and 2.5. These coefficients are the lift and drag forces normalised by the dynamic pressure ( $q$ ) and the wing area ( $S$ ).

## Background

---

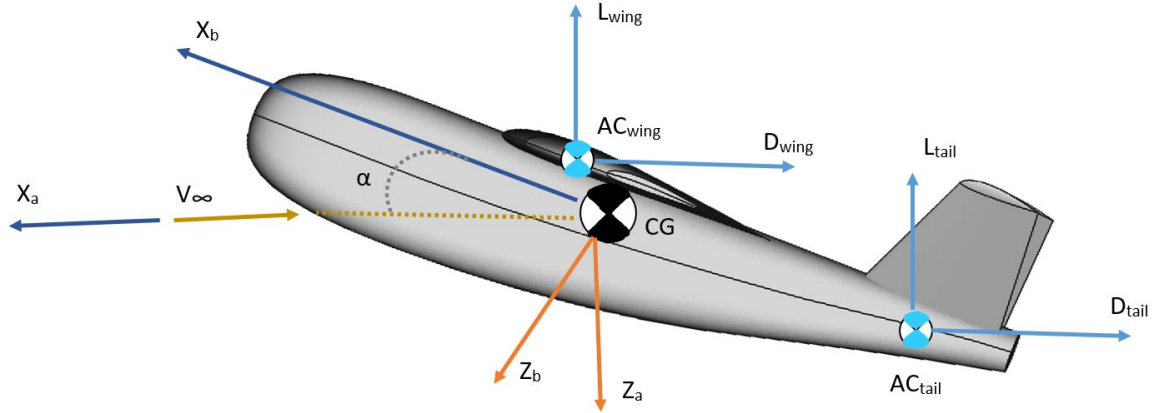


Fig. 2.8 Aerodynamic forces acting on MAV

$$C_L = \frac{L}{qS} = \frac{L}{\frac{1}{2}\rho V_\infty^2 S} \quad (2.4)$$

$$C_D = \frac{D}{qS} = \frac{D}{\frac{1}{2}\rho V_\infty^2 S} \quad (2.5)$$

The lift coefficient is described in terms of the AoA, the lift coefficient at an AoA of 0 ( $C_{L_0}$ ) and the slope of the lift curve with respect to the AoA ( $C_{L\alpha}$ ) shown in Figure 2.9 which can be modelled by Equation 2.6

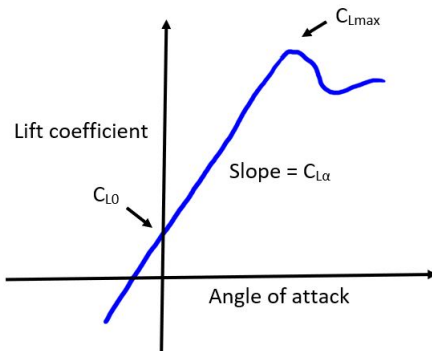


Fig. 2.9 Lift curve with respect to angle of attack

$$C_L \approx C_{L_0} + C_{L_\alpha} \alpha \quad (2.6)$$

Equation 2.6 is accurate at small angles of attack where the lift curve slope is linear as shown in Figure 2.9. The lift curve slope at higher angles of attack becomes non-linear due to flow separation, and hence Equation 2.6 is an inaccurate approximation. Drag can be estimated through Equation 2.7, where  $C_{D_0}$  is the drag due to skin friction and  $e$  is the Oswald efficiency factor. The Oswald efficiency factor measures the lift distribution efficiency across a wing.

$$C_D \approx C_{D_0} + \frac{C_L^2}{\pi A Re} \quad (2.7)$$

## 2.11 Static Longitudinal Stability

Static longitudinal stability is determined from the pitching moment  $C_M$ . The pitching moment is defined as shown in Equation 2.8.

$$C_M = \frac{M}{\frac{1}{2} \rho V_\infty^2 S \bar{c}} \quad (2.8)$$

The derivative of the pitching moment with respect to the angle of attack must be negative with a positive AoA to be stable. This is also given in Equation 2.9.

$$C_{M_\alpha} = \frac{\delta C_M}{\delta \alpha} < 0 \quad (2.9)$$

The aerodynamic centre of the aircraft is also referred to as the neutral point. The total aerodynamic force acts through the neutral point and is the position where no

## Background

---

change in pitching moment is seen with a variation in the angle of attack ( $C_{M\alpha} = 0$  when  $x_{cg} = N_0$ ). Figure 2.10 shows the parameters on the aircraft. When the position of the centre of gravity is the same as the neutral point, the aircraft is neutrally stable.

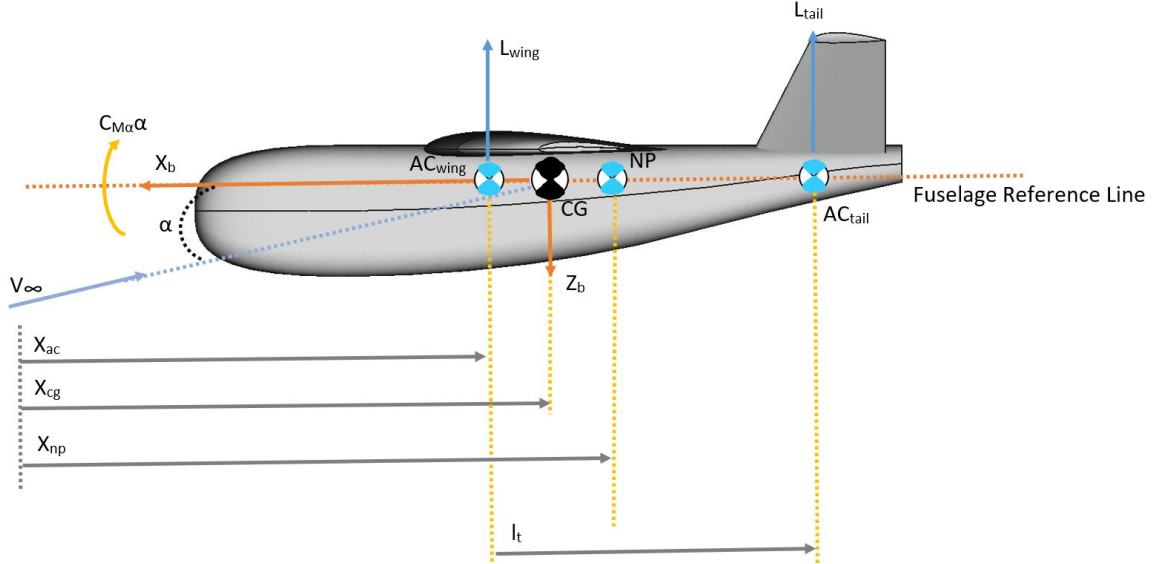


Fig. 2.10 Position of center of gravity (CG), neutral point (NP) and aerodynamic center (AC)

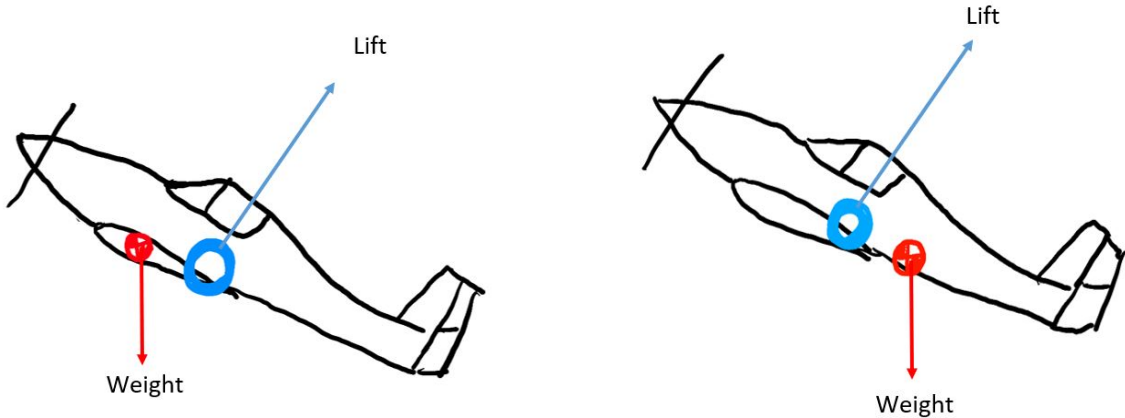
Another important concept for stability is the static margin. The static margin is defined as the distance between the neutral point and the centre of gravity indicated in Figure 2.10. The static margin is expressed as a percentage of the mean aerodynamic chord length and is given in Equation 2.10. A large static margin indicates that an aircraft is stable.

$$C_{M\alpha} = C_{L\alpha} \left( \frac{x_{cg}}{c} - N_0 \right) \quad (2.10)$$

If the centre of gravity is positioned too far forward, the pitching stiffness coefficient becomes negative with a large magnitude. Aircraft in this state require large control surface deflections to be manoeuvrable. Aircraft are designed with this stability in mind, and the pitch stiffness is placed within reasonable controllability and stability

## 2.12 Static Lateral Stability

limitations. Figure 2.11 shows the stability difference when moving the center of gravity and neutral point locations.



(a) When the center of gravity is ahead of the neutral point then the weight tends to correct this displacement (stable).

(b) When center of gravity is behind the neutral point the weight worsens the displacement (unstable).

Fig. 2.11 General forces acting through the neutral point and center of gravity for a stable and unstable state

## 2.12 Static Lateral Stability

Static lateral stability is determined by the roll moment  $l$  and yaw moment  $n$ . Similarly to how the lift and drag coefficients were normalised, the roll and yaw moments can be normalised to form their coefficient forms. These Equations are given in 2.11 and 2.12.

$$C_l = \frac{l}{\frac{1}{2}\rho V_\infty^2 S b} \quad (2.11)$$

$$C_n = \frac{n}{\frac{1}{2}\rho V_\infty^2 S b} \quad (2.12)$$

## Background

---

The lateral stability of an aircraft is based on the change in  $C_n$  and  $C_l$  with respect to disturbances in the sideslip angle. A further parameter can be determined from the yaw moment by taking the derivative with respect to the sideslip angle. This is given in Equation 2.13. This is also known as yaw stiffness.

$$C_{n_\beta} = \frac{\delta C_n}{\delta \beta} > 0 \quad (2.13)$$

A positive sideslip angle change for directional stability must produce a positive yaw moment change. A positive yaw moment shifts the aircraft to re-align the body and wind axes, reducing the sideslip angle. This is described in Equation 2.13.

Similarly, the derivative of the roll moment with respect to the sideslip angle can be used to determine the dihedral effect shown in Equation 2.14.

$$C_{l_\beta} = \frac{\delta C_l}{\delta \beta} < 0 \quad (2.14)$$

A positive sideslip angle change will produce a negative rolling moment to be laterally stable. This causes an aircraft to roll away from the relative wind flow. Hence a yawing movement to align with the air path is produced. This condition is given in Equation 2.14.

However, it is possible to have an aircraft that meets these criteria but is still hard to control. If the yaw or roll is too stiff (i.e.  $C_{n_\beta}$  is positive with a large magnitude and  $C_{l_\beta}$  is negative with a large magnitude), then the aircraft can still become impossible to manoeuvre. Hence the limitations of  $C_{n_\beta}$  and  $C_{l_\beta}$  are primarily limited by the actual controllability of the aircraft.

## 2.12 Static Lateral Stability

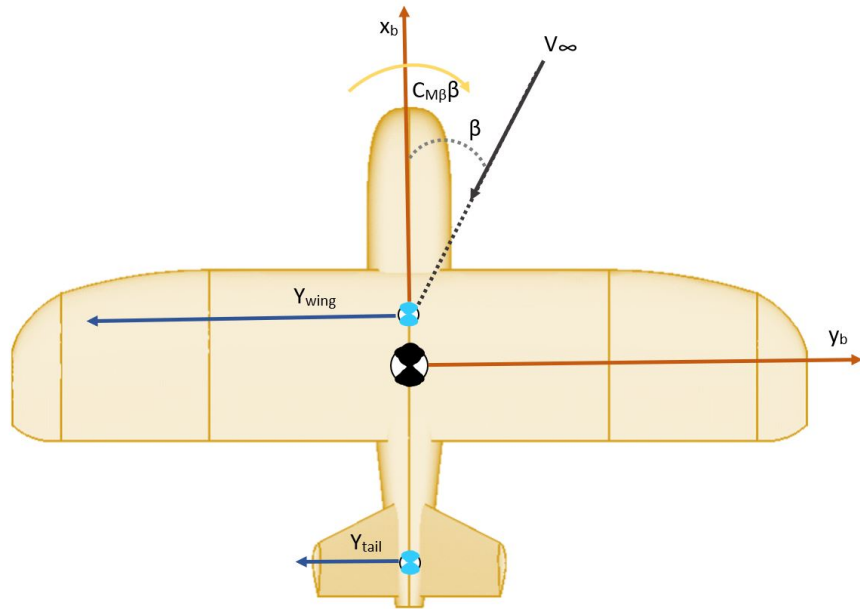


Fig. 2.12 Relevant parameters when an aircraft undergoes a sideslip motion

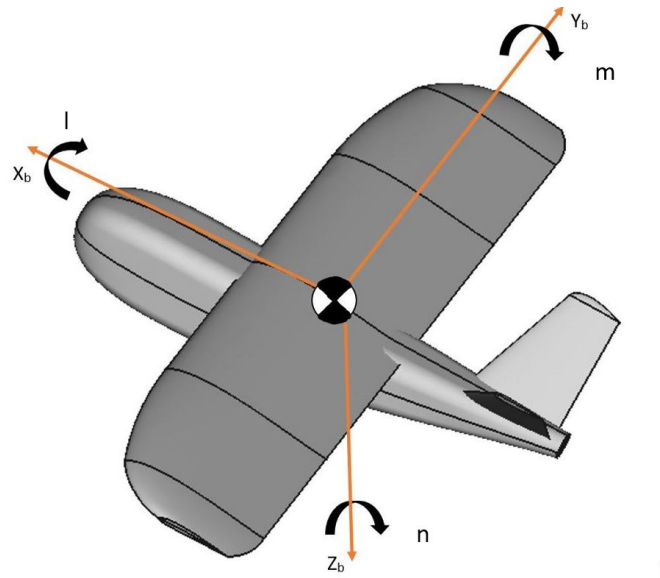


Fig. 2.13 Moments acting on an aircraft

## 2.13 Reynolds Number

Reynolds number is a dimensionless number used to represent the ratio of inertial forces to viscous forces. It is expressed in Equation 2.15 where:

- $\nu$  represents the kinematic viscosity of the fluid.
- $\rho$  represents the density of the fluid (air in this case).
- $u$  is the flow speed.
- $L$  is a characteristic length. In the case of aircraft, this is typically the length of the chord of the wing.
- $\mu$  is the dynamic viscosity of the fluid.

$$Re = \frac{\rho u L}{\mu} = \frac{u L}{\nu} \quad (2.15)$$

The Reynolds number is a parameter for describing the flow of the fluid being investigated. High Reynolds values ( $> 10^6$ ) indicate that the viscous forces only account for a small amount of the flow and hence the flow is essentially inviscid. For low Reynolds number values ( $< 10^5$ ), the viscous forces account for a significant portion of the flow and must be considered.

# Chapter 3

## Literature Review

This chapter contains a review of the current literature published on MAV development and the extent to which propeller effects have been researched. It explores the effects that propellers have on MAVs, current research on non-linear lift distributions, separation bubbles and propeller interactions and effects.

### 3.1 Proliferation of MAV's in the Aerospace Landscape

Initially introduced during World War I, UAVs were heavily criticized due to inaccuracies and unreliability when performing missions. Few saw the potential and impact they could have in changing the landscape of a battlefield [35]. UAVs have existed for centuries, although the modern era of UAVs commonly refers to the last four decades [36].

It was not until Operation Desert Storm (1991) and the Balkan Peninsula conflict that the development and interest in UAVs took off [35, 37]. The U.S. at the time saw a total income of \$2.27 billion dollars [35] (a 9.5% increase from the previous year of 1996). This marked a turning point in the the development of more complex UAVs [38] as the U.S. Department of Defense funded UAV research for the first time in 1996 [39]. The recent shift to the miniaturisation of components, systems and aerial vehicles has

## Literature Review

---

already influenced the military sector [27, 29], with several developments underway to reduce the visibility of reconnaissance aircraft and reduce the likelihood of aircraft being detected during missions [30, 31]. The most famous military MAV arguably being the Honeywell RQ-16 T-Hawk [40] which was mainly used by the U.S. forces in Iraq to search for roadside bombs [41]. The success of which (largely due to its hovering feature) led the U.S. Navy to order a further 372 MAVs [42].

What started as a small initial interest in smaller and smarter drones has resulted in exponential growth in the sector [28, 43]. Technology improvements have led to the exponential growth in the capabilities of MAV seen today [44, 45]. Where an initial drone supported only low camera resolution with meagre flight times, today incorporates several systems such as gyro stabilisation, GPS capability with way-point guidance, beyond the line of vision control, speeds of 70 km/h with a 30 minute flight time, and a 20-megapixel camera (DJI Phantom 4) [46].

## 3.2 Limitations of MAV Design Techniques

While MAV technology is more accessible and viable to the mass market than it has ever been before [45], there is no fully developed and validated way to optimize a MAV for a specified mission [47, 48]. Today, procedures involve developing a CAD model of the MAV or using software based on aerodynamics. This model is either then run through aerodynamic optimization software and/or tested in a wind tunnel to determine the main characteristics of the MAV [49]. The largest drawback of which is the lack of propeller effects accounted for, which are known to have a large effect on aerodynamics and stability [50, 51]. MAV model tests have been conducted with a fixed position propeller [52, 53]. Models are, however, typically tested without a spinning propeller, although these have been included in several aerodynamic software programs and specific tests [25].

### 3.3 Low Reynolds Number Effects

---

However, a lack of validation from wind tunnel testing means that a full understanding of the effects a propeller has on MAVs has not been achieved. MAVs are small relative to the size of the propellers used. Hence, the propeller will significantly affect the stability, noise, overall endurance, performance and power consumption of a given MAV [54, 55].

## 3.3 Low Reynolds Number Effects

Due to the small size and Reynolds numbers at which MAVs operate (typically around  $Re=10^5$  [56] [57]), insects and other small animals are often studied to understand the flight dynamics which occur for small flying bodies [58]. The Reynolds region in which MAVs typically fly is shown in Figure 3.1.

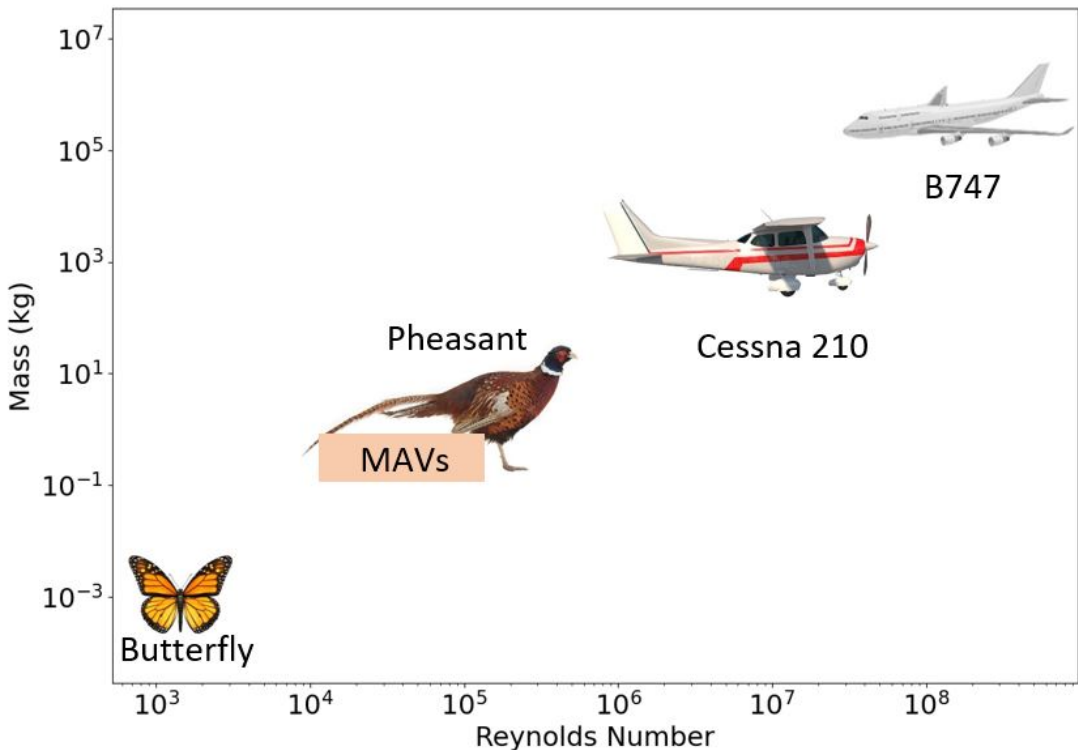


Fig. 3.1 MAV speed with Reynolds number region in respect to flying bodies. Figure is adapted [59]. Image sources: [60–63]

## Literature Review

---

Null used wind tunnel tests to show that propellers on wings during low Reynolds flight increased the performance of the wing at high angles of attack [64]. Ananda also visualised this effect as shown in Figure 3.2, however this is without the propeller being mounted on the wing directly.

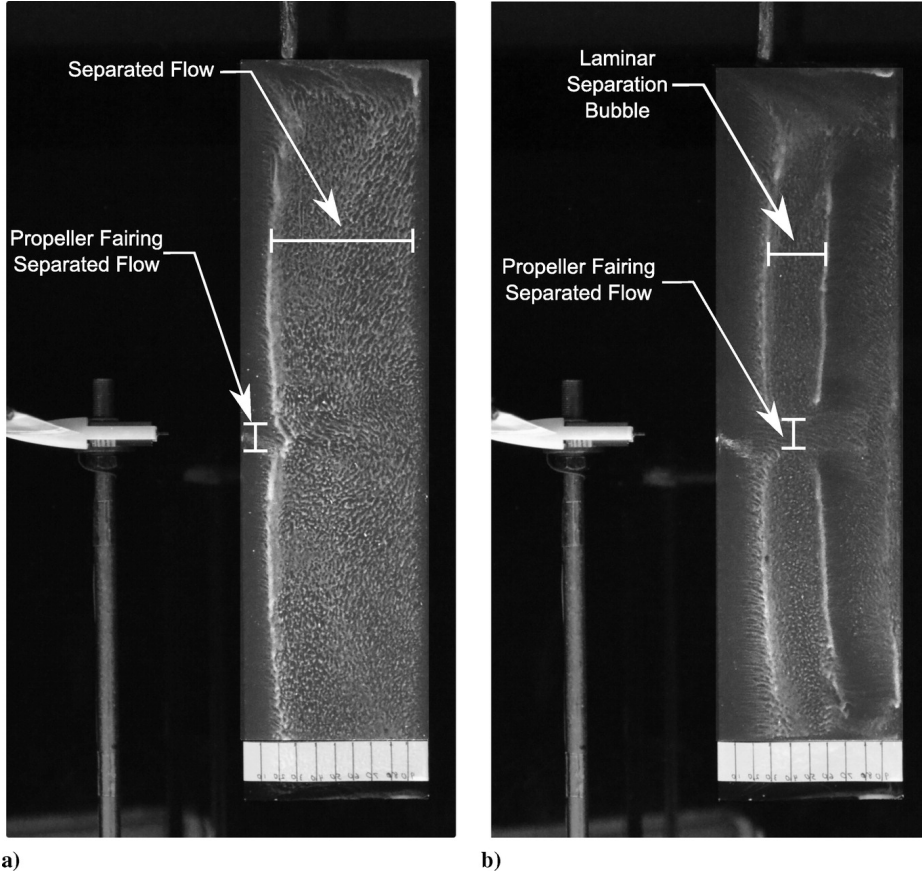


Fig. 3.2 Flow characteristics across the propeller when the propeller is turned off (a) and when the propeller is turned on (b) [65]

Low Reynolds number compressible aerodynamics are particularly important for small aircraft. Aircraft used to survey martian terrain and MAVs are mainly influenced due to the change in atmosphere and small geometry respectively [66]. Low Reynolds number effects are critical for propeller based MAV systems. As the root and tip of a propeller can differ significantly in Mach number [66]. As MAVs have small ARs due to their smaller size and non-conventional structures, low AR wings at low Reynolds numbers have recently, in particular, been studied [67] [68]. Cosyn showed that the

### 3.3 Low Reynolds Number Effects

flow over these is characterised by complex 3D phenomena such as wing-tip vortices, laminar to turbulent transitions, and flow separation, and re-attachment [69].

Airfoils in particular have been investigated due the importance of their use in aircraft. At low Reynolds numbers ( $10,000 < Re < 50,000$ ) the flow remains laminar when the airfoil is aligned with the incoming flow. Pressure gradients created due to a larger angle of attack or high camber (airfoil thickness) create turbulent flow following separation. This is also shown in Figure 3.3. Early research by Mueller showed that the maximum lift coefficient is typically 0.5 for airfoils before stalling at low Reynolds numbers [70].

At Reynolds numbers from 50,000 to 100,000 the separation bubble and turbulent layer thickness increase in size [57]. The separated shear layer will eventually gain enough momentum from the free-stream in order to reattached to the airfoil as shown in Figure 3.3. The separation bubble is also known as a laminar separation bubble (LSB). Mueller found that airfoil choice in this region was critical to the aerodynamic performance. Airfoils with large camber (thickness) produce large pressure gradients causing separating which leads to the formation of LSBs on the upper surface of the wing [70]. As Reynolds numbers increases the separation and attachment move towards the leading edge [57]. The turbulent layer thickness reduces and the airfoil performance improves. The turbulent layer thickness varies between airfoils and LSBs can still form up until around a Reynolds number of 200,000. This is notable as most MAVs operate around the 50,000 to 200,000 Reynolds number range [71]. At Reynolds numbers greater than 500,000 the separation point generally lies on the leading edge. The performance of airfoils increases due to the reduced turbulent layer [57].

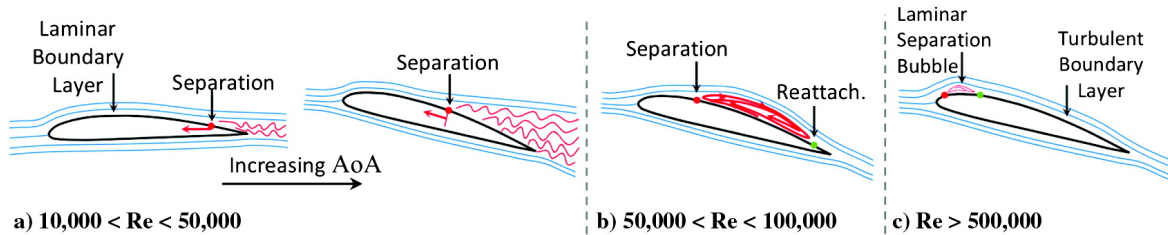


Fig. 3.3 Flow separation position change with Reynolds number [57]

## Literature Review

---

### 3.3.1 Laminar Separation Bubbles and Vortices

Flow separation and re-attachment create separation bubbles over wings and account for the most drag over the surface of wings at these low Reynolds numbers [72]. LSBs typically occur at Reynolds number below 200,000. Perot showed how in the presence of adverse pressure gradients, airflow separates from the wing [73]. This was further validated by Mohamed [74]. Mohamed investigated these LSBs and showed that they can deteriorate a MAVs stability as the drag induced by these bubbles leads to a low-pressure region over the bubbles, causing severe perturbations of motion [74]. Marxen found these bubbles are typically stable, as no transfer of energy occurs between the flow circulating inside the bubble and the laminar flow, which passes over the top [75]. Detailed anatomy of how LSBs affect flow over a typical airfoil shape is shown in Figure 3.4.

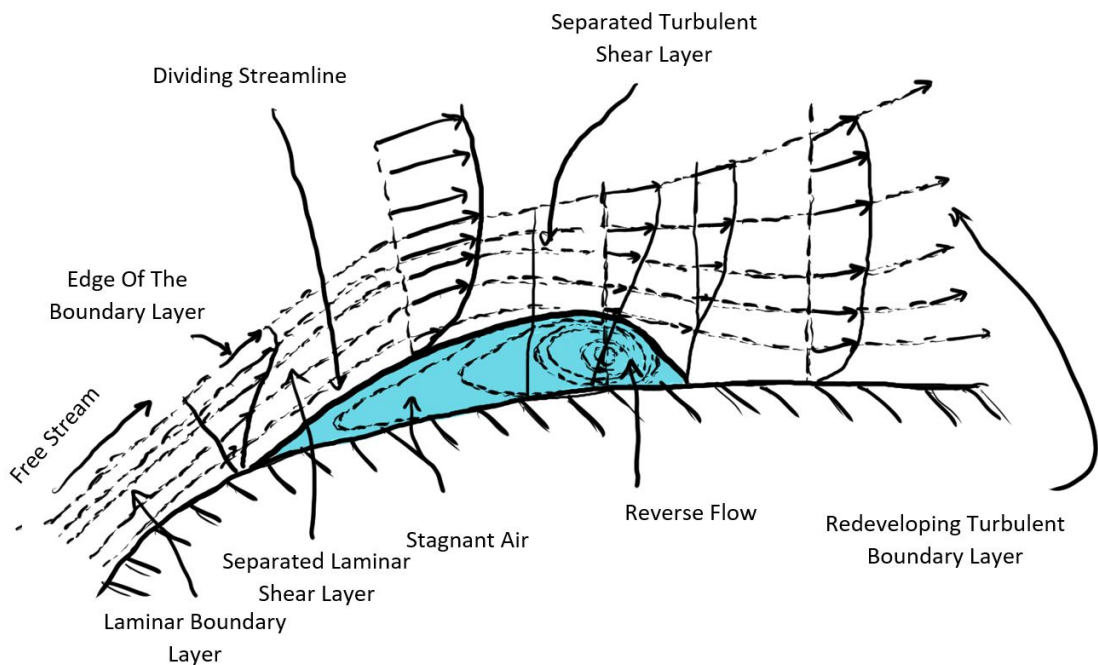


Fig. 3.4 Anatomy of laminar separation bubbles. Figure adapted from Mohamed [74]

### 3.3 Low Reynolds Number Effects

Crini then investigated the implications of this separation when varying the angle of attack. Crini determined that the angle of attack of an airfoil affects the placement of LSBs. When the angle of attack suddenly increases (e.g. during a gust), a separation of the shear layer is also seen close to the leading edge [76]. Mohamed explains this as the shear layer transitioning earlier due to this disturbance [74]. Additionally, LSBs and vortices also significantly affect the coefficient of lift ( $C_L$ ) of an airfoil.  $C_L$  is affected to a greater extent in smooth flow conditions as more suction is experienced inside an LSB with a smooth surface.

Mohammed found this larger suction seen on smooth surfaces, induces pitching and rolling moments [74]. In the stall region angle of attack, turbulent flow results in a higher lift. The opposite is true for smooth flow. Turbulence could therefore increase the characteristic airfoil performance at low Reynolds numbers [74]. These characteristics are also shown in Figure 3.5.

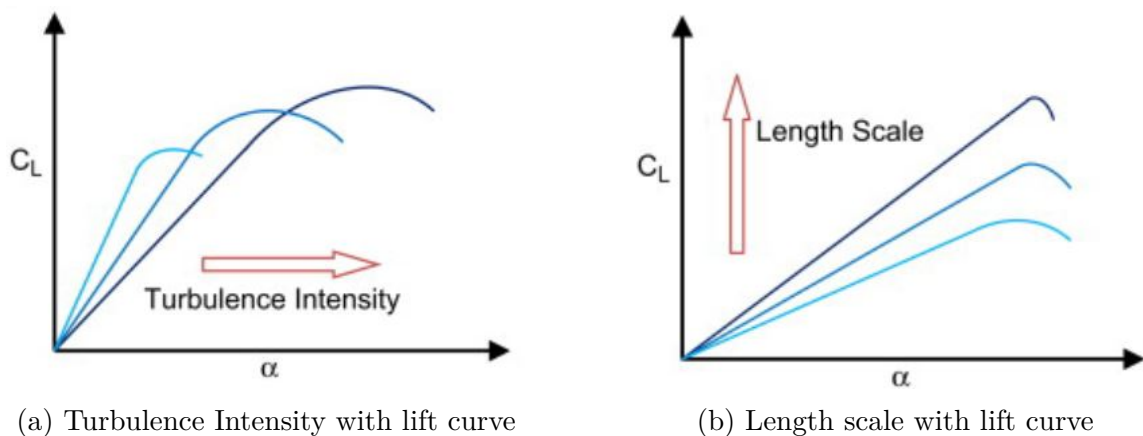
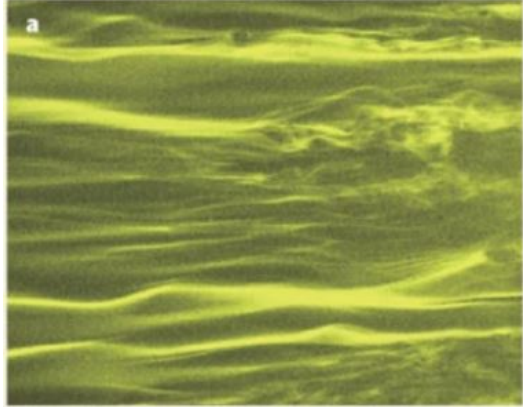


Fig. 3.5 Airfoil aerodynamic performance variation with increasing: (a) turbulence intensity (b) length scale [74]

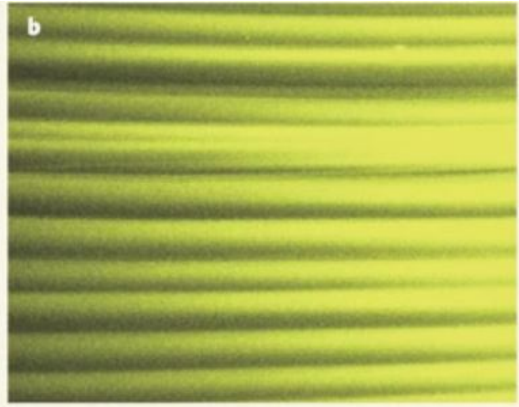
Investigations using materials with varying roughness have also been used to induce this transition to turbulent flow. Choi investigated this transition with some results shown in Figure 3.6. These show that the LSBs are reduced in the flow over airfoils when moving over a rough surface.

## Literature Review

---



(a) Smooth surface



(b) Rough surface

Fig. 3.6 Flow patterns shown by smoke. Laminar flow to turbulence without surface roughness (a). Laminar flow for with a rough surface (b). [77]

### 3.3.2 Non-Linear Lift Distribution

Early on in the study of aerodynamics, theories developed from the study of conventional aircraft were applied to the bodies of small flying objects and animals such as birds. Traditional aerodynamic theories provide good results and insights when steady flows move across a stationary body. As mentioned by Roccia, they could not however, explain what allows small insects and birds to fly, leading to the paradox of "a bee cannot fly" [78] [79]. Roccia determined that the issue lies in the fact that non-linear and steady flows mainly characterize the flight of biological creatures [79]. This non-linear lift distribution is primarily caused by the low Reynolds number that these small bodies fly at and the low AR that MAV aircraft typically have ( $AR < 3$ ).

Early experimental work conducted by Winter showed that wings with small ARs can be described with a bound vortex flow and a wing-tip flow, which is also known today as vortices [80]. Wingtip vortices are particularly important, and even in general aircraft, lead to regulations such as spacing rules between aircraft and aerodynamic noise [81]. At the wingtips the pressure difference between the upper and lower surface

### 3.3 Low Reynolds Number Effects

cause a swirling vortex when in a free stream flow. This phenomenon is also shown in Figure 3.7. Cosyn and Vierendeels showed that this creates a low pressure cell at the wing tip which deforms the lift distribution in this region [71].

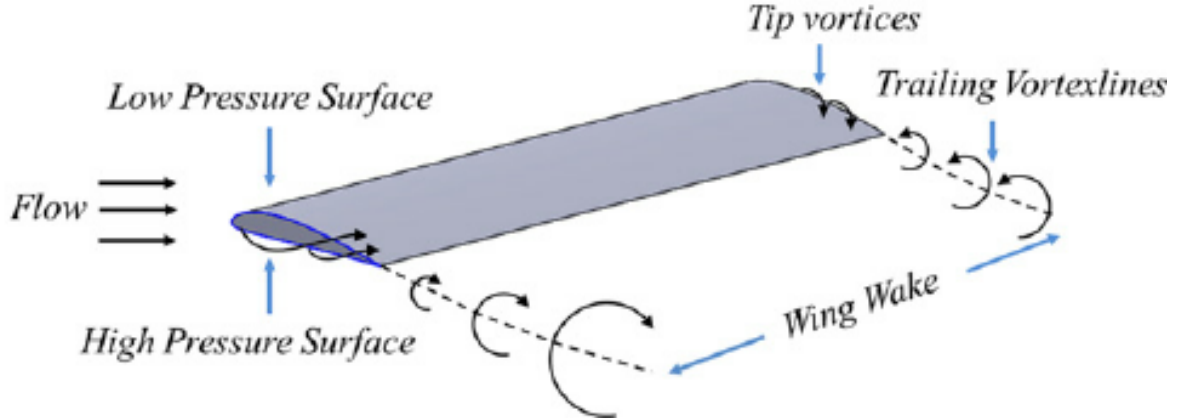


Fig. 3.7 Development of wingtip vortices over a wing section [82]

Zimmerman showed that the wing-tip geometry influences the aerodynamic performance for low AR wings [83]. Zimmerman also concluded that in order to produce the same coefficient of lift for lower AR wings, a higher angle of attack is required [83]. Low AR wings are also more susceptible to instability caused by disturbances [84]. Watkins showed that a sideslip is easily induced by a slight wind gust for low AR aircraft [85]. Shields investigated the inherent stability modes of low AR wings, determining that low AR wings have near-zero roll damping [86]. This means that roll moments created by flow asymmetries have a significant impact on low AR aircraft [86].

Mueller and DeLaurier found that for low AR aircraft, the center of lift was also sensitive to the angle of attack [87]. This is due to the wingtip vortices increasing with angle of attack. Therefore the non-linear aerodynamics dominate more at higher angle of attack, Pelletier also determined that these effects are more pronounced for low AR aircraft [88].

### 3.4 Propeller Wing Interaction

Propellers are commonly mounted on wings and significantly alter the flow seen over airfoils. Prandtl first studied the propeller-wing interaction at the start of the last century. The results concluded that two main effects impact the wing and flow behaviour. The first is due to the swirling of the propeller, which creates an ever-varying velocity. The second is due to an increase in inflow velocity [89]. Mounting propellers on the tips of the wing has also been shown to have benefits to performance compared with other wing positions [90]. Miranda found that substantial performance improvements can be achieved by properly mounting propellers on the wingtips of wings [90], this was also further validated by Sinnige [91] and other teams [92] [93].

Numerical analysis by Rizk using the Vortex Lattice Method (VLM) has also validated these observations [94]. Veldhuis found that propellers have a higher axial velocity at the blade tip than where it is joined at a hub [92]. Ferraro also determined that the slipstream created by the propeller can be split into the axial, and tangential velocity components [95]. The tangential velocity component accounts for the dynamic pressure across the wing [95]. The swirl is anti-symmetrical and changes the incoming flow that the wing sees. This is also shown in Figure 3.8(a) [95]. The axial velocity affects the dynamic pressure on the wing. The axial velocity is considered to be symmetric when the propeller flow is uniform and undisturbed, as shown in Figure 3.8(b) [95].

### 3.4 Propeller Wing Interaction

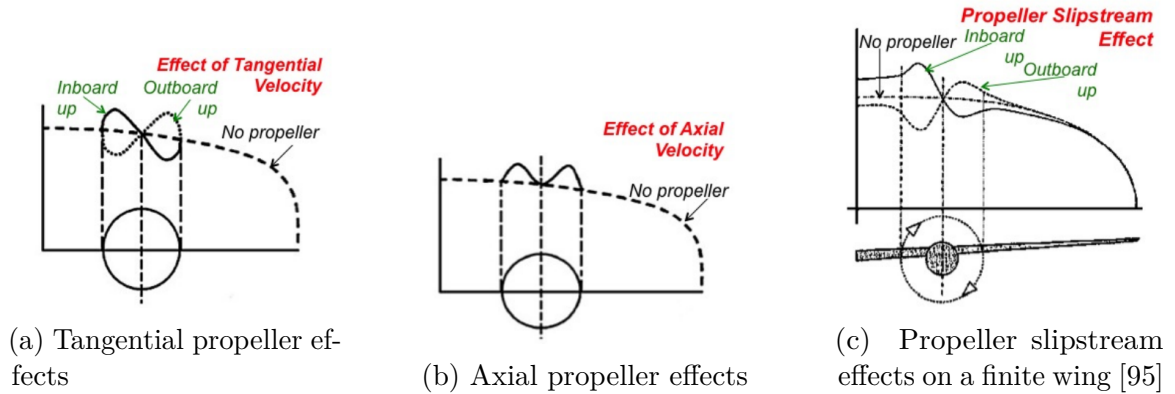


Fig. 3.8 Tangential and Axial velocity effects [95]

As the dynamic pressure increases, a gain in lift coefficient is seen as shown in Figure 3.9. This increase in lift coefficient is also partially due to the lack of separation seen when increasing the revolutions per minute (RPM) of the propeller. Shams shows that this leads to a forward shift in the aerodynamic center of the aircraft [54] [52].

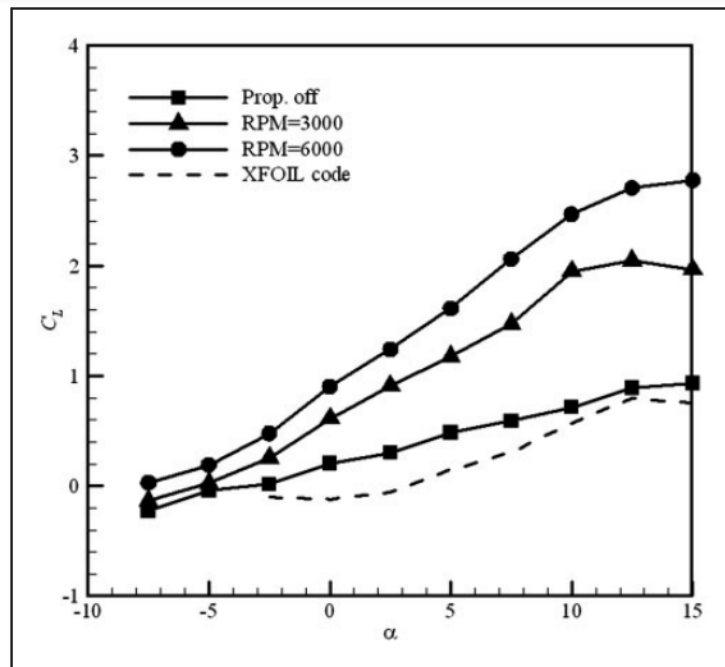


Fig. 3.9 Effect of propeller slipstream on the lift coefficient curve with angle of attack ( $Re = 0.3 \times 10^5$ ) [96].

## Literature Review

---

The slipstream effect is shown in Figure 3.10. The inboard wing sees a higher angle of attack, and hence an up-wash effect is seen ( $y/b > 0$ ). Aminaei found that in the propeller down-wash region ( $y/b < 0$ ) a delay is experienced in the flow transition than when compared with the up-wash region [96]. This is due to the reduced local angle of attack on the wing, which moves the transition region towards the trailing edge. These effects can also affect the flow stream beyond the propeller and lead to non-linear lift distributions further from the propeller as well.

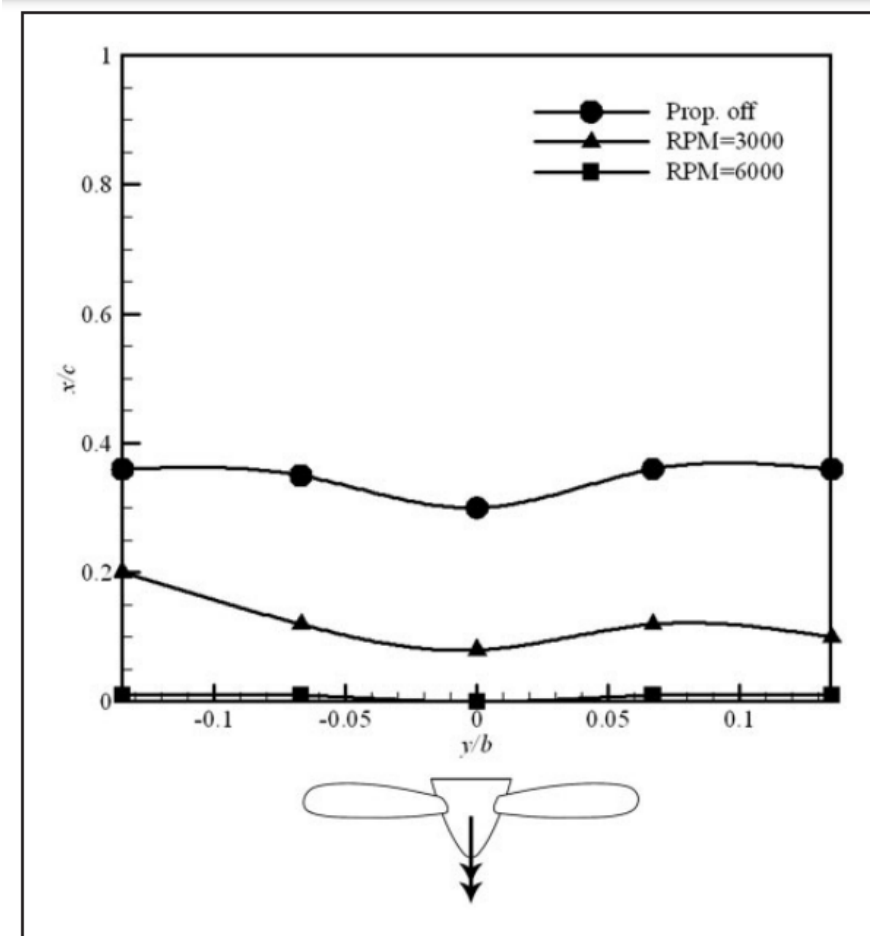


Fig. 3.10 Propeller slipstream effect with span-wise location for airflow transition over the wing upper surface,  $\alpha = 2.5^\circ$  [96].

Prantl was one of the first to investigate the influence of propellers on wings [97] and Franke and Weinig one of the first to investigate the rotational velocity's effects on

### 3.4 Propeller Wing Interaction

---

the lift distribution across the wing [98]. Framk and Weinig showed the circulation distribution in regards to the slipstream can be predicted using the lifting line theory [98]. Jameson went on to develop simple equations to quantify the lift and drag of wings in jet slipstreams [99]. Ellis developed programs to run multiple lifting line approximations to quantify the circulation pattern, when propeller effects are being accounted for [100]. These approximations were all too rudimentary and could not be used to predict the flow characteristics over wings. Veldhuis concluded that the propeller effects can only be described completely when using the Full Interaction Mode (FIM) [101].

Veldhuis determined that there are four regions of influence for a propeller. These sections are not independent of each other but rather act as a smooth transition from one to the other [101]. As shown in Figure 3.11 the local blade angle of attack increases where the blade moves down (P-II in Figure 3.11) and decreases where the blade moves up (P-IV in Figure 3.11). The induced angle of attack is visualised in Figure 3.12. The effect of the propeller to induce this change in effective angle of attack is most greatly seen when the propeller is parallel to the wing span [101].

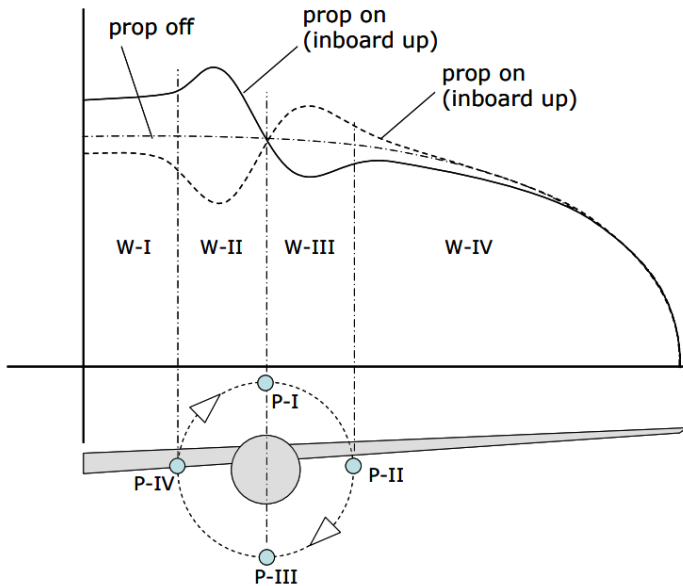


Fig. 3.11 Influence areas related to propeller-wing interaction based on the loading distributions [101]

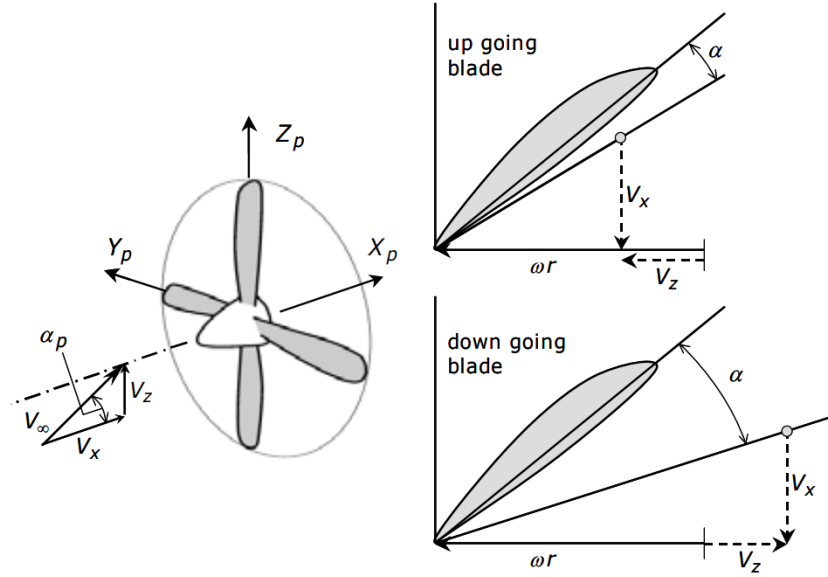


Fig. 3.12 Blade angle of attack variation due to propeller pitch angle [101]

Veldhuis also found that the extent of the swirl relaxation is dependent on the propellers position, free stream conditions and the overall wing loading [101]. A more recent study by Veldhuis simulated these effects through the use of CFD [102]. Ananda also concludes that for the tractor configuration, in a low speed wind tunnel, the flow transitions to turbulent flow earlier. This reduces the drag and increases the lift to drag ratio. These benefits were not seen when analysing the pusher configuration.

### 3.4.1 Stability Effects

As propellers have been shown to have a strong influence on the lift distribution across wings, the overall lateral and longitudinal stability will be affected. Shams has showed that increasing the propeller diameter and RPM increase the moment produced creating a larger pitching moment on the aircraft [54]. Tractor configurations have also been investigated by Shams. The tractor configuration creates an increase in the rolling and

yaw moments acting on the aircraft [54]. Propellers do also produce a torque effect, further destabilizing the aircraft by creating an asymmetric roll.

#### 3.4.2 Aerodynamic Parameters

The characteristics of an aircraft are given by a combination of the aerodynamic parameters that describe it. For MAV, this is more complex as these aircraft do not allow for the same assumptions to be made in calculations. New methods such as those developed by Shen, for determining the aerodynamic parameters are currently being developed, and proposed in order to address these differences [103, 104]. Aerodynamic forces are crucial to the overall design of any aircraft [105]. In order to determine these forces for MAVs, a variety of techniques have been used, such as the Athena Vortex Lattice (AVL) Method used by Stewart and Hrad [106, 107]. However, this method cannot predict the separation of flow as the lift is assumed to increase linearly with the angle of attack. This is not the case at low Reynolds numbers [108]. Aboelezz outlines a process in which a fixed-wing MAV can be designed, whereby he uses physical wind tunnel testing in order to evaluate the MAVs actual flight performance [25]. Bollay and Belotserkovskii have both proposed modified versions of Prandtl's lifting line theory [109, 110], though validations with experimental data are limited in scope and do not validate propeller-wing interactions.

#### 3.4.3 The General Micro Aerial Vehicle

Today the interest, research and development of MAVs are continually increasing. However, in order to focus on particular aspects or compare various designs, a "baseline" geometry is required. An example of this is the GenMAV developed by Stewart [106] shown in Figure 3.13.



Fig. 3.13 GenMAV Model [106]

While there are various models which have been tested to determine the main aerodynamic properties [106] [25], none have completed a physical wind tunnel test while accounting for the effects of a powered propeller. Initial GenMAV aerodynamic data was determined by using the vortex-panel method by Stewart [106], and did not involve wind tunnel testing. The effects of propeller induced flow have also been studied for both fixed and free-spinning propellers, but currently, no data is available for wind tunnel tests of a powered propeller MAV.

### 3.4.4 Optimization Techniques and Validation

Many non-standard aircraft designs are evaluated using software to analyse aerodynamic characteristics and then optimised through a variety of typical software engineering methods such as the particle swarm method used by Gomez to optimize the algorithm for the attitude and altitude, and Boutemedjet who used this to optimize the wing planform parameters of a MAV [111, 112]. These procedures are used, as non-standard aircraft designs are more tedious to design and even more complex to set up and test

### 3.4 Propeller Wing Interaction

than standard aircraft designs. The unique constraints that MAVs have and how they led to poor attitude control are shown in Figure 3.14.

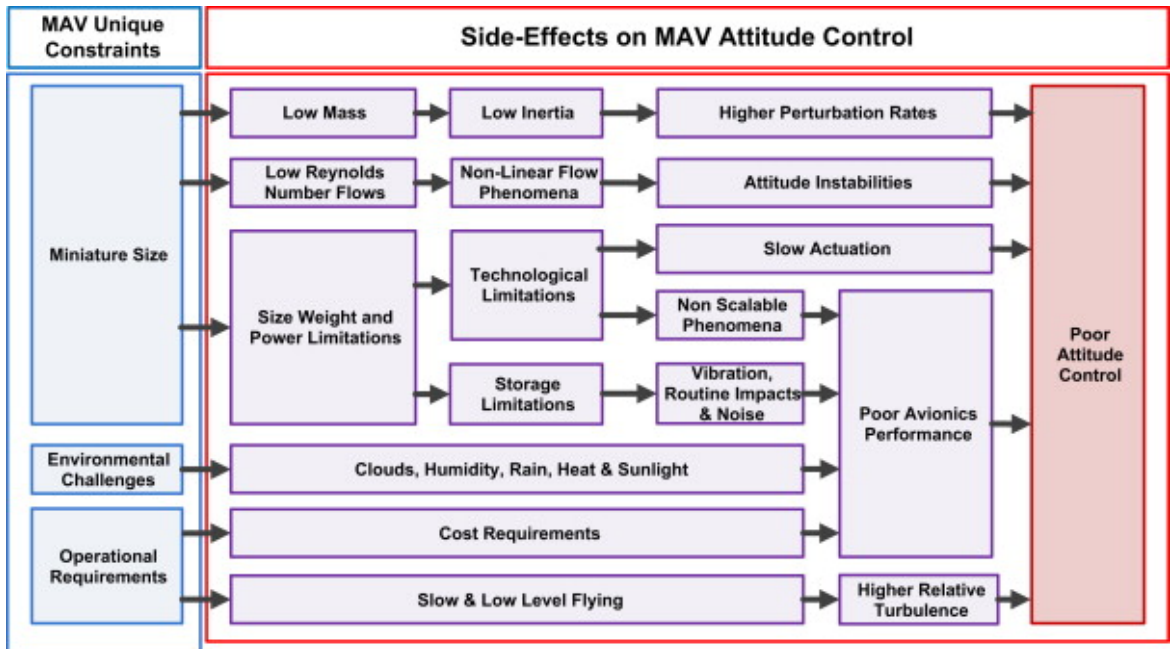


Fig. 3.14 Unique constraints of MAVs [74]

Mohamed found that the physical size, environment and flight regime have strong effects on a MAVs ability to fly and carry payloads [74]. Many groups of researchers have created software to optimize MAVs by using optimization algorithms such as genetic algorithms, non-dominating sorting generic algorithms, particle swarm optimization and sequential quadratic optimization programs. While some have accounted for low speed flight [23, 47, 48], no optimization techniques accounting for propeller-interaction effects currently exist. Many investigations into propeller effects show the propeller has significant effects on wing aerodynamics, both in regards to performance and also stability [113, 114]. None have been used with the results of spinning propellers in physical wind tunnel testing. Therefore these software models are currently invalid when also accounting for propeller-wing effects.

# Chapter 4

## Theory and Methodology

This chapter outlines the theory and methodology used to create, test and collect the data required for the wing-propeller interaction analysis. It covers the development of the MAV model for testing from python scripts and FreeCAD to the final testing completed in a 3x4ft wind tunnel to collect the force and moment data of the model. The software used to validate these results is also explained in this chapter.

### 4.1 Material Choice

To readily edit and modify the model to be tested, 3D printing was used to print the final developed model. 3D printing has become increasingly common when developing models testing in wind tunnels [115]. Polylactic acid (PLA) filament was used to print the main body of the model as this is the most widely used and available filament for 3D printing purposes. PLA has a low melting point of  $\approx 150$  °, good layer adhesion and structural strength. PLA can also be extruded in various ways to develop different textures on the surface of the 3D model [116]. This is particularly significant for MAVs as aircraft surfaces are typically smooth to reduce viscous drag effects. 3D printed models may have thin ridges between layers when printed. However, the extrusion rate, nozzle size, temperature, and bed temperature can all be set to mitigate this issue as much as possible [116] [117]. However, a lightweight PLA was used for the wings and tail to print a smoother surface. This is particularly important for the wings and tail

as these are the main surfaces that provide lift for the aircraft. Using a lightweight PLA, the structure allows for some bending, as seen in typical wing shapes, rather than printing with standard PLA to produce a rigid structure.

## 4.2 FreeCAD

FreeCAD is a 3D parametric modeller and was used with python scripts provided by Dries Verstraete to produce fuselage, wing and tail shapes when given input parameters to define the shape and geometry. Various model shapes were produced to make the model 3D printable and allow for easy manufacturing and testing. Several design constraints had to be considered due to the structural strength of the PLA used for 3D printing and size limitations. The wings and tail in particular had to be large enough to print the aerofoil shape accurately. The TL54 airfoil was used for the main wings due to this airfoil having a high lift coefficient and low pitching moment. The model's dimensions are also given in Figure 4.2. The model shown in Figure 4.1 was also fitted to mount into the 3x4ft wind tunnel for testing as shown in Figure 4.3.



Fig. 4.1 Final model for wind tunnel testing in FreeCAD

The model size was chosen to reduce the blockage experienced when using the model during wind tunnel testing. The blockage varied from 4.9% to 8.7% for an angle of

## Theory and Methodology

---

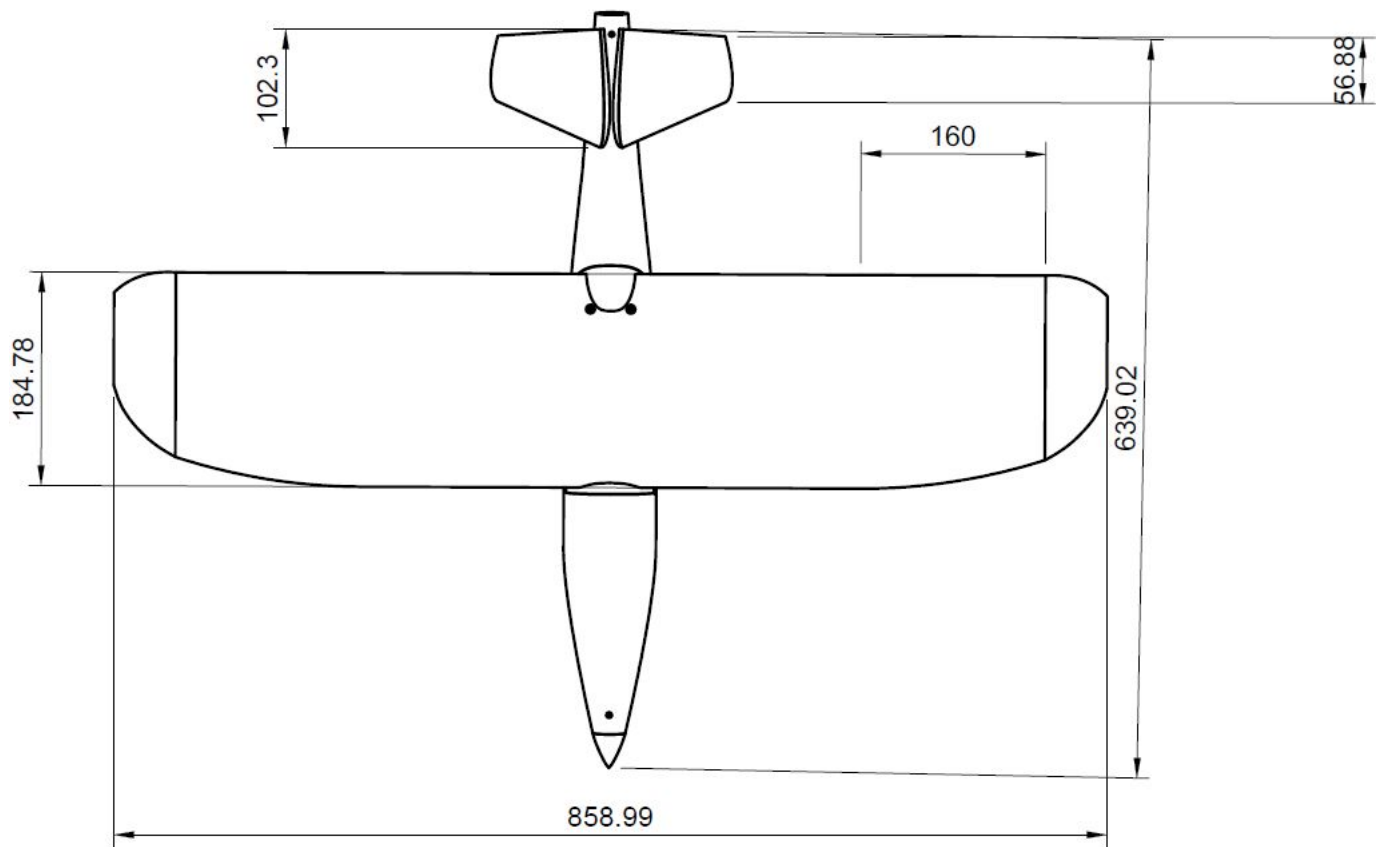


Fig. 4.2 Dimensions of the final MAV model in millimeters

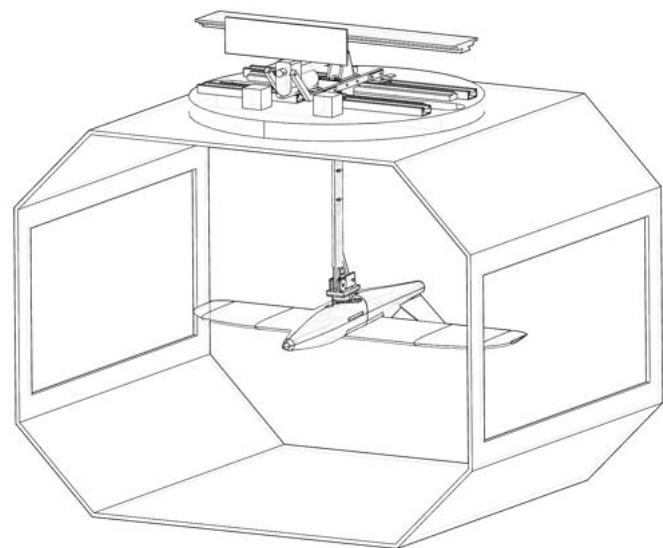


Fig. 4.3 FreeCAD model mounted in Wing tunnel

attack range from  $-5^\circ$  to  $15^\circ$ . The wing span was also limited in size to ensure that wind tunnel interference would not influence the results.

## 4.3 VAP 3.5

VAP 3.5 is open-source software that uses the High-Order Free Wake (HOFW) method to determine the aerodynamic performance of MAV designs.

The software is used by first defining the flight conditions and geometry of the model to be tested. This includes setting the duration of the simulation to ensure that the wake from the propeller and wing have interacted and fully developed. The VAP 3.5 model is then generated and run through the potential flow method used by the VAP 3.5 software. This is used to determine the aerodynamics of the MAV design to be tested. The weight and CG location of the model as determined based on the MAV geometry or explicitly defined in the code used to generate the model. The stability derivatives can be determined based on the CG location and the lift distribution determined in the VAP 3.5 potential flow method. A flowchart is given in Figure 4.4 to outline this process.

The HOFW method uses higher-order vorticity elements to represent the wings and propeller blades as lifting surfaces. This method has a faster computational speed, numerical stability and realistic prediction than alternatives such as the Navier-Stokes equations, fixed wake panel method, relaxed wake method or the Vortex Lattice Method (VLM). It was initially developed to create a potential flow method that allowed for improved force resolution and intrinsic computational stability while keeping a simple geometric representation [118]. This method has also been shown to be suitable for lightly loaded propeller/proprotors and propeller-wing systems. The HOFW method is a higher-order, relaxed-wake potential flow method which imposes Neumann boundary

## Theory and Methodology

---

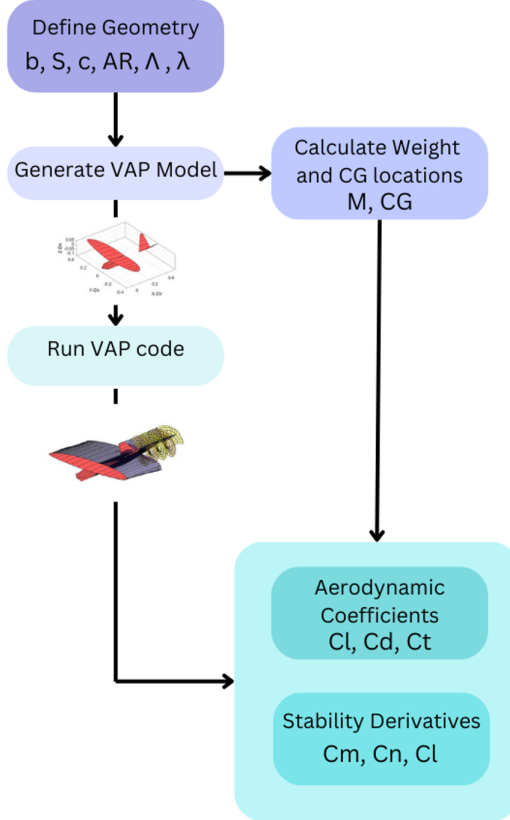


Fig. 4.4 VAP 3.5 main steps to setup, run and return results from simulation

conditions. It consists of a non-linear vorticity distribution along the transverse and linear distribution along the streamwise edges of a single Distributed Vortex Element (DVE). A single element is shown in figure 4.5.

For propeller-wing systems, the circulation distribution over each surface distributed vorticity element (SDVE) is calculated using Equation 4.1. Where  $[A]$  is the influence matrix which is a function of the geometry representing the lifting surfaces,  $\{x\}$  is a vector of the unknown DVE strengths, and  $\{B\}$  is the resultant vector where the boundary conditions are applied.  $A$ ,  $B$ , and  $C$  hence represent the coefficients of the circulation distribution.

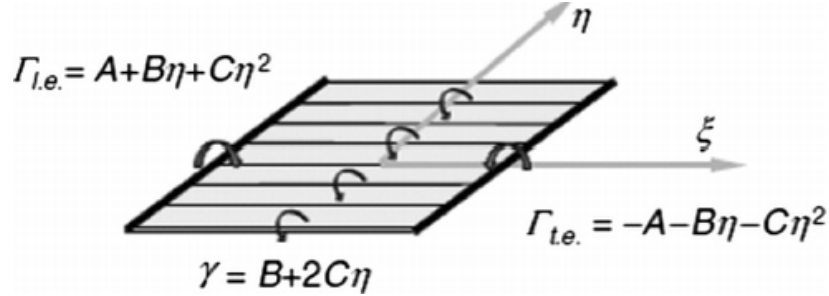


Fig. 4.5 Visualisation of a single distributed vorticity element. The leading and trailing edge vortices are represented by  $\Gamma_{l.e.}$  and  $\Gamma_{t.e.}$ , respectively. The quadratic circular distribution is in the spanwise  $\eta$  direction, and the leading and trailing edge vortices are joined in the streamwise direction by a linear changing distribution vorticity strength indicated by  $\gamma$  in the spanwise direction [118].

$$[A]\{x\} = \{B\} \quad (4.1)$$

The transverse vorticity axis ( $\eta$ ) uses a quadratic function to model the vorticity distribution, whereas the streamwise axis ( $\zeta$ ) uses a linear process. The simplicity allows for ease of calculation compared to alternative methods. The total force due to the lift of each SDVE is the summation of the kinematic velocity and the force calculated with the induced velocity as given by Equation 4.2 [118].

$$\bar{F}_{total} = \bar{F}_k + \bar{F}_{ind} \quad (4.2)$$

The kinematic lift force and induced velocity force are determined at each time step to determine the lift and drag as they are defined relative to the freestream velocity. The kinematic lift force is calculated using Equation 4.3

$$\bar{F}_k = \rho \sum_{i=1}^m \sum_{j=1}^n \left[ \int_{-\eta_{i,j}}^{\eta_{i,j}} |\bar{V}_k \times \hat{s}_{i,j}| (\Gamma_{i,j} - \Gamma_{i-1,j}) d\eta \frac{\bar{V}_k \times \hat{s}_{i,j}}{|\bar{V}_k \times \hat{s}_{i,j}|} \right] \quad (4.3)$$

## Theory and Methodology

---

Where n is the number of spanwise panels, m is the number of lifting lines,  $\eta$  is the half span and  $\hat{s}$  is the unit vector along the leading-edge bound vortex of the distributed vorticity element. The induced velocity forces are calculated using Equation 4.4.

$$\bar{F}_{ind} = \rho \sum_{i=1}^m \sum_{j=1}^n \left[ \int_{-\eta_{i,j}}^{\eta_{i,j}} |\bar{V}_{ind} \times \hat{s}_{i,j}| (\Gamma_{i,j} - \Gamma_{i-1,j}) d\eta \left( \frac{\bar{V}_{ind} \times \hat{s}_{i,j}}{|\bar{V}_{ind} \times \hat{s}_{i,j}|} \right) \cdot \left( \frac{\bar{V}_k \times \hat{s}_{i,j}}{|\bar{V}_k \times \hat{s}_{i,j}|} \right) \right] \quad (4.4)$$

## 4.4 XFOIL

XFOIL, developed by Harold Youngren and Mark Drela was used to analyse 2D airfoils for their aerodynamic characteristics. XFOIL was used to produce aerofoil data which accounted for viscous effects. Viscous effects have an essential role in the flow characteristics across the surface of an aircraft wing. This is particularly important at lower Reynolds numbers. Xfoil uses the wake momentum thickness to determine the skin friction produced as the fluid passes over the airfoil surface as given by Equation 4.5. In this manner the skin friction losses can be determined and accounted for when running the VAP 3.5 software to analyse the stability of the model.

$$\theta = \int_0^\infty \frac{u}{U_e} \left(1 - \frac{u}{U_e}\right) dy \quad (4.5)$$

Where:

- $\theta$  is the momentum thickness at a given point along the airfoil
- $U_e$  is the freestream velocity
- $u$  is the flow velocity at a position  $y$  distance from the airfoil surface

### 4.5 Wind Tunnel Testing

To analyse the stability of the final developed model, the model was mounted in the 3x4 ft wind tunnel to determine the forces and moments acting at several conditions to assess the effect that adding a propeller has on the stability of the model. Wind tunnel tests were taken for variations of AoA, airspeed, propeller speed and configuration. These are outlined below

- AoA: -5 ° to 15 ° in increments of 2°
- Airspeed: 10m/s, 15m/s and 20m/s
- Motor speed: 6000RPM, 9000RPM, 11000RPM
- Configuration: No propeller, tractor and pusher

A safety net was placed in the wind tunnel in case parts of the model could not remain attached as the airspeed increased to 20m/s, as shown in Figure 4.6(a). An external cooler was used to ensure that the wind tunnel motor did not overheat and is shown in Figure 4.6(b).



(a) Safety net to prevent any model parts from damaging the wind tunnel if the mount were to disconnect



(b) Cooler for wind tunnel motor

Fig. 4.6 Safety measures taken to ensure no damage is done to any people or to the wind tunnel itself.

## Theory and Methodology

---

The nano25 load cell was used to record the forces and moments acting on the model about the mounting position at  $25\bar{c}$  and is shown in Figure 4.7(a). The model mount was then attached over the load cell as shown in Figure 4.7(b)



(a) Nano 25 load cell mount



(b) Model mount in 3x4 wind tunnel

Fig. 4.7 Wind tunnel mount and load cell used

The model was then attached in three main configurations. These were mounting the propeller without a propeller, in a pusher and tractor configurations. These configurations are shown from Figure Figure 4.8(a) to Figure Figure 4.8(c) respectively.



(a) Model with no propeller attached



(b) Model in pusher configuration



(c) Model in tractor configuration

Fig. 4.8 Examples of MAVs with category

## 4.6 Stability Calculation

---

The wind tunnel was then calibrated for wind speed, atmospheric conditions and angles of attack. The mount used for the model was double-checked using a pitch gauge to ensure the angle of attack was correct as shown in Figure 4.9.



Fig. 4.9 Calibrating pitch of model mount to ensure AoA is accurate

When using the prop, the motor was supplied with a 7.4V battery, and the RPM was set to  $\approx 6000RPM$ ,  $\approx 9000RPM$  and  $\approx 11000RPM$ . The bias at each airspeed tested was first calculated to determine the change in forces and moments across the angles of attack tested. Following this, an AoA sweep from  $-5^\circ$  to  $15^\circ$  was undertaken for each airspeed analysed. For each velocity, the bias was recalculated. From the force and moment data collected, the main stability coefficients for the MAV model could be determined.

## 4.6 Stability Calculation

To determine the stability in all the tested configurations, the stability derivatives of the model had to be determined. Data from the nano25 load cell was used to determine the loads and moments acting on the model about the mounting point. These values were transferred to the neutral point of the model at  $20\bar{c}$ . The aerodynamic coefficients were determined using equations 2.4 to 2.5, and the moment coefficients about the pitch, yaw and roll axis were calculated using Equations 2.9 to 2.13.

# Chapter 5

## Results and Discussion

### 5.1 Wind Tunnel Results

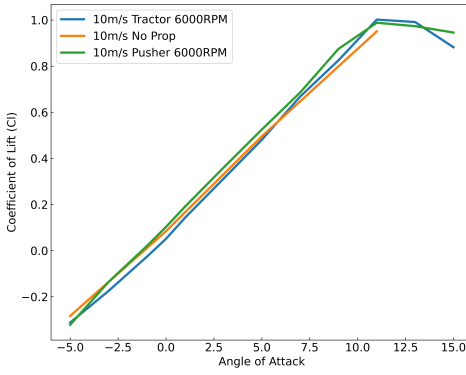
This chapter outlines the final wind tunnel results for all three main configurations; tractor, pusher and no propeller. It outlines the main trends in the stability coefficients  $C_l$ ,  $C_n$ , and  $C_m$  corresponding to the MAV model's roll, yaw and pitch. These results are analysed with critical observations and trends identified. A validation of the wind tunnel results is also conducted with VAP 3.5 to compare the accuracy of the results obtained with any discrepancies explained.

#### 5.1.1 Aerodynamic Coefficient of Lift

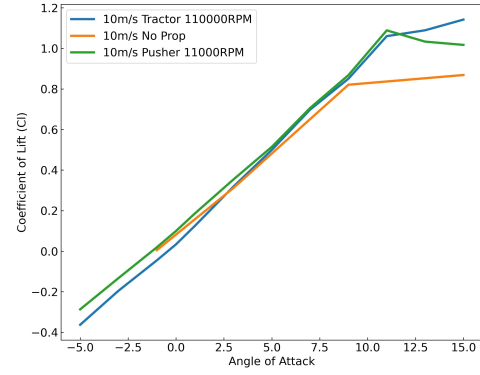
Figure 5.1(a) and 5.1(b) show that as the motor speed increases from 6000RPM to 11000RPM the coefficient of lift increases slightly for both the tractor and pusher configurations. The tractor configuration sees an increase in the lift coefficient beyond the stall point, while the pusher configuration has a linear decrease in the lift coefficient beyond the stall point. Increasing the airspeed to  $20\text{ms}^{-1}$  at the higher 11000RPM speed delays the MAV model's stall as the angle of attack increases in all configurations. Increasing the airspeed when the motor is at 6000RPM increases the max coefficient of lift seen for the pusher configuration and delays stall. Null also found that propellers

## 5.1 Wind Tunnel Results

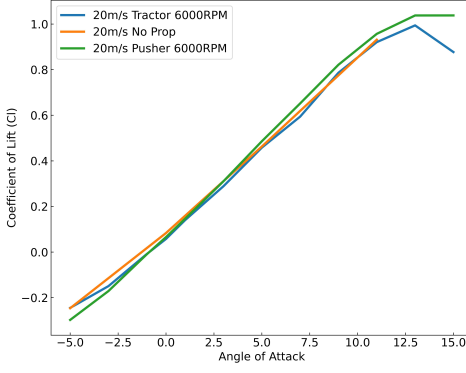
on wings during low Reynolds flight increased the performance of the wing at high angles of attack [64] with a delayed stall also observed. The tractor configuration has a deeper stall when airspeed is at  $20\text{ms}^{-1}$ , and leads to a more unrecoverable aircraft if stall were to occur as due to a more pronounced loss of lift. It also gives little room for error or warning to correct the MAVs position to avoid a stall. These trends due to airspeed are shown between Figure 5.1(a) and 5.1(c) as well as between Figure 5.1(b) and 5.1(d).



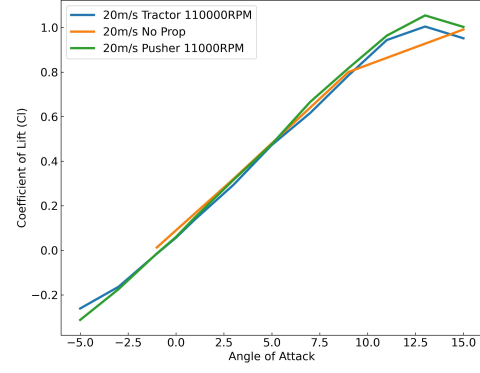
(a) Coefficient of lift at 10m/s airspeed and 6000RPM motor speed



(b) Coefficient of lift at 10m/s airspeed and 11000RPM motor speed



(c) Coefficient of lift at 20m/s airspeed and 6000RPM motor speed



(d) Coefficient of lift at 20m/s airspeed and 11000RPM motor speed

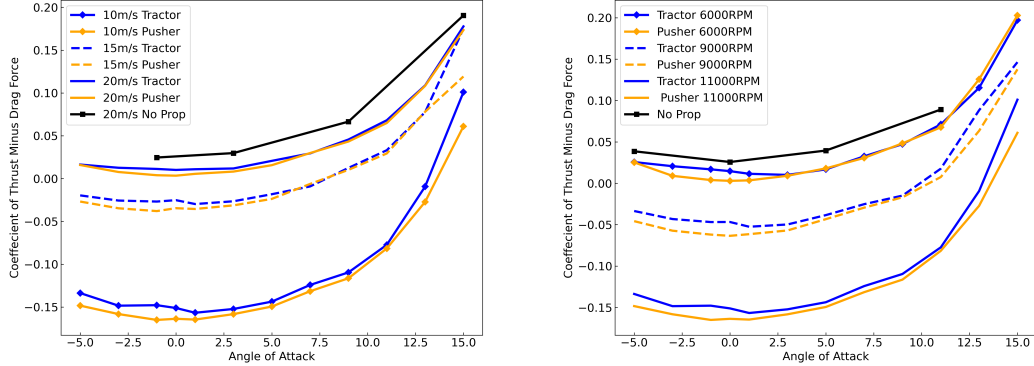
Fig. 5.1 Coefficient of lift variation with various conditions for the pusher, tractor and no propeller configurations

## Results and Discussion

---

### 5.1.2 Aerodynamic Coefficient of Thrust Minus Drag Force

Figure 5.2(a) shows that as the wind tunnel airspeed increased, the thrust minus drag coefficient (referred to as the force coefficient) shifted upwards for both the pusher and tractor configuration. The overall force for both the tractor and puller configuration at  $10\text{ms}^{-1}$  airspeed is negative and shifts to positive value as the airspeed increases to  $20\text{ms}^{-1}$ . The thrust produced by the propeller decreased as the airspeed increased for both the tractor and puller configurations. The force curve shifts into negative values for the tractor and puller configurations as the thrust produced by the propeller is sufficient to balance the drag. As the overall force is a measure of the thrust minus drag, the overall force becomes negative, shifting the coefficient of force curve into negative values. As the airspeed increases, the force coefficient is also seen to increase for the pusher and tractor configuration with increasing airspeed. This shifts the coefficient of force curves upwards as the airspeed increases. The highest force coefficient occurred when no propeller operated on the MAV model. Ananda concluded that for tractor configuration propeller-wing set up in a low-speed wind tunnel, the flow transitions to turbulent flow earlier. This reduces the drag and increases the lift-to-drag ratio [65]. This shows a discrepancy with the results seen in this study. However, Ananda's setup involved a motor being mounted in front of the wing with no direct attachment; hence, the forces are not directly applied to the wing [65]. When no propeller is added, no significant changes are seen in airspeed for the force coefficient. The tractor configuration, in general, has a lower overall thrust minus drag than the pusher configuration; hence, the force coefficient is lower for the tractor configuration. This is most clearly seen at  $20\text{ms}^{-1}$  in Figure 5.2(a). This could possibly be due to less thrust being produced in the tractor configuration, however further investigation is needed as the motor thrust was not separately measured during wind tunnel testing.



(a) Coefficient of drag variation at 10ms  
11000RPM motor speed for the tractor, airspeed for the tractor, pusher and no pro-  
pusher and no propeller configurations (b) Coefficient of drag variation at 10ms  
propeller configuration

Figure 5.2(b) shows that the coefficient of force shifts downwards as the propeller RPM increases from 6000RPM to 11000RPM at an airspeed of  $10\text{ms}^{-1}$ . This trend changes as the airspeed increases due to the propellers beginning to windmill as the airspeed increases to  $20\text{ms}^{-1}$  (the tractor and pusher configuration at 6000RPM propeller as shown in Appendix A). The propeller adds additional drag to the MAV model causing the coefficient of force to shift downwards. The tractor configuration again has a lower overall thrust minus drag than the pusher configuration, conclusive reasons for this cannot be made as the motor thrust was not separately recorded. However likely that propeller is tractor configuration produces less thrust due to blockage from the fuselage.

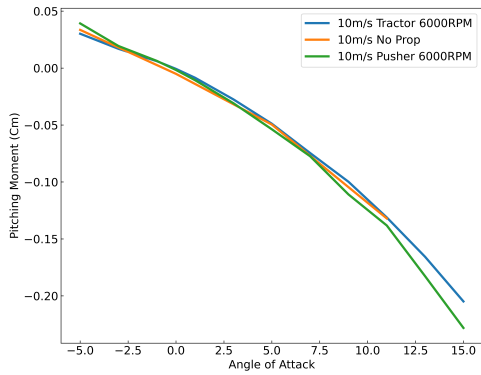
### 5.1.3 Pitching Moment Coefficient

Figures 5.3(a) to 5.3(d) show that for all cases, the pitching moment of the MAV model decreases as the angle of attack increases. This leads to a stable MAV in all cases as the longitudinal stability is maintained due to the pitching down motion of the MAV as the AoA increases. Figures 5.3(a) to 5.3(d) also show that as the motor speed increases from 6000RPM to 11000RPM, the tractor configuration experienced a

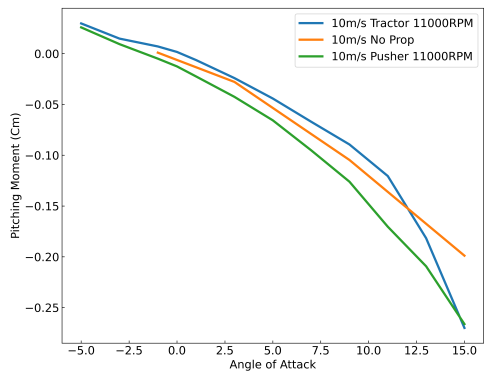
## Results and Discussion

---

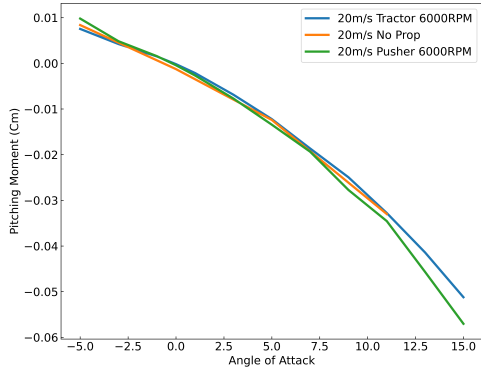
decrease in pitching coefficient compared with the no propeller model up until stall at approximately  $12^\circ$  AoA. The pusher configuration experienced an increase in the pitching moment compared with the no-propeller model. This shows that as the airspeed and propeller speed increase, the tractor configuration becomes less stable, while the pusher configuration becomes more stable. Increasing the airspeed decreased the pitching moment for all motor speeds.



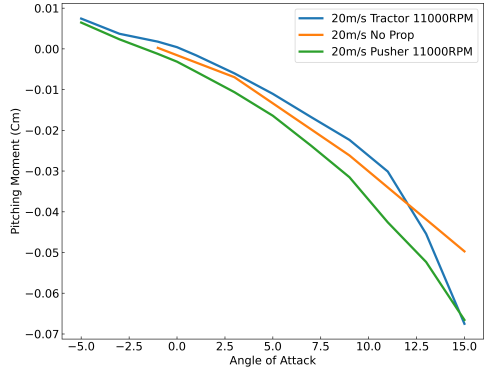
(a) Pitching Moment Coefficient at 10m/s airspeed and 6000RPM motor speed



(b) Pitching Moment Coefficient at 10m/s airspeed and 11000RPM motor speed



(c) Pitching Moment Coefficient at 20m/s airspeed and 6000RPM motor speed



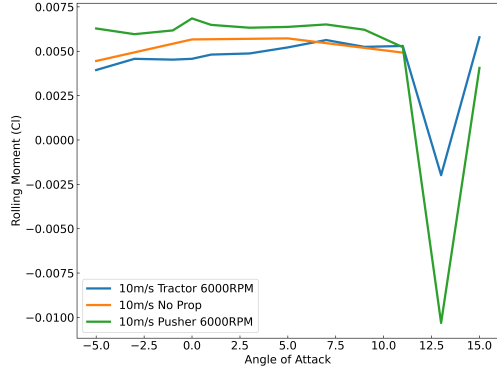
(d) Pitching Moment Coefficient at 20m/s airspeed and 11000RPM motor speed

### 5.1.4 Rolling Moment Coefficient

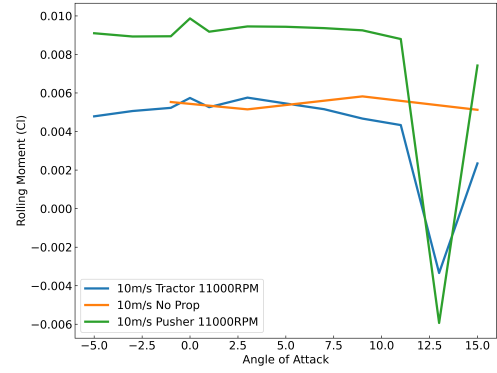
Figures 5.4(a) to 5.4(d) show that the tractor configuration rolling moment coefficient at 6000RPM propeller speed was shifted downwards compared to both the pusher and no propeller configurations, leading to a decrease in the rolling moment for all airspeeds. At 11000RPM propeller speed, the tractor configuration showed a sharp drop, seen at  $\approx 12.5^\circ$  AoA. In comparison the pusher configuration shows a shift upwards and an increase in the rolling coefficient for all airspeeds and propeller speeds. The rolling moment is due to the propeller torque effect due to the propeller wing interaction, previously described in Section 3.4. The tractor configuration experiences a flow distribution change over the wings and fuselage due to the propeller's upwash and downwash effect, as described in Section 3.4. This affects the lift distribution across the wings' surface, shifting the roll moment coefficient upwards as one wing is in the upwash of the propeller blades and the other in the downwash airstream. As the AoA increases, the rolling moment increases until sharply dropping off as the right wing of the MAV stalled first, creating a lift force imbalance as the left wing continued to produce lift. At the same time, the right-wing experiences flow separation due to stalling. The rolling moment sharply raises as the left wing also stalls and the flow over the left wing separates. The pusher configuration shifts the rolling moment to a larger extent due to having a larger moment arm from the position of the propeller to the aerodynamic centre of the MAV model than the tractor configuration. The pusher configuration also shows an increase in the roll moment coefficient at  $0^\circ$  AoA for all airspeeds, while the tractor configuration shows this only when the propeller is running at 11000RPM. The rolling moment also decreases after  $2.5^\circ$  AoA for the tractor configuration when the propeller runs at 11000RPM. The increases in roll moment at  $0^\circ$  AoA is likely due to an interaction with the wing and/or the wings wake. However, more investigation is needed to validate this.

## Results and Discussion

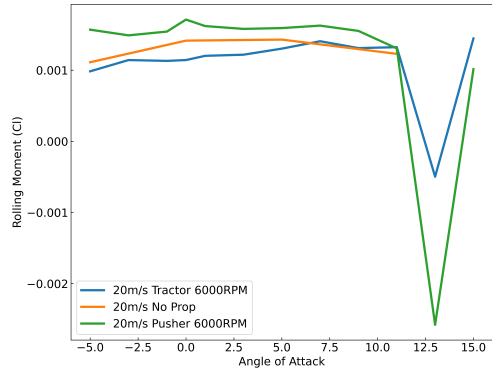
---



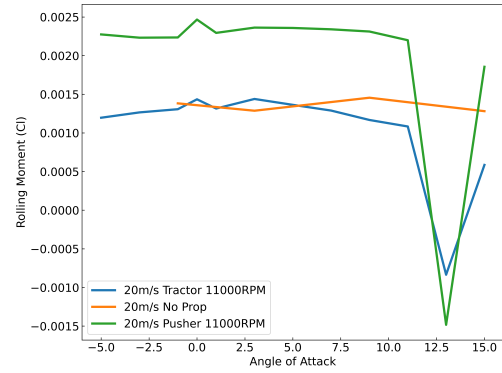
(a) Rolling Moment Coefficient at 10m/s airspeed and 6000RPM motor speed



(b) Rolling Moment Coefficient at 10m/s airspeed and 11000RPM motor speed



(c) Rolling Moment Coefficient at 20m/s airspeed and 6000RPM motor speed



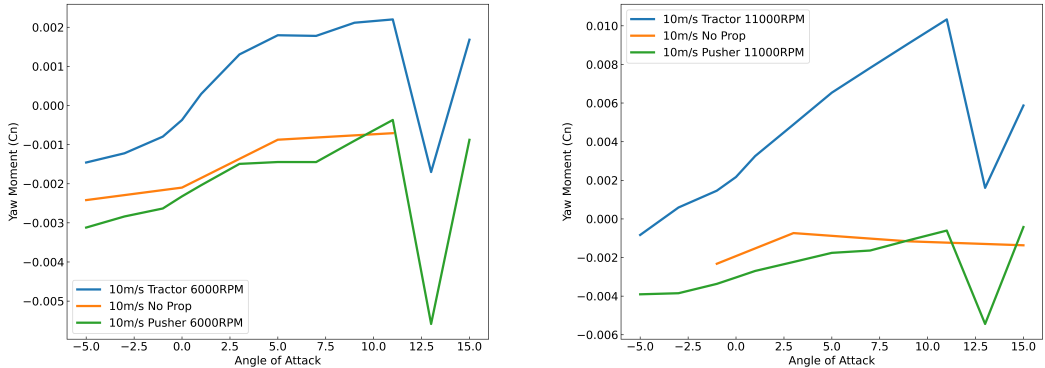
(d) Rolling Moment Coefficient at 20m/s airspeed and 11000RPM motor speed

### 5.1.5 Yawing Moment Coefficient

Figures 5.4(a) to 5.4(d) show that the yaw coefficient for the tractor configuration was shifted upwards compared to the pusher and no propeller configurations. The yawing moment is produced as a consequence of the roll moment. The aircraft roll moment remains relatively constant until the stall of the right wing at  $\approx 12.5^\circ$  AoA. Hence the increase in the yawing moment as the aircraft AoA increases is likely due to the

## 5.1 Wind Tunnel Results

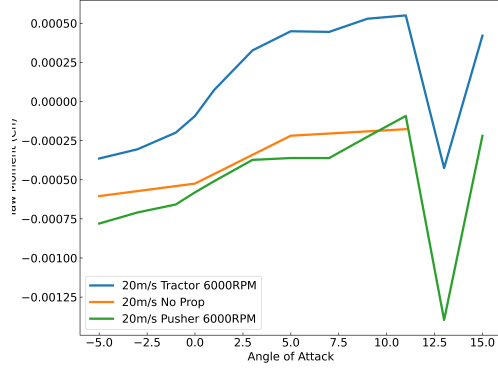
effects of the roll being magnified as flow separation occurs. The roll moment causes an adverse yaw effect where the MAV naturally tends to yaw in the opposite direction of the roll [119]. This is as the different lift and drag acting on each wing. As the angle of attack increases, the difference between the two wings in lift and drag increases, leading to an increase in the yaw moment for all configurations, airspeeds and propeller speeds except for the no propeller configuration when run at  $20\text{ms}^{-1}$ . As the angle of attack increases, the yaw moment increases until sharply dropping off in Figures 5.4(a) to 5.4(d). This is also due to the stall of the right-wing, creating a lift force imbalance as the left wing continues to produce a lift force while the right-wing experiences flow separation due to the increase in AoA. The yawing moment also sharply raises as the flow over the left wing also separates and stalls beyond  $\approx 12.5^\circ$  AoA. Several kinks are seen in Figures 5.4(a) to 5.4(d), the most notable being the changes in gradient seen for the pusher configuration with a propeller speed of 6000RPM in Figures 5.4(a) and 5.4(c) at  $\approx 0^\circ$ ,  $\approx 2.5^\circ$  and  $\approx 7.5^\circ$  AoA. These changes can be partially attributed to the roll moment changes seen in Figures 5.4(a) to 5.4(d), which creates an adverse yaw effect that acts opposite to the roll.



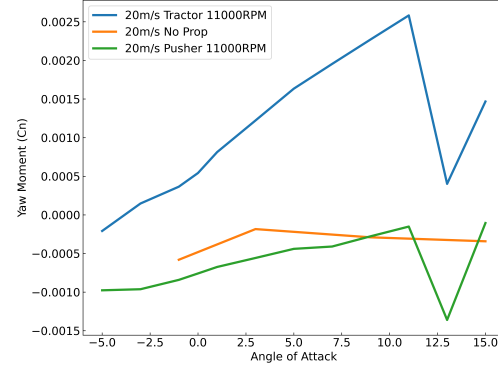
(a) Yawing Moment Coefficient at 10m/s airspeed and 6000RPM motor speed      (b) Yawing Moment Coefficient at 10m/s airspeed and 11000RPM motor speed

## Results and Discussion

---



(c) Yawing Moment Coefficient at 20m/s airspeed and 6000RPM motor speed



(d) Yawing Moment Coefficient at 20m/s airspeed and 11000RPM motor speed

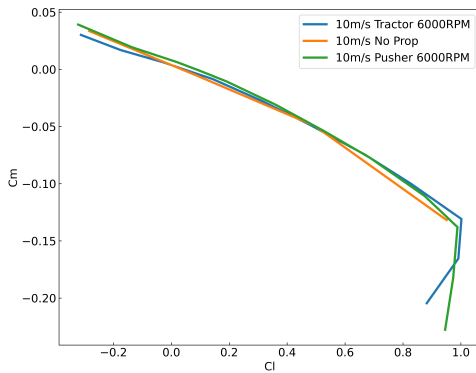
### 5.1.6 Static Margin

Figures 5.6(a) to 5.6(d) shows that the static margin for all configurations, airspeeds and propeller speeds tested was stable. The tractor configuration decreased the stability of the MAV except for the  $10\text{ms}^{-1}$  at 6000RPM propeller speed. This is also seen more clearly in Table 5.1 as static margin decreases from -0.155 to -0.107 when comparing the no propeller and tractor configurations at 11000RPM and  $10\text{ms}^{-1}$ . At 6000RPM propeller speed, the tractor configuration became less stable when airspeed increased from  $10\text{ms}^{-1}$  to  $20\text{ms}^{-1}$ , with the static margin decreasing from -0.116 to -0.106. This same trend was also seen for the pusher configuration at 6000RPM propeller speed, decreasing from -0.117 to -0.108. The opposite trend was seen when the propeller speed was increased to 11000RPM. The tractor and pusher configurations became more stable, increasing from -0.107 to -0.118 and from -0.156 to -0.173, respectively, when airspeed increased from  $10\text{ms}^{-1}$  to  $20\text{ms}^{-1}$ . The no propeller configuration became more stable at all propeller speeds as the airspeed increased from  $10\text{ms}^{-1}$  to  $20\text{ms}^{-1}$ .

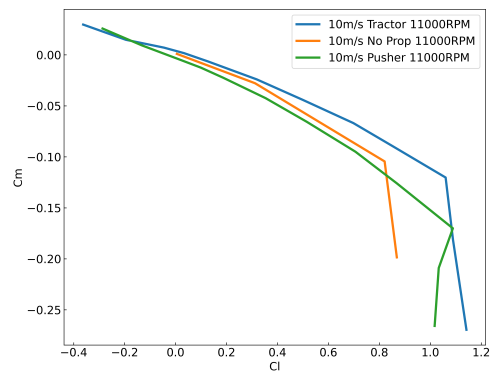
## 5.1 Wind Tunnel Results

Table 5.1 Static margin of all three configurations tested at airspeeds of  $10\text{ms}^{-1}$  and  $20\text{ms}^{-1}$ , and propeller speeds of 6000RPM and 11000RPM

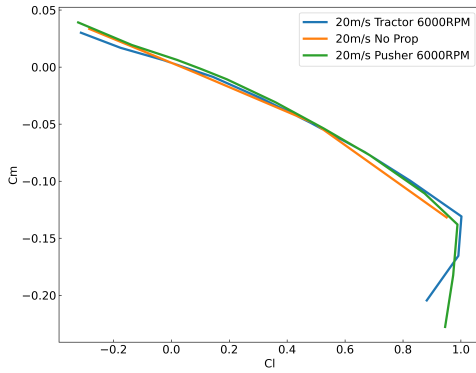
Configuration	Airspeed ( $\text{ms}^{-1}$ )	Propeller Speed (RPM)	Static Margin
Tractor	10	6000	-0.116
Tractor	20	6000	-0.106
No Propeller	10	6000	-0.100
No Propeller	20	6000	-0.107
Pusher	10	6000	-0.117
Pusher	20	6000	-0.108
Tractor	10	11000	-0.107
Tractor	20	11000	-0.118
No Propeller	10	11000	-0.155
No Propeller	20	11000	-0.159
Pusher	10	11000	-0.156
Pusher	20	11000	-0.173



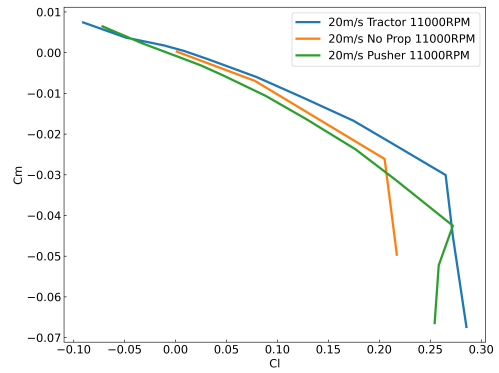
(a) Rolling Moment Coefficient at 10m/s airspeed and 6000RPM motor speed



(b) Rolling Moment Coefficient at 10m/s airspeed and 11000RPM motor speed



(c) Rolling Moment Coefficient at 20m/s airspeed and 6000RPM motor speed



(d) Rolling Moment Coefficient at 20m/s airspeed and 11000RPM motor speed

## Results and Discussion

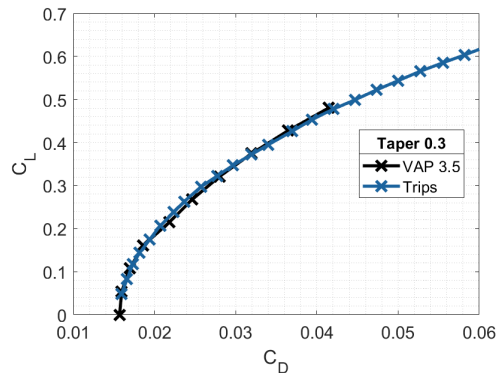
---

### 5.2 VAP 3.5 Validation

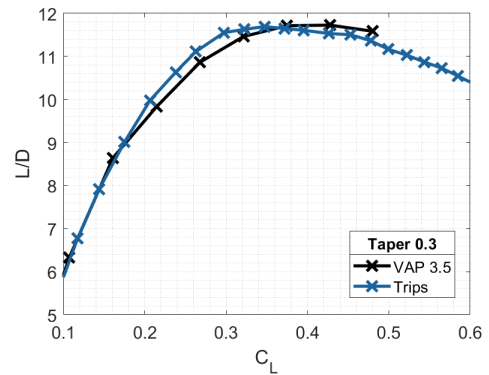
Low-speed aerodynamics have complex flow distributions and phenomena such as non-linear lift distribution and LSBs as discussed in Sections 2.13 and 3.3. To evaluate the use of VAP 3.5 for the wind tunnel tests conducted, a wing validation and model validation was performed with comparison to the GenMAV model, which has been previously evaluated with the Athena Vortex Lattice (AVL) method to estimate the stability derivatives and moments of the GenMAV. A rectangle wing shape was used in this analysis with the S5010, a root chord of 0.17m, AR of 3 and three taper configurations which are 0.3, 0.5 and 1.

#### 5.2.1 Wing Validation

Figure 5.7(a) show a wing validation against Fluent CFD results [120] with additional wing validation comparisons given in Appendix B. This data was taken at a Reynolds number of  $2.32 \times 10^5$  at a freestream velocity of  $20m/s$  and density  $1.225kg/m^3$ . Figures 5.7(a) showed strong agreement with the CFD results, as did all other wing shapes tested for the coefficient of lift and L/D ratios for the three tapered wings.



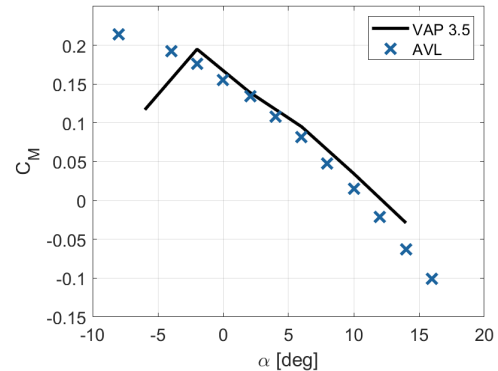
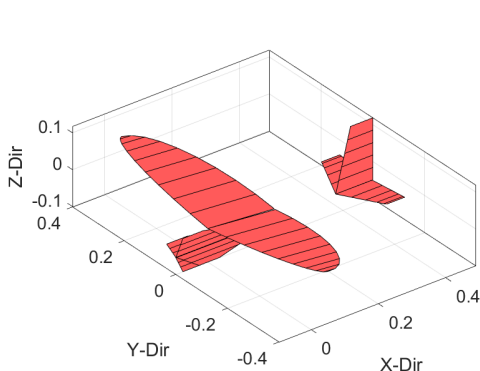
(a) Wing validation of  $C_L$  between VAP 3.5 and AVL with S5010 airfoil, root chord of 0.17m and taper ratio of 0.3 [120]



(b) Wing validation of L/D ratio between VAP 3.5 and AVL with S5010 airfoil, root chord of 0.17m and taper ratio of 0.3 [120]

### 5.2.2 GenMAV model validation

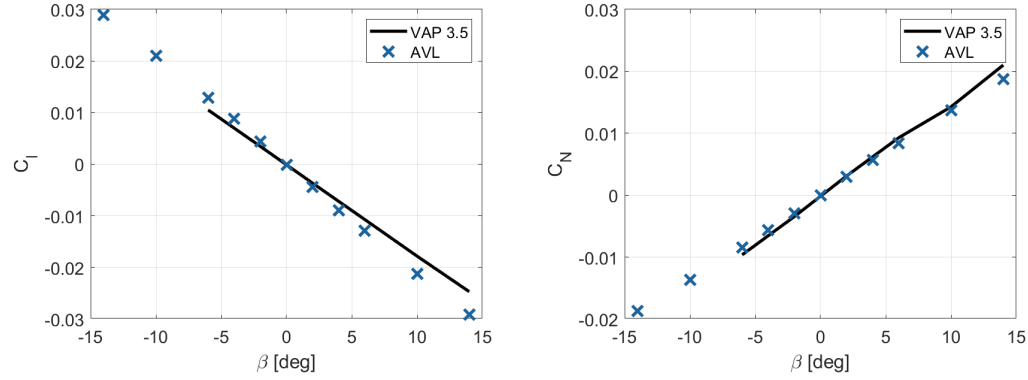
A model validation was also conducted to assess how accurate the stability coefficient calculations were for a non-propelled MAV. A validation against a propelled MAV could not be completed due to a lack of data in literature. This thesis potentially fills this gap. The GenMAV is a baseline MAV designed for further development and testing. Due to this it features many typical MAV aspects for its configuration. It features a conventional wing and empennage with a thin cambered plate airfoil. The thin cambered plate was approximated with the Eppler E387 to best match the camber of the GenMAV airfoil. The stability coefficients shown in Figures 5.8(b) to 5.8(d) show reasonable agreement with the AVL method [106]. The inaccuracies seen below  $0^\circ$  AoA in Figure 5.8(b) for the pitching moment are due to the way in which VAP 3.5 calculates the forces acting on the model. Discrepancies are also seen in Figures 5.8(c) and 5.8(d), however to a lesser extent. These discrepancies are more likely due to the geometry used to model the GenMAV not being exactly the same as features such as the curve of a fuselage profile are not implemented in current software [106].



(b) Pitching moment comparison for GenMAV between VAP 3.5 and AVL [106]

## Results and Discussion

---



(c) Rolling moment comparison for Gen- (d) Yawing moment comparison for Gen-  
MAV between VAP 3.5 and AVL [106] MAV between VAP 3.5 and AVL [106]

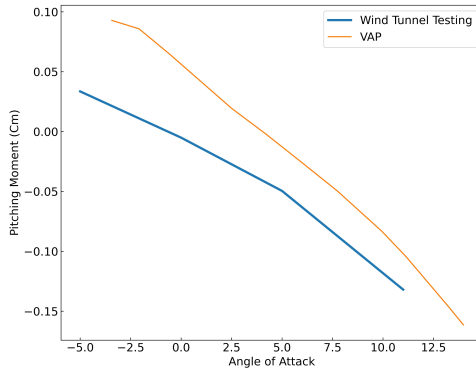
### 5.2.3 Validation of Wind Tunnel Results with VAP 3.5

To determine the accuracy of the wind tunnel results obtained and assess VAP 3.5's ability to calculate the stability coefficients analysed, a comparison was made between the wind tunnel and VAP 3.5 results for the three MAV configurations analysed.

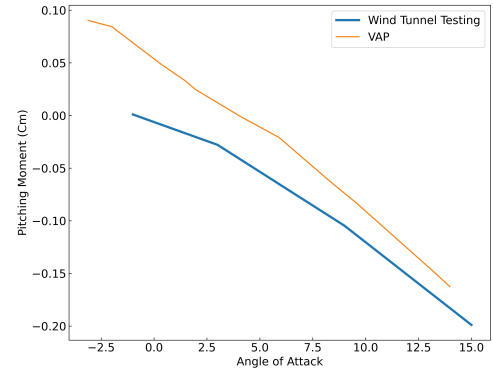
#### 5.2.3.1 No Propeller Configuration

Figure 5.10 outlines a partially completed run. All no-propeller VAP 3.5 analyses were run until the wing wake and tail wake had fully developed to most accurately determine the stability coefficients acting on the model. Figures 5.9(a) to 5.9(d) show that the pitching moment has similar slopes between the VAP 3.5 and wind tunnel results. This indicates a similar  $C_{m\alpha}$ , which describes the stability of the model in terms of the pitching moment. However, the magnitude of the pitching moment force is incorrectly calculated by the VAP 3.5 software. VAP 3.5 does not predict the forces at AoAs lower than  $0^\circ$  well. Hence these discrepancies are expected. Results indicate that further development is needed, and refinement of the geometry's detail could account for the offset seen in the pitching moment.

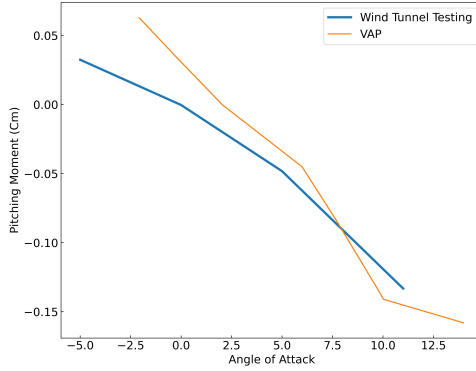
## 5.2 VAP 3.5 Validation



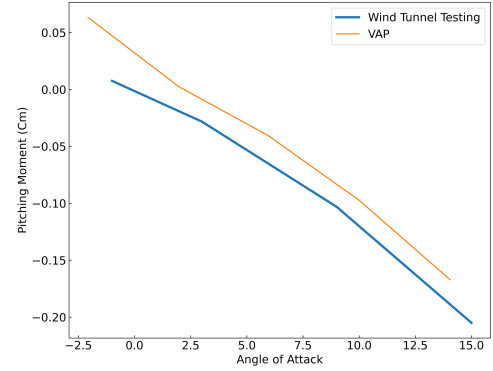
(a) Pitching Moment Coefficient at 10m/s airspeed for no propeller configuration



(b) Pitching Moment Coefficient at 10m/s airspeed for no propeller configuration



(c) Pitching Moment Coefficient at 20m/s airspeed for no propeller configuration



(d) Pitching Moment Coefficient at 20m/s airspeed for no propeller configuration

Figures 5.11(a) to 5.11(d) show that the rolling moment shows significant discrepancies for the no propeller configuration in all tested cases. The side force and moments calculations are still being tested in VAP 3.5 and are highly dependent on the geometry defined. While the geometry of the MAV model has been kept the same where possible, several features, such as the curve of the fuselage and wing, have been approximated with curved plates and approximate equations, respectively.

## Results and Discussion

---

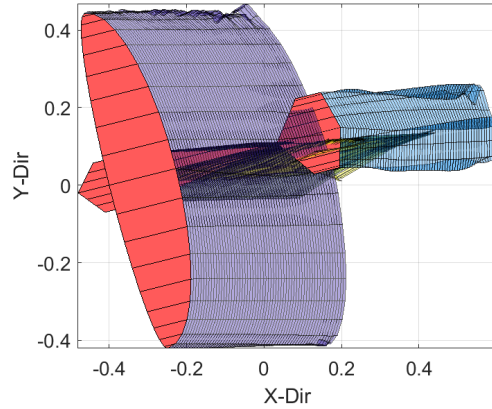
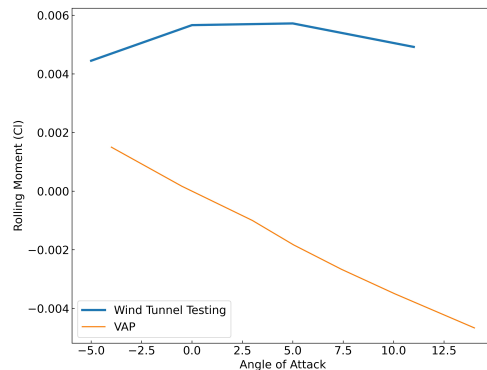
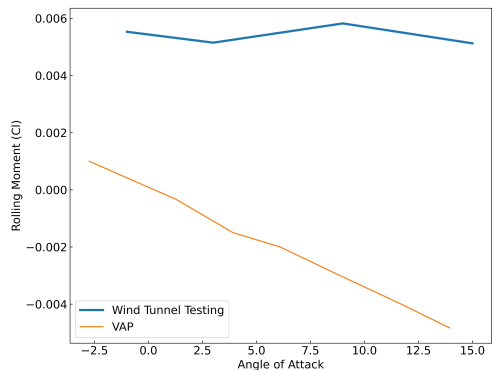


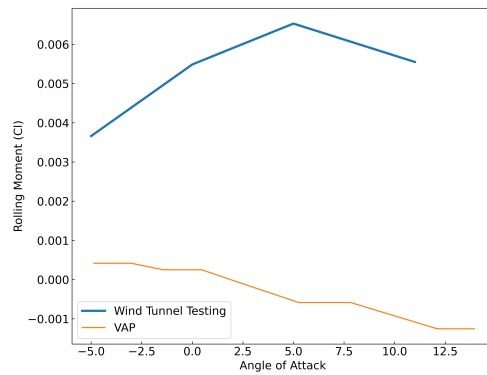
Fig. 5.10 No propeller configuration showing the start of the wake interference when run through VAP 3.5 at a sideslip angle of 15°



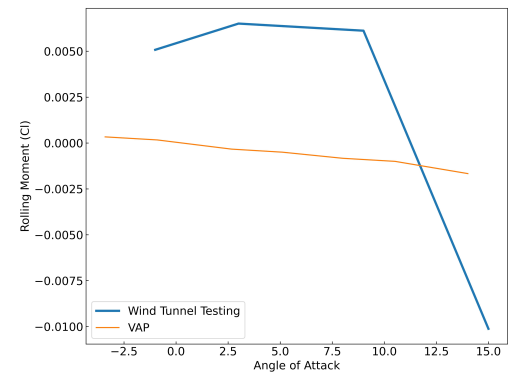
(a) Rolling Moment Coefficient at 10m/s airspeed for no propeller configuration



(b) Rolling Moment Coefficient at 10m/s airspeed for no propeller configuration



(c) Rolling Moment Coefficient at 20m/s airspeed for no propeller configuration



(d) Rolling Moment Coefficient at 20m/s airspeed for no propeller configuration

### 5.2.3.2 Tractor Configuration

The tractor configuration introduced a propeller in the VAP 3.5 simulations. VAP 3.5 is still currently testing propeller force and moment calculations as described in the current fcnROTORFORCE.m file [121]. The simulation for the tractor configuration was run until the propeller wake passed over the tail so that the wake interactions had been fully developed to assess the stability coefficients. Figure 5.12 shows a partially developed wake.

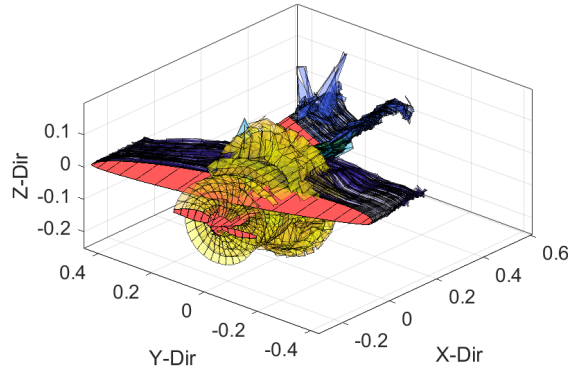
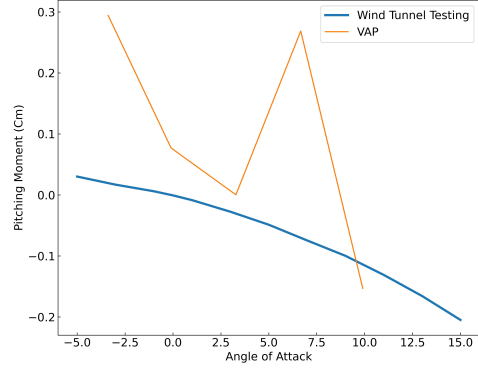


Fig. 5.12 VAP 3.5 simulation of tractor configuration showing propeller-wing wake interference

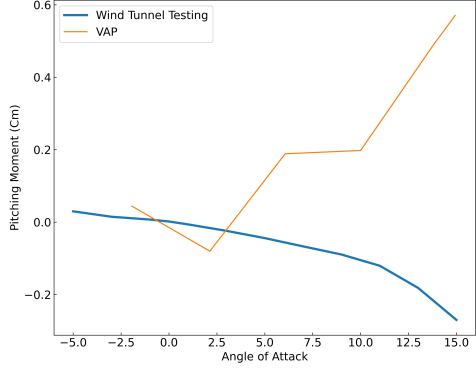
While the pitching moment showed the same general trend for the no-propeller analysis, the addition of the propeller significantly reduced the accuracy of the pitching moment coefficient. The addition of random increases in pitching moment such as that seen at  $7^\circ$  AoA in Figure 5.14(a) are unexpected and shows that there still needs to be a further improvement on the method which is being used to calculate the forces and moments created by the aircraft, along with how these translate to the main MAV model.

## Results and Discussion

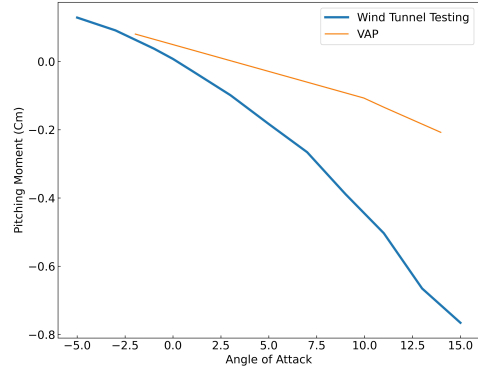
---



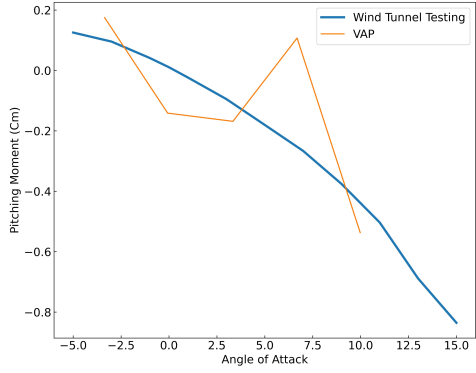
(a) Pitching Moment Coefficient at 10m/s airspeed and 6000RPM motor speed



(b) Pitching Moment Coefficient at 10m/s airspeed and 11000RPM motor speed



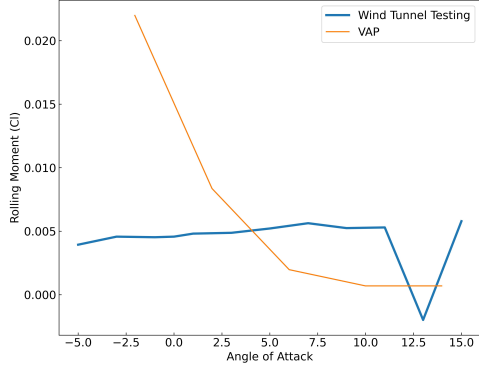
(c) Pitching Moment Coefficient at 20m/s airspeed and 6000RPM motor speed



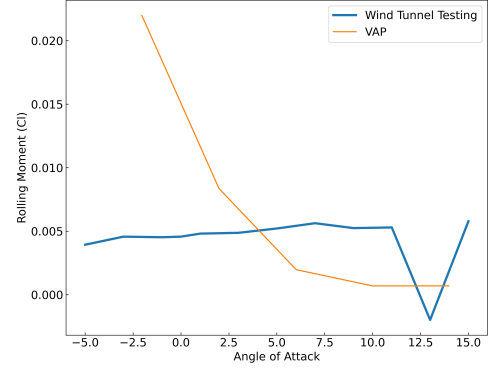
(d) Pitching Moment Coefficient at 20m/s airspeed and 11000RPM motor speed

The rolling moment of the VAP 3.5 software showed substantial discrepancies in magnitude and trend for Figures 5.14(a) to 5.14(c). Figure 5.14(d) begins to show similar trends to the wind tunnel tested results. However, the discrepancy is still too large to show an agreement. This is likely caused by the force and moments from the propeller and has not been tested with accurate results. The discrepancy can also be attributed to the geometry of the VAP 3.5 model, as it simplifies the actual MAV geometry.

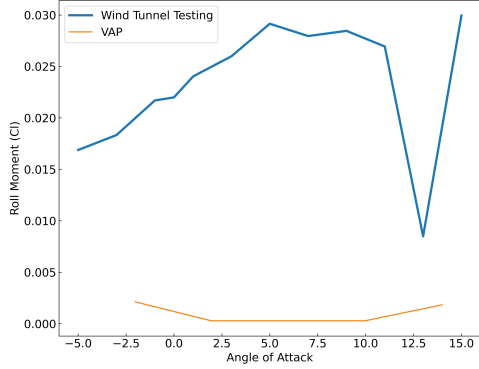
## 5.2 VAP 3.5 Validation



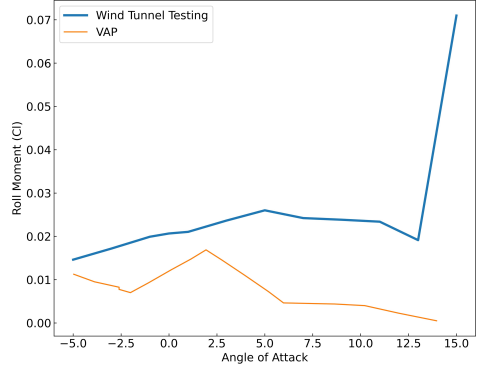
(a) Rolling Moment Coefficient at 10m/s airspeed and 6000RPM motor speed



(b) Rolling Moment Coefficient at 10m/s airspeed and 11000RPM motor speed



(c) Roll Moment Coefficient at 20m/s airspeed and 6000RPM motor speed

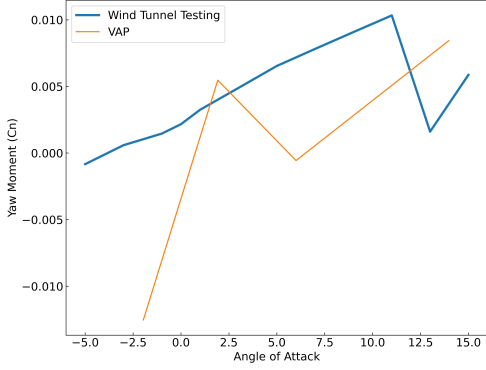


(d) Roll Moment Coefficient at 20m/s airspeed and 11000RPM motor speed

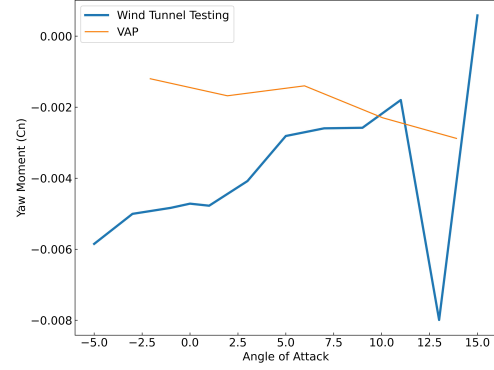
Figures 5.15(a) to 5.15(c) show the yaw moment between the VAP 3.5 and wind tunnel results. The yawing moment is influenced by the roll of the MAV, and wind tunnel testing showed a sharp drop, due to the right wing stalling before the left. There is a gradient change in Figure 5.15(a) as the AoA transitions from negative to positive. From  $6^\circ$  AoA, the gradient of the yawing moment is closer to what is expected. However, there is no general agreement between the VAP 3.5 and wind tunnel results in all cases analysed. The  $20\text{ms}^{-1}$  results are opposite to what is expected from wind tunnel testing, likely due to the same force and moment methods used by VAP 3.5.

## Results and Discussion

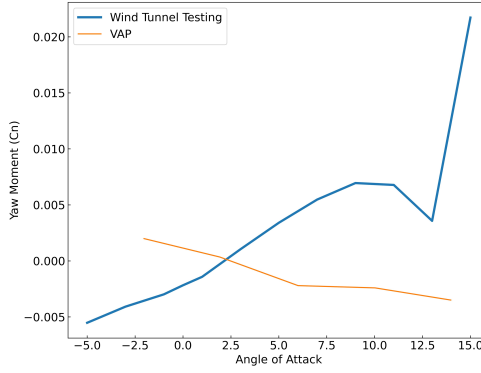
---



(a) Yawing Moment Coefficient at 10m/s airspeed and 11000RPM motor speed



(b) Yawing Moment Coefficient at 20m/s airspeed and 6000RPM motor speed



(c) Yawing Moment Coefficient at 20m/s airspeed and 11000RPM motor speed

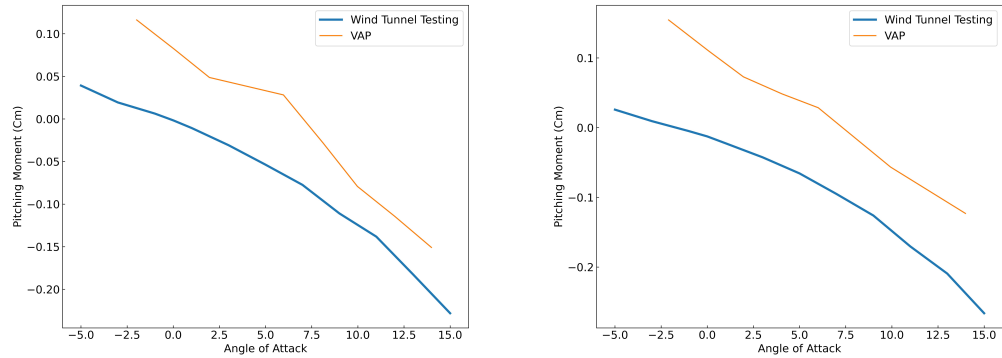
### 5.2.3.3 Pusher Configuration

The simulation was run until the wing wake had passed over the propeller as shown in Figures 5.16(a) and 5.16(b). Figures 5.17(a) to 5.17(d) show that the pitching moment was estimated to be larger in magnitude for the VAP 3.5 simulations and are more linear than expected. These discrepancies are likely due to the propeller force and moment calculations still being tested [121].

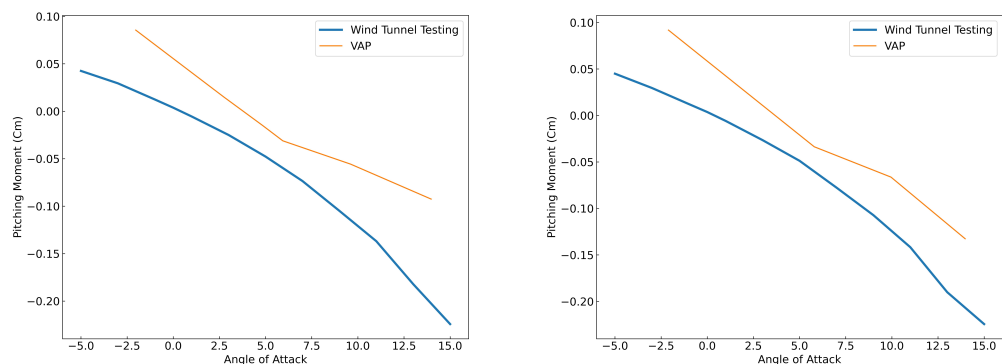
## 5.2 VAP 3.5 Validation



(a) Side view of the fully developed wake (b) Top view of the fully developed wake  
for the pusher configuration in VAP 3.5 for the pusher configuration in VAP 3.5



(a) Pitching Moment Coefficient at 10m/s airspeed and 6000RPM motor speed (b) Pitching Moment Coefficient at 10m/s airspeed and 11000RPM motor speed

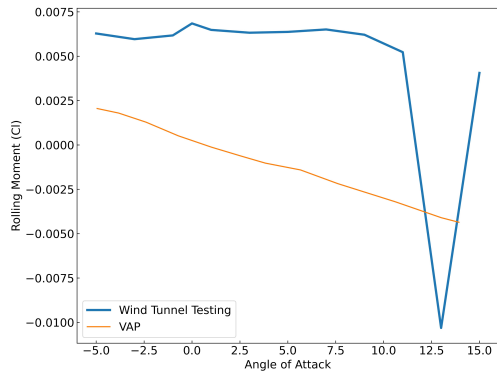


(c) Pitching Moment Coefficient at 20m/s airspeed and 6000RPM motor speed (d) Pitching Moment Coefficient at 20m/s airspeed and 11000RPM motor speed

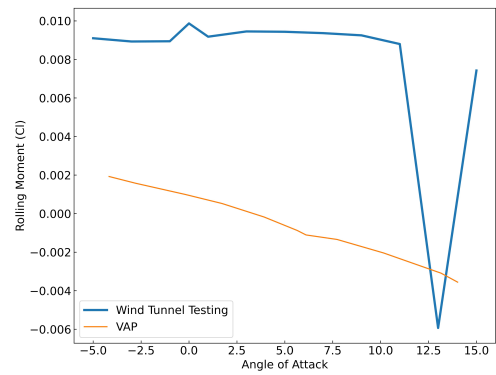
## Results and Discussion

---

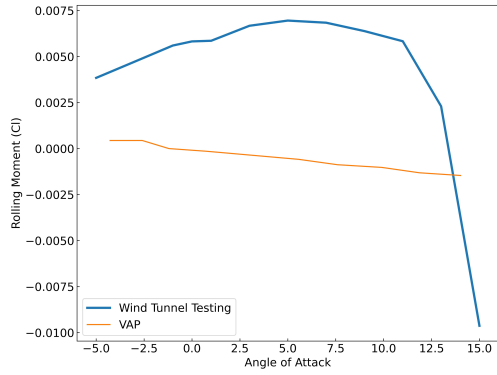
The rolling moment of the VAP 3.5 software showed substantial discrepancies in magnitude and trend for Figures 5.18(a) to 5.18(d). Figure 5.18(c) also implies that the motor torque effect has not been included in calculations to determine the stability coefficients as the rolling moment is very close to 0, which is unexpected due to the propeller torque effect, which should be generated as the wings experience an upwash on one side and a downwash on the other side of the propeller wake.



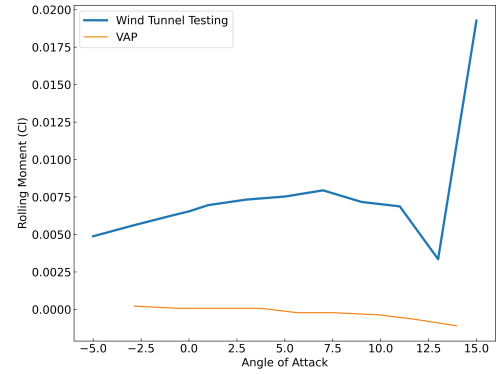
(a) Rolling Moment Coefficient at 10m/s airspeed and 6000RPM motor speed



(b) Rolling Moment Coefficient at 10m/s airspeed and 11000RPM motor speed



(c) Rolling Moment Coefficient at 20m/s airspeed and 6000RPM motor speed

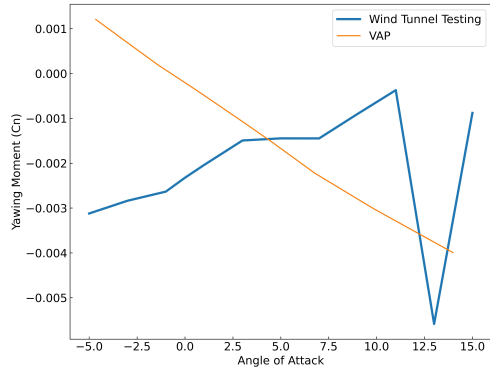


(d) Rolling Moment Coefficient at 20m/s airspeed and 11000RPM motor speed

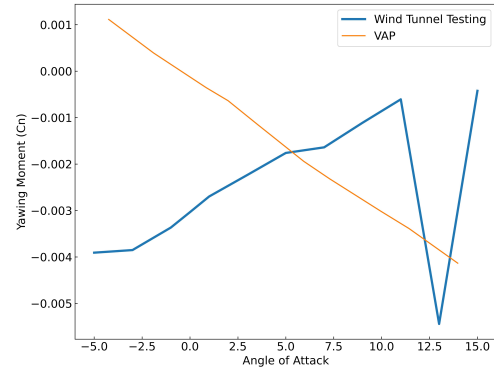
Figures 5.19(a) to 5.19(d), similarly to the tractor configuration, show a trend that is opposite to what is expected from wind tunnel testing and again is likely due to the

## 5.2 VAP 3.5 Validation

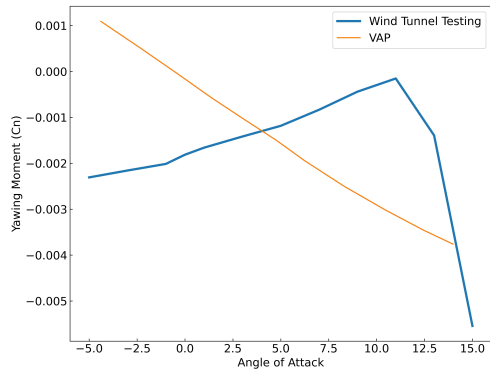
same force and moment methods still being under development and testing. Similar results were seen for the no propeller configuration with further details in Appendix B.



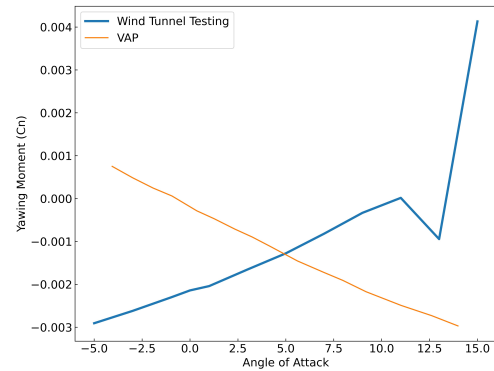
(a) Yawing Moment Coefficient at 10m/s airspeed and 6000RPM motor speed



(b) Yawing Moment Coefficient at 10m/s airspeed and 11000RPM motor speed



(c) Yawing Moment Coefficient at 20m/s airspeed and 6000RPM motor speed



(d) Yawing Moment Coefficient at 20m/s airspeed and 11000RPM motor speed

# Chapter 6

## Conclusions and Future Work

MAVs ability to be much quieter and concealed gives them a significant advantage over UAVs [2] and has led to an increasing interest in improving and understanding the aerodynamics and stability of MAV designs. MAV designs are much more challenging to design and manufacture due to the low-speed flight, small physical dimensions and low inertia. The low-speed and non-linear flight dynamics are of particular importance for MAV development. While many recent studies have investigated the effects of using a propeller, none so far have analysed a propeller mounted on a MAV to investigate the effects the addition of a propeller has on the stability of MAV designs. This thesis has covered the influence of an operating propeller mounted on three main MAV configurations to assess changes in the stability of a developed MAV model. The three configurations which have been investigated as the pusher, tractor and no propeller configurations.

This chapter outlines the work completed in this thesis and summarises the main conclusions. Key areas identified for further investigation have also been identified with suggestions made on areas which could provide key insights into this area of study.

### 6.1 Conclusions

A 3D printed MAV model using light-weight PLA and superlight-weight PLA was successfully designed in FreeCAD and tested in the 3x4 ft wind tunnel for stability coefficients and aerodynamic characteristics. These results were processed and validated against data produced by VAP 3.5 in order to assess the accuracy of the data produced and assess the suitability of using VAP 3.5 for analysing propeller-wing interactions.

The key conclusions determined from this investigation are:

- Increasing the airspeed and propeller speed delayed the MAV model's stall as the stall angle of attack increased in all configurations. The tractor configuration has a deeper stall when airspeed is at  $20\text{ms}^{-1}$ , which is undesirable to recover the MAV if a stall were to occur.
- The highest force coefficient (thrust minus drag) occurred when no propeller operated on the MAV model. The tractor configuration, in general, produces a lower magnitude force than the pusher configuration; hence, the force coefficient is lower for the tractor configuration. This is possibly due to a lower thrust being produced by the tractor configuration, however further investigation is needed.
- The pitching moment of the MAV model decreased as the angle of attack increased and indicated that the MAV was stable in all cases.
- The pusher configuration had a larger pitching moment compared with the no-propeller model and showed that the MAV became more stable in the pusher configuration. The opposite trend was seen with the tractor configuration; hence, the tractor configuration became less stable than the no-propeller MAV model.

## **Conclusions and Future Work**

---

- The pusher configuration shifts the rolling moment to a larger extent due to having a larger moment arm from the position of the propeller to the aerodynamic centre of the MAV model than the tractor configuration. In this case, the pusher configuration would require more input from control surfaces such as ailerons to correct this and maintain stability.
- The yawing coefficient for the tractor configuration was shifted upwards, increasing the yawing coefficient when compared to both the pusher and no propeller configurations. This was caused by the roll moment, which created an adverse yaw effect where the MAV naturally tends to yaw in the opposite direction of the roll. In this case, the tractor configuration would require a larger control surface than the no propeller and pusher configuration to maintain stability.
- Further investigation is required into the suitability of VAP 3.5 as a validation software for wing propeller interactions. Currently, the side forces and moment calculations are still in testing and, based on discrepancies found with wind tunnel testing, indicate that further work needs to be done regarding the side forces and moments generated by the propeller to determine the roll and yaw moment coefficients accurately.

## **6.2 Future Work**

The conclusions made in this thesis lead to many further investigations, which would greatly improve our understanding of MAV stability and propeller-wing interactions in low airspeed conditions. These include:

- An analysis into the effects of other parameters that define wing shapes such as sweep, dihedral and twist in both the MAV tractor and pusher configurations. Currently, only one wing shape has been analysed, and the influence of the wing

## **6.2 Future Work**

---

shape on the stability of the MAV would enable a greater understanding of the effects that wing parameters have on both the tractor and pusher configurations.

- Looking into the effects of propeller size could provide further insight into the influence of the wing-propeller interaction on the stability of the MAV in more detail.
- Further wind tunnel testing to investigate the yaw stiffness and dihedral effect would provide a complete understanding of the stability and the kind of control surfaces required for each configuration.
- Further refinement of the VAP 3.5 model geometry to better account for fuselage, tail and wing shapes would allow for more accurate stability coefficient calculation.
- An analysis of the suitability of VAP 3.5 as a validation software for wing propeller interactions would allow for a greater understanding of why the discrepancies seen are so significant. This could also be used to improve how the side forces and moments that are generated by the propeller are translated onto the main model to be tested and, as a consequence, the accuracy of the stability coefficients for yaw, roll and pitch.



# References

- [1] X. F. Liu, Z. W. Guan, Y. Q. Song, and D. S. Chen, “An optimization model of uav route planning for road segment surveillance,” *Journal of Central South University 2014 21:6*, vol. 21, pp. 2501–2510, 6 2014.
- [2] S. K. Chaturvedi, R. Sekhar, S. Banerjee, H. Kamal, and C. Author, “Comparative review study of military and civilian unmanned aerial vehicles (uavs),” *INCAS BULLETIN*, vol. 11, pp. 183–198, 2019.
- [3] J. Fan, D. Li, and R. Li, “Evaluation of mav/uav collaborative combat capability based on network structure,” *International Journal of Aerospace Engineering*, vol. 2018, 2018.
- [4] K. P. Valavanis and M. Kontitsis, “A historical perspective on unmanned aerial vehicles,” *Advances in Unmanned Aerial Vehicles*, pp. 15–46, 2 2007.
- [5] M. S. J and H. Michael, “Design of micro air vehicles and flight test validation,” 022.
- [6] Z. M. Yehia, M. Abdallah, and A. Elshaafi, “Classification of uavs with respect to size and weight | download scientific diagram,” 2012.
- [7] “Micro-air-vehicle enviroment system | projects | research & production | digital worlds institute | college of the arts | university of florida,” 2022.
- [8] “World’s first hummingbird-like unmanned aircraft system takes flight,” 2011.
- [9] K. Dalamagkidis, “On integrating unmanned aircraft systems into the national airspace system.,” *Intelligent Systems, Control and Automation: Science and Engineering*, vol. 36, 2009.
- [10] R. Sabatini, S. Ramasamy, A. Gardi, and L. R. Salazar, “Low-cost sensors data fusion for small size unmanned aerial vehicles navigation and guidance.,” 2013.
- [11] “Hunter rq-5a / mq-5b/c uav - army technology,” 2021.
- [12] “Iai rq-2 pioneer,” 2022.
- [13] “Mq-9 reaper uav (cropped) - general atomics mq-9 reaper - wikipedia,” 2022.
- [14] “Japan’s first global hawk begins flying at northrop’s california drone hub,” 2021.

## References

---

- [15] B. Stanford, P. Ifju, R. Albertani, and W. Shyy, “Fixed membrane wings for micro air vehicles: Experimental characterization, numerical modeling, and tailoring,” *Progress in Aerospace Sciences*, vol. 44, pp. 258–294, 5 2008.
- [16] M. Lasek, J. Pietrucha, M. Złocka, and K. Sibilski, “Analogies between rotary and flapping wings from control theory point of view,” *AIAA Atmospheric Flight Mechanics Conference and Exhibit*, 2001.
- [17] M. F. Platzer, K. D. Jones, J. Young, and J. C. Lai, “Flapping wing aerodynamics: Progress and challenges,” <https://doi.org/10.2514/1.29263>, vol. 46, pp. 2136–2149, 5 2012.
- [18] K. Sibilski, M. Nowakowski, D. Rykaczewski, P. Szczepaniak, A. Zyluk, A. Sibilska-Mroziewicz, M. Garbowski, and W. Wróblewski, “Identification of fixed-wing micro aerial vehicle aerodynamic derivatives from dynamic water tunnel tests,” *Aerospace 2020, Vol. 7, Page 116*, vol. 7, p. 116, 8 2020.
- [19] S. Duranti, G. Conte, D. Lundstrom, P. Rudol, M. Wzorek, and P. Doherty, “Linkmav, a prototype rotary wing micro aerial vehicle,” 2007.
- [20] K. D. Jones and M. F. Platzer, “Flapping-wing propelled micro air vehicles,” *Handbook of Unmanned Aerial Vehicles*, pp. 1359–1383, 2015.
- [21] T. A. Ward, C. J. Fearday, E. Salami, and N. B. Soin, “A bibliometric review of progress in micro air vehicle research;,” <http://dx.doi.org/10.1177/1756829316670671>, vol. 9, pp. 146–165, 2 2017.
- [22] K. Amadori, D. Lundström, and P. Krus, “Automated design and fabrication of micro-air vehicles,” *Proceedings of the Institution of Mechanical Engineers, Part G: Journal of Aerospace Engineering*, vol. 226, pp. 1271–1282, 10 2012.
- [23] R. Vijayanandh, M. S. Kumar, K. Naveenkumar, G. R. Kumar, and R. N. Kumar, “Design optimization of advanced multi-rotor unmanned aircraft system using fsi,” *Lecture Notes in Mechanical Engineering*, pp. 299–310, 2019.
- [24] M. Radmanesh, O. Nematollahi, M. Nili-Ahmabad, and M. Hassanalian, “A novel strategy for designing and manufacturing a fixed wing mav for the purpose of increasing maneuverability and stability in longitudinal axis,” *Journal of Applied Fluid Mechanics*, vol. 7, pp. 435–446, 2014.
- [25] A. Aboelezz, M. Hassanalian, A. Desoki, B. Elhadidi, and G. El-Bayoumi, “Design, experimental investigation, and nonlinear flight dynamics with atmospheric disturbances of a fixed-wing micro air vehicle,” *Aerospace Science and Technology*, vol. 97, p. 105636, 2 2020.
- [26] A. Aboelezz, O. Mohamady, M. Hassanalian, and B. Elhadidi, “Nonlinear flight dynamics and control of a fixed-wing micro air vehicle: Numerical, system

## References

---

- identification and experimental investigations,” *Journal of Intelligent & Robotic Systems* 2021 101:3, vol. 101, pp. 1–18, 3 2021.
- [27] K. C. Aleksander, “Military use of unmanned aerial vehicles – a historical study,” *Safety & Defense*, vol. 4, pp. 17–21, 10 2018.
- [28] K. NONAMI, “Prospect and recent research & development for civil use autonomous unmanned aircraft as uav and mav,” *Journal of System Design and Dynamics*, vol. 1, pp. 120–128, 2007.
- [29] “Inevitable bedfellows? cooperation on military technology for the development of uavs and cruise missiles in the asia-pacific | policy commons,” 2022.
- [30] W. W. Greenwood, J. P. Lynch, and D. Zekkos, “Applications of uavs in civil infrastructure,” *Journal of Infrastructure Systems*, vol. 25, p. 04019002, 1 2019.
- [31] K. Saytov, N. Abdujabarov, T. Jonibek, K. Saytov, and S. Bobomurodov, “Prospects of the development of unmanned aerial vehicles (uavs),” *PROSPECTS OF THE DEVELOPMENT OF UNMANNED AERIAL VEHICLES (UAVs)*, vol. 4, 2020.
- [32] “(139) pinterest,” 2022.
- [33] S. Martin, “How gliders fly, and how they’re different than powered aircraft | boldmethod,” 7 2015.
- [34] “Reference frames and how they are used in inertial navigation · vectornav,” 2022.
- [35] K. P. Valavanis, “Advances in unmanned aerial vehicles,” *Advances in Unmanned Aerial Vehicles*, 2007.
- [36] K. L. Cook, “The silent force multiplier: The history and role of uavs in warfare,” *IEEE Aerospace Conference Proceedings*, 2007.
- [37] J. H. MacConnell, “Ishm & design: A review of the benefits of the ideal ishm system,” *IEEE Aerospace Conference Proceedings*, 2007.
- [38] R. Kumar, “Tactical reconnaissance: Uavs versus manned aircraft,” 1997.
- [39] M. Keenon and J. Grasmeyer, “Development of two mavs and vision of the future of mav design,” *American Institute of Aeronautics and Astronautics AIAA International Air and Space Symposium and Exposition: The Next 100 Years - Dayton, Ohio (14 July 2003 - 17 July 2003)*, 7 2003.
- [40] A. O. Agbeyangi, J. O. Odiete, and A. B. Olorunlomerue, “Review on uavs used for aerial surveillance development of an english to yoruba language numeral translation system view project wireless sensor network for potentially harmful

## References

---

- gasses view project review on uavs used for aerial surveillance,” *Journal of Multidisciplinary Engineering Science and Technology (JMEST)*, vol. 3, pp. 2458–9403, 2016.
- [41] O. Crivoi, I. Doroftei, and F. Adascalitei, “A survey on unmanned aerial vehicles based on coanda effect,” *TEHNOMUS - New Technologies and Products in Machine Manufacturing Technologies*, 2013.
  - [42] D. J. Snyder, “Design requirements for weaponizing man-portable uas in support of counter-sniper operations,” 2011.
  - [43] X. Wang, Z. Huang, G. Sui, and H. Lian, “Analysis on the development trend of future uav equipment technology,” *Academic Journal of Engineering and Technology Science*, vol. 2, pp. 114–121, 4 2019.
  - [44] R. Yin, W. Li, Z. Q. Wang, and X. X. Xu, “The application of artificial intelligence technology in uav,” *Proceedings - 2020 5th International Conference on Information Science, Computer Technology and Transportation, ISCTT 2020*, pp. 238–241, 11 2020.
  - [45] J. Jackson, G. Ellingson, and T. McLain, “Rosflight: A lightweight, inexpensive mav research and development tool,” *2016 International Conference on Unmanned Aircraft Systems, ICUAS 2016*, pp. 758–762, 6 2016.
  - [46] M. V. Peppa, J. Hall, J. Goodyear, and J. P. Mills, “Photogrammetric assessment and comparison of dji phantom 4 pro and phantom 4 rtk small unmanned aircraft systems,” *School of Engineering, Newcastle University*, 2019.
  - [47] M. Bronz, J. M. Moschetta, P. Brisset, and M. Gorraz, “Towards a long endurance mav:,” <http://dx.doi.org/10.1260/175682909790291483>, vol. 1, pp. 241–254, 12 2009.
  - [48] M. HASSANALIAN, R. SALAZAR, and A. ABDELKEFI, “Conceptual design and optimization of a tilt-rotor micro air vehicle,” *Chinese Journal of Aeronautics*, vol. 32, pp. 369–381, 2 2019.
  - [49] C. A. Paulson, A. Sóbester, and J. P. Scanlan, “The rapid development of bespoke small unmanned aircraft: A proposed design loop,” *The Aeronautical Journal*, vol. 121, pp. 1683–1710, 11 2017.
  - [50] K. Harikumar, J. V. Pushpangathan, and S. Sundaram, “Effects of propeller flow on the longitudinal and lateral dynamics and model couplings of a fixed-wing micro air vehicle,” *Proceedings of the Institution of Mechanical Engineers, Part G: Journal of Aerospace Engineering*, vol. 235, 2021.
  - [51] K. Chinwicharnam, D. Ariza, J. M. Moschetta, and C. Thipyopas, “Propeller interaction,” in *Aerodynamic characteristics of a low aspect ratio wing and propeller interaction for a tilt-body MAV*, vol. 5, 2013.

## References

---

- [52] T. A. Shams, S. I. A. Shah, A. Javed, and S. H. R. Hamdani, “Airfoil selection procedure, wind tunnel experimentation and implementation of 6dof modeling on a flyingwing micro aerial vehicle,” *Micromachines*, vol. 11, 2020.
- [53] A. Durai, “Experimental investigation of lift and drag characteristics of a typical mav under propeller induced flow:,” <http://dx.doi.org/10.1260/1756-8293.6.1.63>, vol. 6, pp. 63–72, 3 2014.
- [54] T. A. Shams, S. I. A. Shah, A. Shahzad, A. Javed, and K. Mehmod, “Experimental investigation of propeller induced flow on flying wing micro aerial vehicle for improved 6dof modeling,” *IEEE Access*, vol. 8, 2020.
- [55] Z. Chen and F. Yang, “Propeller slipstream effect on aerodynamic characteristics of micro air vehicle at low reynolds number,” *Appl. Sci. 2022*, vol. 12, p. 4092, 2022.
- [56] A. A. Huq, R. A. Sankar, C. Lakshmanan, C. Rukesh, D. S. Kulkarni, M. B. Subramanya, and B. N. Rajani, “Numerical prediction of aerofoil aerodynamics at low reynolds number for mav application,” *Computational & Theoretical Fluid Dynamics Division National Aerospace Laboratories*, 2009.
- [57] J. Winslow, H. Otsuka, B. Govindarajan, and I. Chopra, “Basic understanding of airfoil characteristics at low reynolds numbers (104–105),” *Journal of Aircraft*, vol. 55, pp. 1050–1061, 12 2018.
- [58] H. Liu and H. Aono, “Size effects on insect hovering aerodynamics: an integrated computational study,” *Bioinspiration & Biomimetics*, vol. 4, p. 015002, 3 2009.
- [59] N. I. Ismail, “Aerodynamic performances of twist morphing mav wing,” 2015.
- [60] “Butterfly definition and meaning | collins english dictionary,” 2022.
- [61] “Pheasant stock photos, royalty free pheasant images | depositphotos,” 2022.
- [62] “Light aircraft 2-lateral view white background 3d rendering ilustracion 3d stock illustration - illustration of technology, isolated: 231762604,” 2022.
- [63] “Jp scheinelier: Boeing 747-400.,” 2020.
- [64] W. Null, A. Noseck, and S. Shkarayev, “Effects of propulsive-induced flow on the aerodynamics of micro air vehicles,” *Collection of Technical Papers - AIAA Applied Aerodynamics Conference*, vol. 1, pp. 198–216, 2005.
- [65] G. K. Ananda, M. S. Selig, and R. W. Deters, “Experiments of propeller-induced flow effects on a low-reynolds-number wing,” *AIAA Journal*, vol. 56, pp. 3279–3294, 6 2018.

## References

---

- [66] P. M. Munday, K. Taira, T. Suwa, D. Numata, and K. Asai, “Nonlinear lift on a triangular airfoil in low-reynolds-number compressible flow,” *Journal of Aircraft*, vol. 52, pp. 924–931, 12 2015.
- [67] S. S. Bhat, J. Zhao, J. Sheridan, K. Hourigan, and M. C. Thompson, “Aspect ratio studies on insect wings,” *Physics of Fluids*, vol. 31, p. 121301, 12 2019.
- [68] G. E. Torres and T. J. Mueller, “Low aspect ratio aerodynamics at low reynolds numbers,” <https://doi.org/10.2514/1.439>, vol. 42, pp. 865–873, 5 2012.
- [69] P. Cosyn and J. Vierendeels, “Numerical investigation of low-aspect-ratio wings at low reynolds numbers,” <https://doi.org/10.2514/1.16991>, vol. 43, pp. 713–722, 5 2012.
- [70] M. T, “Low reynolds number vehicles,” 1985.
- [71] P. Cosyn and J. Vierendeels, “Numerical investigation of low-aspect-ratio wings at low reynolds numbers,” *Journal of Aircraft*, vol. 43, pp. 713–722, 2006.
- [72] S. Ravi, “The influence of turbulence on a flat plate aerofoil at reynolds numbers relevant to mavs,” 2011.
- [73] B. Perot and H. Wang, “Modeling separation and reattachment using the turbulent potential model,” *Engineering Turbulence Modelling and Experiments* 4, pp. 145–154, 1 1999.
- [74] A. Mohamed, K. Massey, S. Watkins, and R. Clothier, “The attitude control of fixed-wing mavs in turbulent environments,” *Progress in Aerospace Sciences*, vol. 66, pp. 37–48, 4 2014.
- [75] O. Marxen and U. Rist, “Mean flow deformation in a laminar separation bubble: separation and stability characteristics,” *Journal of Fluid Mechanics*, vol. 660, pp. 37–54, 2010.
- [76] P. Crimi and B. L. Reeves, “Analysis of leading-edge separation bubbles on airfoils,” *AIAA JOURNAL*, vol. 14, 1976.
- [77] K. S. Choi, “The rough with the smooth,” *Nature 2006* 440:7085, vol. 440, pp. 754–754, 4 2006.
- [78] J. H. McMaster, “The flight of the bumblebee and related myths of entomological engineering: Bees help bridge the gap between science and engineering on jstor,” 1989.
- [79] B. A. Roccia, S. Preidikman, M. L. Verstraete, and D. T. Mook, “Influence of spanwise twisting and bending on lift generation in mav-like flapping wings,” *Journal of Aerospace Engineering*, vol. 30, p. 04016079, 8 2016.

## References

---

- [80] H. Winter, “Flow phenomena on plates and airfoils of short span - unt digital library,” 1936.
- [81] S. Qin, Z. Weng, Z. Li, Y. Xiang, and H. Liu, “On the controlled evolution for wingtip vortices of a flapping wing model at bird scale,” *Aerospace Science and Technology*, vol. 110, p. 106460, 3 2021.
- [82] K. Tufan, “Development of wingtip vortices over a wing section | download scientific diagram,” 2015.
- [83] H. Z. Langley, “Tech caz n0 s national advisory committee for aeronautics aerodynamic characteristics of several airfoils of low aspect ratio,” *NATIONAL ADVISORY COMMITTEE FOR AERONAUTICS*, 1936.
- [84] A. C. DeVoria and K. Mohseni, “A vortex model for forces and moments on low-aspect-ratio wings in side-slip with experimental validation,” *Proceedings of the Royal Society A: Mathematical, Physical and Engineering Sciences*, vol. 473, 2 2017.
- [85] S. Watkins, J. Milbank, B. J. Loxton, and W. H. Melbourne, “Atmospheric winds and their implications for microair vehicles,” <https://doi.org/10.2514/1.22670>, vol. 44, pp. 2591–2600, 5 2012.
- [86] M. Shields and K. Mohseni, “Inherent stability modes of low-aspect-ratio wings,” *Journal of Aircraft*, vol. 52, pp. 141–155, 1 2015.
- [87] T. J. Mueller and J. D. DeLaurier, “Aerodynamics of small vehicles,” <http://dx.doi.org/10.1146/annurev.fluid.35.101101.161102>, vol. 35, pp. 89–111, 11 2003.
- [88] A. Pelletier and T. J. Mueller, “Low reynolds number aerodynamics of low-aspect-ratio, thin/flat/cambered-plate wings,” <https://doi.org/10.2514/2.2676>, vol. 37, pp. 825–832, 5 2012.
- [89] P. L., “Mutual influence of wings and propeller - unt digital library,” 1921.
- [90] L. R. Miranda and J. E. Brennan, “Aerodynamic effects of wingtip-mounted propellers and turbines.,” *AIAA Paper*, pp. 221–228, 1986.
- [91] T. Sinnige, N. V. Arnhem, T. C. Stokkermans, G. Eitelberg, and L. L. Veldhuis, “Wingtip-mounted propellers: Aerodynamic analysis of interaction effects and comparison with conventional layout,” *Journal of Aircraft*, vol. 56, pp. 295–312, 2019.
- [92] L. L. Veldhuis and P. M. Heyma, “Aerodynamic optimisation of wings in multi-engined tractor propeller arrangements,” *Aircraft Design*, vol. 3, pp. 129–149, 9 2000.

## References

---

- [93] L. Veldhuis, “Review of propeller-wing aerodynamic interference,” 2004.
- [94] M. H. Rizk, “Propeller in slipstream/wing interaction in the transonic regime,” <https://doi.org/10.2514/3.57482>, vol. 18, pp. 184–191, 5 2012.
- [95] G. Ferraro, T. Kipouros, A. M. Savill, A. Rampurawala, and C. Agostinelli, “Propeller-wing interaction prediction for early design,” *52nd AIAA Aerospace Sciences Meeting - AIAA Science and Technology Forum and Exposition, SciTech 2014*, 2014.
- [96] H. Aminaei, M. D. Manshadi, and A. R. Mostofizadeh, “Experimental investigation of propeller slipstream effects on the wing aerodynamics and boundary layer treatment at low reynolds number,” *Proceedings of the Institution of Mechanical Engineers, Part G: Journal of Aerospace Engineering*, vol. 233, pp. 3033–3041, 6 2019.
- [97] L. Prandtl, “Mutual influence of wings and propeller,” 1931.
- [98] A. Franke and F. Weinig, “The effect of the slipstream on an airplane wing - nasa technical reports server (ntrs),” 1939.
- [99] A. Jameson, “(pdf) analysis of wing slipstream flow interaction,” 1970.
- [100] N. Ellis, “Aerodynamics of wing-slipstream interaction: a numerical study,,” 1971.
- [101] L. Veldhuis, “Review of propeler-wing aerodynamics,” 2004.
- [102] L. Veldhuis, T. Stokkermans, T. Sinnige, and G. Eitelberg, “Analysis of swirl recovery vanes for increased propulsive efficiency in tractor propeller aircraft,” *30th Congress of the International Council of the Aeronautical Sciences. 60.,* 2016.
- [103] J. Shen, Y. Su, Q. Liang, and X. Zhu, “Calculation and identification of the aerodynamic parameters for small-scaled fixed-wing uavs,” *Sensors 2018, Vol. 18, Page 206*, vol. 18, p. 206, 1 2018.
- [104] B. Roberts, R. Lind, and M. Kumar, “Polynomial chaos analysis of mav’s in turbulence,” *AIAA Atmospheric Flight Mechanics Conference 2011*, 2011.
- [105] P. K. K. David R. Dowling, Ira Cohen, “Aerodynamics,” *Fluid Mechanics*, pp. 691–728, 1 2012.
- [106] K. Stewart, J. Wagener, G. Abate, and M. Salichon, “Aiaa 2007-667,” in *Design of the air force research laboratory micro aerial vehicle research configuration*, vol. 12, 2007.
- [107] P. Hrad, “Conceptual design tool for fuel-cell powered micro air vehicles,” *Defense Technical Information Center*, 2010.

- [108] K. Zhang, B. Shah, and O. Bilgen, “Low-reynolds-number aerodynamic characteristics of airfoils with piezocomposite trailing surfaces,” *AIAA Journal*, vol. 60, pp. 2701–2706, 4 2022.
- [109] W. Bollay, “A non-linear wing theory and its application to rectangular wings of small aspect ratio,” *ZAMM - Journal of Applied Mathematics and Mechanics / Zeitschrift für Angewandte Mathematik und Mechanik*, vol. 19, pp. 21–35, 1 1939.
- [110] S. M. Belotserkovskii, “Calculation of the flow around wings of arbitrary planform over a wide range of angles of attack,” *Fluid Dynamics 1972 3:4*, vol. 3, pp. 20–27, 7 1968.
- [111] V. Gomez, N. Gomez, J. Rodas, E. Paiva, M. Saad, and R. Gregor, “Pareto optimal pid tuning for px4-based unmanned aerial vehicles by using a multi-objective particle swarm optimization algorithm,” *Aerospace 2020, Vol. 7, Page 71*, vol. 7, p. 71, 6 2020.
- [112] A. Boutemedjet, M. Samardžić, L. Rebhi, Z. Rajić, and T. Mouada, “Uav aerodynamic design involving genetic algorithm and artificial neural network for wing preliminary computation,” *Aerospace Science and Technology*, vol. 84, pp. 464–483, 1 2019.
- [113] J. R. Parga, M. F. Reeder, T. Leveron, and K. Blackburn, “Experimental study of a micro air vehicle with a rotatable tail,” *Journal of Aircraft*, vol. 44, 2007.
- [114] S. Jana, H. Kandath, M. Shewale, and M. S. Bhat, “Effect of propeller-induced flow on the performance of biplane micro air vehicle dynamics,” *Proceedings of the Institution of Mechanical Engineers, Part G: Journal of Aerospace Engineering*, vol. 234, pp. 716–728, 3 2020.
- [115] K. Szwedziak, T. Łusiak, R. Babel, P. Winiarski, S. Podsedek, P. Doležal, and G. Niedbała, “Wind tunnel experiments on an aircraft model fabricated using a 3d printing technique,” *Journal of Manufacturing and Materials Processing 2022, Vol. 6, Page 12*, vol. 6, p. 12, 1 2022.
- [116] J. Butt, R. Bhaskar, and V. Mohaghegh, “Investigating the effects of extrusion temperatures and material extrusion rates on fff-printed thermoplastics,” *International Journal of Advanced Manufacturing Technology*, vol. 117, pp. 2679–2699, 12 2021.
- [117] K. Olasek and P. Wiklak, “Application of 3d printing technology in aerodynamic study,” *Journal of Physics: Conference Series*, vol. 530, p. 012009, 8 2014.
- [118] J. A. Cole, M. D. Maughmer, M. Kinzel, and G. Bramesfeld, “Higher-order free-wake method for propeller-wing systems,” *Journal of Aircraft*, vol. 56, pp. 150–165, 9 2019.

## References

---

- [119] D. Arivoli, R. Dodamani, R. Antony, C. S. Suraj, G. Ramesh, and S. Ahmed, “Experimental studies on a propelled micro air vehicle,” *29th AIAA Applied Aerodynamics Conference 2011*, 2011.
- [120] D. Trips, “Aerodynamic design and optimization of a long range mini-uav,” 2010.
- [121] “raalf/vap3 at vap3.5.”

# Appendix A

## Wind Tunnel Results

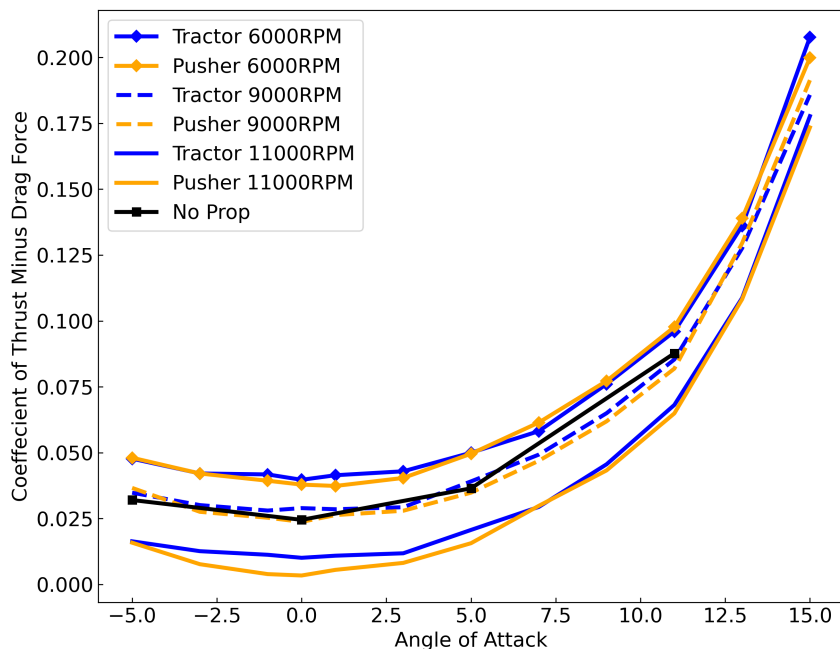


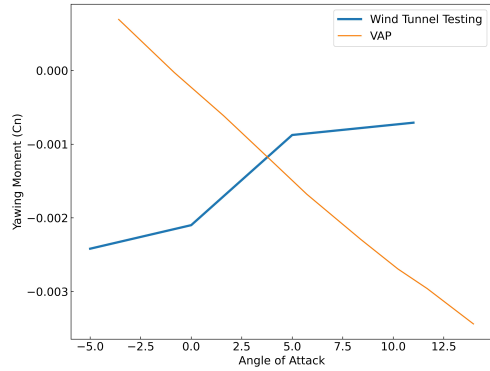
Fig. A.1 Coefficient of drag variation at 20ms airspeed for the tractor, pusher and no propeller configuration

Figure A.1 shows that as the airspeed increased to  $20\text{ms}^{-1}$  the tractor and pusher configuration at 6000RPM began windmilling and hence these coefficient of force curves have been shifted upwards from the no propeller model.

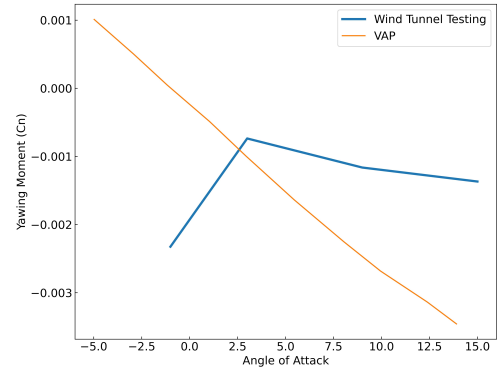
## Wind Tunnel Results

---

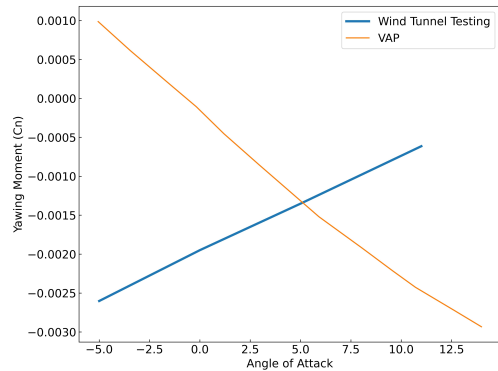
Figures A.2(a) to A.2(d) show the yawing moment coefficient for the no propeller configuration. The VAP 3.5 trend is opposite to what is expected from wind tunnel testing is likely due to the force and moment methods still being under development and testing [121].



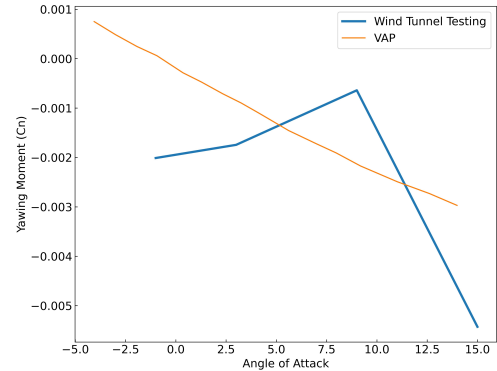
(a) Yawing Moment Coefficient at 10m/s airspeed for no propeller configuration



(b) Yawing Moment Coefficient at 10m/s airspeed for no propeller configuration



(c) Yawing Moment Coefficient at 20m/s airspeed for no propeller configuration

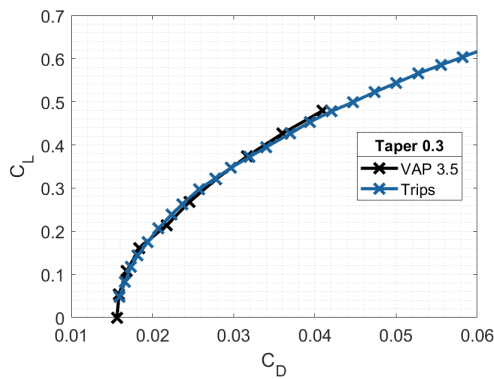


(d) Yawing Moment Coefficient at 20m/s airspeed for no propeller configuration

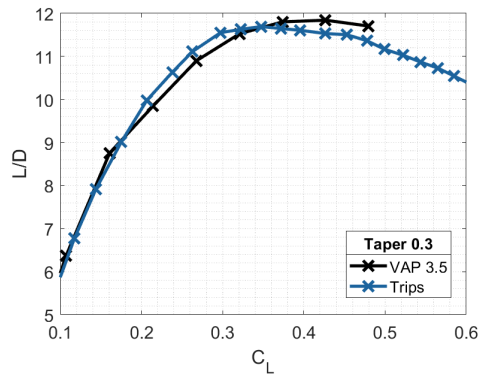
# Appendix B

## Wing Validation

Figure B.1(a) to B.2(b) show the wing validation for the 0.5 and 1 taper ratio results respectively.



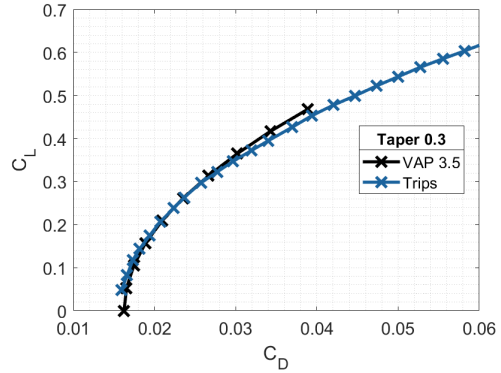
(a) Wing validation of  $C_L$  between VAP 3.5 and AVL with S5010 airfoil, root chord of 0.17m and taper ratio of 0.5 [120]



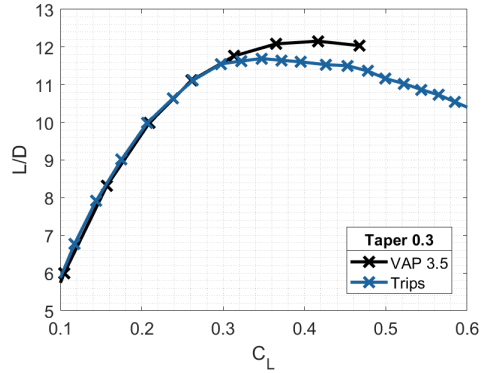
(b) Wing validation of the L/D ratio between VAP 3.5 and AVL with S5010 airfoil, root chord of 0.17m and taper ratio of 0.3 [120]

## Wing Validation

---



(a) Wing validation of  $C_L$  between VAP 3.5 and AVL with S5010 airfoil, root chord of 0.17m and taper ratio of 1 [120]



(b) Wing validation of  $L/D$  ratio between VAP 3.5 and AVL with S5010 airfoil, root chord of 0.17m and taper ratio of 1 [120]